# Contribution of Roughness to the Comprehension of Features on Ice Shelves and Implications for Ice Shelf Vulnerability

by

Ray Watkins

A dissertation submitted in partial fulfillment
of the requirements for the degree of
Doctor of Philosophy
(Materials Science and Engineering)
in The University of Michigan
2023

Doctoral Committee:

Professor Jeremy Bassis, Co-Chair
Professor Michael Thouless, Co-Chair
Professor Wei Lu
Professor Richard B. Rood

Ray Watkins
rayhw@umich.edu

ORCID iD: 0000-0003-1019-872X

To those who gave up even a small part of their day to talk through some science with me, Thank You

## ACKNOWLEDGEMENTS

First of all, I would like to thank my family who always supported me on my academic journey. To my parents Ray and Marilyn who inspired me to aim big and work hard to accomplish what I start out on. To my sister Grace who helped to keep the family working when I went to school. To my grandparents Joseph and Helen Lozinski, who helped to raise me and pushed me to be the best student I could be. And to my unbelievable and truly incredible girlfriend Caitlin, who always knows what buttons to push on me so that I can achieve my very best. And to Grandpee and Mom, wherever you may be, thank you for everything.

Thank you to my advisor Jeremy, who took me on as a student when no one else wanted to. You taught me an innumerable amount about science and about being a supporting and overall great person. I'm not sure you are told this enough, but you are an excellent advisor and mentor who truly cares about not just your students' work in Glaciology, but about the student themself. I cannot thank you enough for your support and guidance over these last 5 years.

I would like also to thank my committee members: Michael Thouless, Richard Rood, and Wei Lu. Specificity, to my co-advisor and co-chair Michael, thank you for taking the time to meet weekly with Jeremy and me and provide valuable material science/mechanical engineering commentary and advice to the questions that Jeremy and I were asking. I also would like to thank other current and former members of the vintage glaciology group: Yue Ma, Lizz Ultee, Morgan Whitcomb, Brandon Berg,

Sam Kachuck, Mac Cathles, Tristan Rendfrey, Maya Fields, and Tanner May. I truly enjoyed our talks on zoom and in the group office and appreciate your feedback along the way.

As I begin my career after grad school, I would also like to extend my thanks to the Michigan Tech Research Institute (MTRI). Specifically to Mike Sayers and Robert Shuchman, thank you for taking me in and letting me run with many of the projects that I was allowed to work on. Also, thank you for letting me tag along on some of the Sleeping Bear data collects. You guys treated me very well and I think we even had some fun along the way. I look forward to our continued work going forward.

Lastly, to all of my many friends from across the country, I am deeply grateful for the support you provide me and the many fun times that we have and will continue to have.

# TABLE OF CONTENTS

# LIST OF FIGURES

**Figure**

# LIST OF TABLES

**Table**

# LIST OF APPENDICES

**Appendix**

# ABSTRACT

Understanding the fate and stability of the Antarctic Ice Sheet is paramount for future projections of sea level rise in the coming centuries. Ice shelves—permanent, floating, sections of ice that fringe the coastline of Antarctica,—regulate the discharge of land-based ice into the ocean and are thought to buttress and stabilize the discharge of grounded ice upstream. Previous research has tied ice shelf collapse to the accelerated discharge of grounded ice into the ocean. However, our understanding of the processes that contribute to ice shelf weakening and demise remains underdeveloped. In this work, we aimed to improve our understanding of the processes that increase ice shelf vulnerability by developing a quantitative tool for measuring how fragmented an ice shelf is based on quantities that are increasingly available through remote sensing, such as ice thickness. We first explain how we can quantify the roughness of ice shelves and then calculate roughness of a series of ice shelves. We observe that consistent with previous studies, the roughness of ice shelves is largely determined by features associated with melting and fracturing of the ice. Basal melt carves out melt channels into the base of the ice shelf while fracture impart cracks (or crevasses) onto the ice shelf. We find that the topography of ice shelves is fractal, with the amplitude of roughness controlled by the melt rate. Next, we examine the discrete processes that are imparting roughness onto ice shelves and find that roughness is largest when basal melting and strain rate are largest. When both processes are active at the same time, the ice shelf becomes the roughest (or

most fragmented). Finally, by using data obtained over the last two decades across a menagerie of ice shelves throughout Antarctica, we track how the roughness of ice shelves has changed over twenty years. Critically, we find that ice shelves have seen a statistically significant increase in roughness have also had a significant reduction in their overall size. This is particularly true for ice shelves in the vulnerable and changing Amundsen Sea. This hints that ice shelf roughness, which can be easily measured from remotely sensed data products, may be a powerful tool in tracking the demise of some ice shelves over time. Being able to predict exactly when a particular ice shelf may collapse is going to collapse may be impossible. However, we show that by using roughness in addition to other metrics, we may be able to identify which ice shelves are the most at risk and therefore gauge future scientific efforts toward studying those ice shelves.

# CHAPTER I

# Introduction

## 1.1 Motivation: The Antarctic Ice Sheet and Sea Level Rise

The Antarctic continent, a land mass that is roughly the size of the United States and Mexico combined (Earth Resources Observation and Science (EROS) Center, 2018), is home to the Antarctic Ice Sheet (AIS). The AIS contains roughly 27 million cubic kilometers of ice, an amount that is equivalent to 58 m of eustatic sea level rise (Fretwell and others, 2013). Although it is extremely unlikely that all of the ice in this region would disappear on a century timescale, it is extremely likely that enough could be lost to affect a large portion of the world population. According to the 2019 IPCC Special Report on The Ocean and Cryosphere in a Changing Climate, approximately 680 million people live in a low-lying coastal zone, a number that could reach 1 billion by 2050 (Pörtner and others, 2019). Sea level is expected to rise in the coming century, affecting many of the people residing in these regions. Predicting some of the mechanics influencing the rate of this rise is crucial in knowing how fast people will be affected and to what extent.

Conservative estimates from the IPCC Special Report say that with zero carbon dioxide emissions past 2100, global temperatures would still increase by 1 degree Celsius (Pörtner and others, 2019). These rising temperatures across the globe could

work to destabilize parts of the AIS. It is important to note that the AIS, and ice sheets in general, regularly discharge ice. However, when this equilibrium is perturbed by climate forcing (such as temperature rise), discharge increases. In addition, potential zones of weakness across the ice sheet can become exacerbated.

## 1.2 Importance of Ice Shelves

Ice shelves are freely floating portions of the Antarctic Ice Sheet (AIS) fed by grounded ice upstream. Ice shelves are sustained by ice moving from the grounded ice upstream and play an important role in the dynamics, mass balance, and stability of the ice sheet. Moreover, ice loss from the AIS occurs primarily through ice shelves, with iceberg calving and basal melt currently the largest contributors. Although the relative effect of each basal melting and calving varies significantly based upon location, the average contribution across the continent to ice loss for both iceberg calving and basal melt is 50 % (Rignot and others, 2013; Liu and others, 2015). In addition to the role that ice shelves have in mass discharge, they also contribute significantly to the stability of ice sheets.

Because they are floating, ice shelves do not contribute inherently to sea level rise. Yet, the role that ice shelves play in buttressing the flow of inland ice to the ocean is crucial (Dupont and Alley, 2005). In the recent past (less than 30 years ago), major ice shelves have collapsed. For example, the Larsen A (Rott and others, 1996) and Larsen B (Rignot, 2004) ice shelves collapsed in 1995 and 2002 respectively. Both of these events coincided with increased ice mass flux into the ocean (Rignot and others, 2019a). This result serves as a link to show that the demise of ice shelves coincides directly with increased mass flux and therefore increased sea level rise, suggesting again the importance of ice shelves to stability. Additionally, DeConto and Pollard

(2016) calculated that the collapse of ice shelves in the West Antarctic Ice Sheet (WAIS) from a warming ocean could have a runaway effect on the grounding line retreat of many glaciers in this region. Specifically, a major vulnerability of WAIS (and therefore the ice shelves associated with it) is by way of the Marine Ice Sheet Instability (MISI). In this, a marine ice sheet - an ice sheet in which a significant portion (including its base contact) exists below sea level - becomes unstable due to the erosion of mass due to warming ocean temperatures (DeConto and Pollard, 2016). This is due partly to the retrograde slope of the glacial bed upstream in this region (Fretwell and others, 2013) which increases the flux of ice across the grounding line due to the increase of ice thickness (Schoof, 2007). This in turn creates a feedback loop that could result in rapid retreat of the grounding line - the region where the ice begins to float and influence sea level rise. Because ice shelves are vulnerable to a warming ocean (Shepherd and others, 2004), their potential loss could result in an even faster retreat of ice in WAIS.

A major region in the WAIS that has been subject to recent change and which may be susceptible to MISI is the Amundsen Sea Embayment: more specifically, Pine Island and Thwaites glaciers. Both glaciers sit on a retrograde bed and have been subject to unstable grounding line retreat over at least the last 30 years (Rignot and others, 2014) with predictions indicating that there may be no stop in sight. This is also coupled with recent observations that indicate an acceleration of both rifting - the formation of cracks in the ice shelf that pierce the entirety of the ice thickness - and large calving events (Jeong and others, 2016a). Currently, the thinning ice shelves of both glaciers are preventing full-on retreat. But based on these observations and events that have happened in the past, these ice shelves may also be on the brink of collapse. In short, based on observations, ice shelves that have buttressed

and slowed the flow of glacial ice are becoming increasingly fragile. This said it is poorly understood as to how climate forcing will affect the stability of the ice shelves going forward.

### 1.3 Ice as a Flowing Material

Glacial ice, like many other inorganic materials existing in nature, has a polycrystalline structure (Cuffey, 2010). This structure allows ice to "flow" somewhat like a very viscous fluid over large time scales, mainly through deformation brought on by creep in the material. The general relationship describing the rate of deformation (strain rate) of the ice to the stress causing the deformation is governed by Glen's Flow Law (Cuffey, 2010). This law was derived experimentally as shown in Equation 1.1 below:

$$\dot{\epsilon} = A\sigma^n \tag{1.1}$$

In this expression, $\dot{\epsilon}$ is the strain rate, $\sigma$ is the stress, $n$ is a parameter experimentally determined that has a value equal to approximately 3 (Cuffey, 2010; Glen, 1953), and A is a constant that varies based upon ice temperature, orientations of crystals, ice debris, and other factors. This results in strain rate that is fairly sensitive to the driving gravitational stresses. If stresses in the ice go above certain, undefined thresholds that the strain rate can keep up with, then the ice will deform plastically. This results in the opening of crevasses - cracks within the ice. Thus, the movement and deformation of the ice change its shape and produces geometries that may control future actions that the ice takes.

## 1.4 Features on ice shelves and their control on stability

Expanding upon one of the drivers of ice mechanics, which were previously noted as iceberg calving and basal melt, we now look at the features that are synonymous with each. We note first that the calving cycle is predominantly thought to be controlled by rifts. Rifts start as brittle fractures around regions where stresses are large. This happens by pinning points - underwater islands where the ice shelf is locally grounded - and shear margins - where fast-flowing ice meets a slow or still region of ice or rock. These fractures then propagate through the ice shelf (Joughin (2005)). Prior to iceberg calving events, the basal surface of the ice fractures resulted in features that have a wide spectrum of size and properties. From recent observations of the Larsen C ice shelf, narrow brittle fractures, ice thickness sized crevasses, and kilometer-scale rifts have been identified (McGrath and others, 2012). In McGrath and others (2012), it is proposed that the crevasses form in regions where there is high stress (e.g. regions where the flows from different ice streams combine). To garner a relative size, we note that in McGrath and others (2012), the crevasses first penetrate relatively deep into the ice ($\approx$125 m) and have a small opening width ($\approx$45 m). Then, as they advect downstream their penetration depth decreases ($\approx$80 m) and their opening width increases ($\approx$195 m).

In contrast to rifts, basal melt tends to be related mostly to the intrusion and circulation of "warm" waters which enter the ocean lying underneath the ice shelf (Fricker, 2005). From basal melt observations, results indicate that even across singular ice shelves heterogeneous patterns of melt can result in morphologies that are complex (Dutrieux and others, 2014). Similar to rifting, Liu and others (2015) also speculated that basal melt channels could enhance iceberg calving, though the

specific mechanics surrounding this process are not yet fully understood.

## 1.5 Discrepancies between Models and Data

With these mechanisms in play, the ice deforms and takes on an ever-changing shape. Using observations taken from NASA's Operation IceBridge (Paden and others, 2010), this complex and bumpy shape can be seen in an along flow track of the Pine Island Ice Shelf. This stands in stark contrast to how large-scale ice sheet models, such as BISICLES (Berkeley Ice Sheet Initiative for CLimate ExtremeS), initialize their models in which the ice/ocean interface is relatively smooth (Cornford and others, 2015). As such, this results in a large discrepancy between what is used in models and what the data shows. This is illustrated by the transect shown in Figure 1.1. Understanding first what causes these "bumps" to form in the data and second, if these bumps are paramount to ice shelf stability is one of the major themes of this work.

## 1.6 Visual differences in ice shelves

Using satellite imagery, we can optically compare various ice shelves to each other to visually inspect if they are bumpy or smooth. Take for example the four ice shelves shown in Figure 1.2. We can see visually that the Pine Island and Thwaites ice shelves (Figure 1.2a and b) appear to look entirely different than the Ross and Larsen C ice shelves (Figure 1.2c and d). For Pine Island and Thwaites, the ice as a whole in both cases looks much more fractured and broken than from Ross and Larsen C. This is due directly to the prevalence of more "rough" features on the two bumpier ice shelves. But to address what these rough features are in detail and quantitatively describe how much rougher the two former ice shelves are than the two latter, we need to define what we mean by roughness.

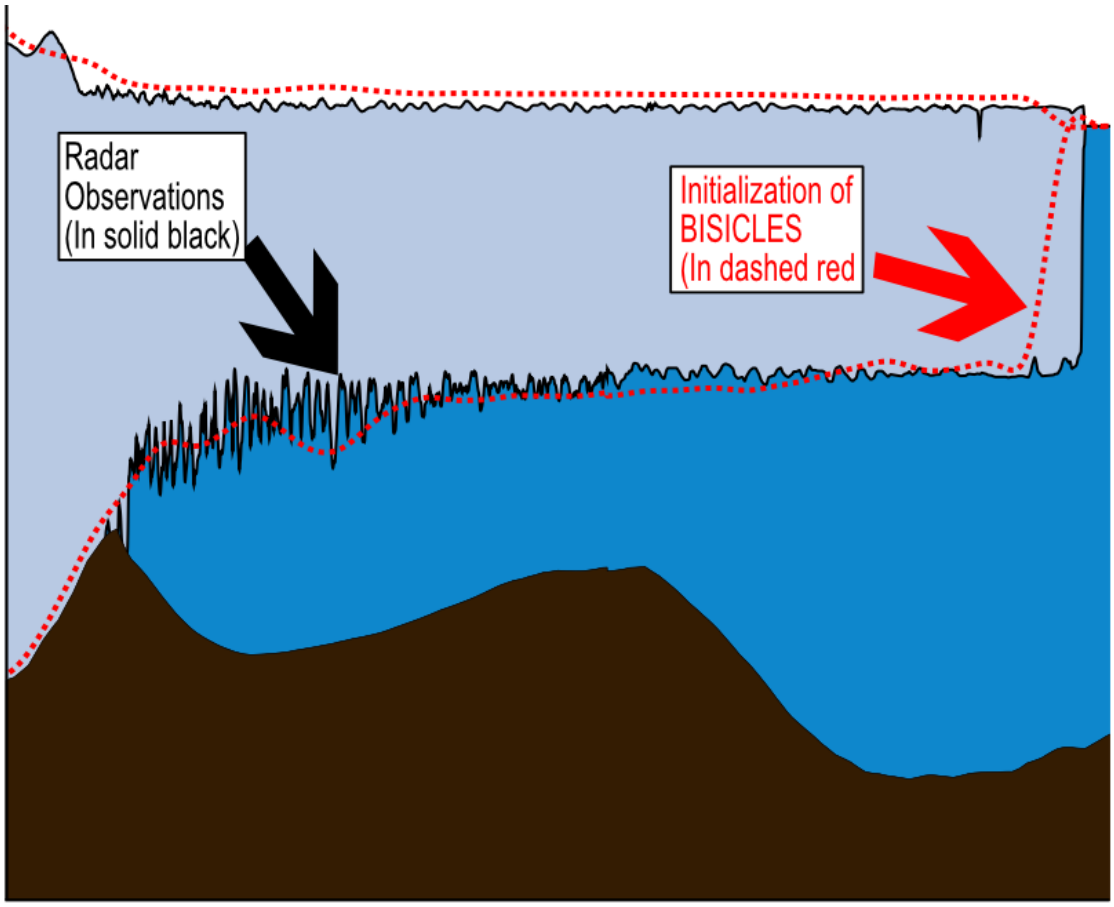


Figure 1.1: A comparison between the observed data of the Pine Island Ice Shelf (shown as the black solid line) and the initialization the BISICLES simulation of Pine Island along the same flight line (shown as the red dashed line). The surface of the ice is found through an altimeter measurement. The bottom of the ice is calculated using the radar-observed ice thickness.

## 1.7 General Definition of Roughness

To take a more quantitative approach, we must first define what it means to be bumpy or smooth. Within glaciology, the use of roughness has typically been reserved for use in conjunction with describing glacial beds. In this, roughness is calculated as being the integral of the power spectral density (which is obtained by dividing the square of the Fourier transform by the length of a given profile) at multiple windowed distances (Taylor and others, 2004; Li and others, 2010a; Rippin and others, 2014). More specifically, Li and others (2010a) estimates the along-track roughness of cross-

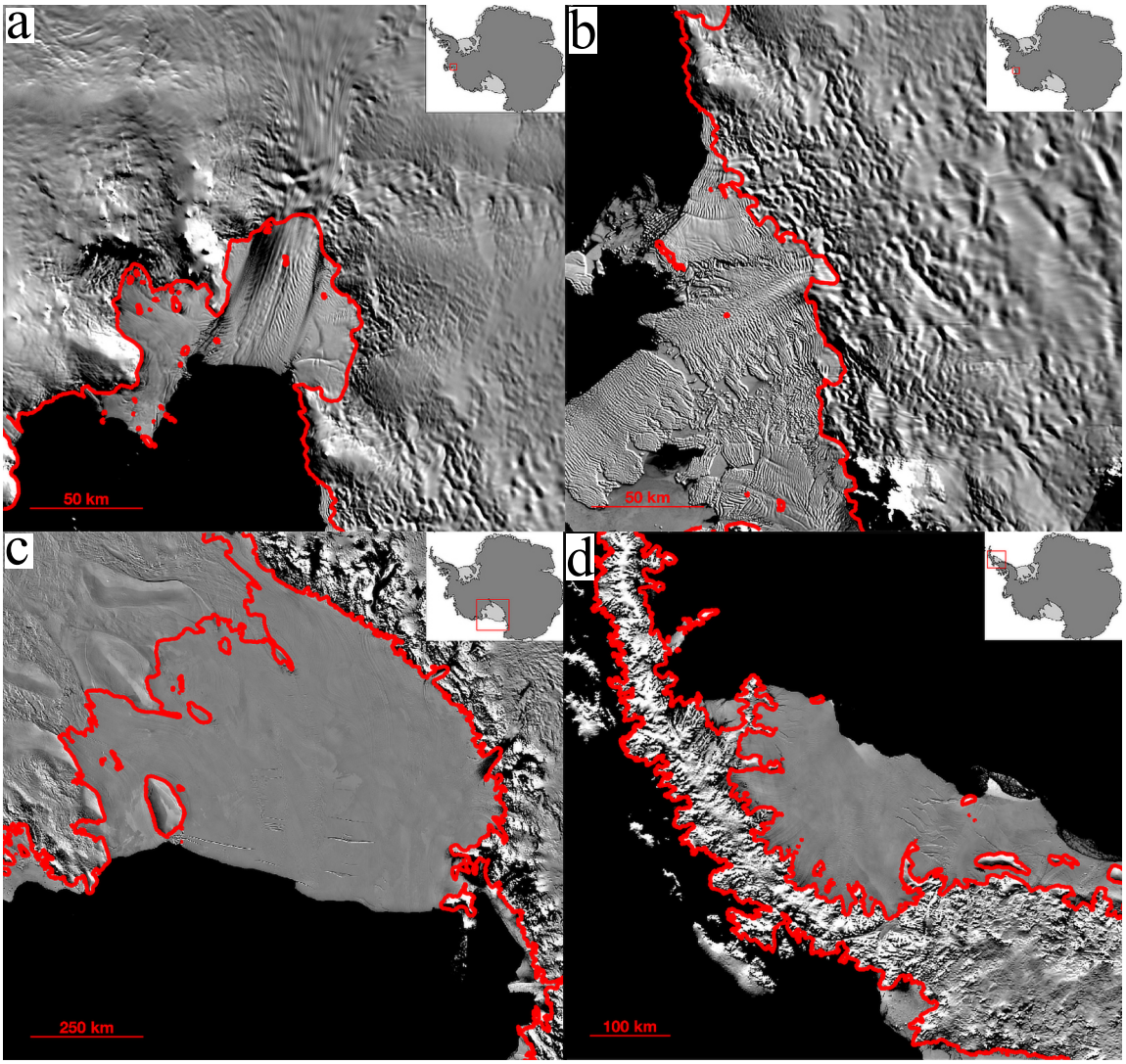


Figure 1.2: MODIS Satellite imagery for a) Pine Island Ice Shelf, b)Thwaites Ice Shelf, C)Ross Ice Shelf, and D)Larsen C Ice Shelf. The red line shows the grounding line (where the ice begins to float). Note how much rougher the first two ice shelves are relative to the last two.

sectional profiles by using a moving window and computing multiple power spectra via discrete, overlapping blocks of data. From a mathematical standpoint, take for example the two equations below:

$$Z_0(x) = Z(x) - \left\langle Z(x) \right\rangle \tag{1.2}$$

$$S(k) = \frac{1}{l} \mid \overline{Z_0}(k) \mid^2 \tag{1.3}$$

In Equation 1.2, Z(x) represents the bed profile and $Z_0$(x) represents the bed profile with the mean of the data,$\left\langle \text{Z(x)} \right\rangle$, subtracted out. Then in Equation 1.3, $S(k)$ represents the power spectral density (as a function of frequency $k$ ), which is calculated by dividing the square of the Fourier Transform of $Z_0$(x) (indicated by $\mid \overline{Z_0}(k) \mid^2$) by the length of the profile $l$. To evaluate the roughness, the integral is taken of $S(k)$ between two frequencies, $k_1$ and $k_2$. The roughness is indicated by $\xi$ and is shown in Equation 3:

$$\xi = \int_{k_1}^{k_2} S(k)dk \tag{1.4}$$

The drawback to the above definition of roughness is that it does not inherently have any spatial 'resolution' (as is the definition of the Fourier Transform). In Li and others (2010a), they approximate roughness locally along the track by using a moving window and estimating it at discrete distances. As we are particularly concerned with the spatial variability of roughness, we seek to use a different frequency transform that does have some spatial resolution. We also want to eliminate as much bleeding (spectral leakage) as possible, which is a side effect of windowing the Fourier transform. Therefore, our approach to calculating roughness will be similar to those used in the past, however, the tool we choose to use to calculate it will be different.

## 1.8 The Continuous Wavelet Transform

The alternative approach to calculating the frequency spectrum of the ice surface that we choose to use that does have some spatial resolution is the continuous wavelet transform (CWT). The CWT is described in detail in a series of papers: Lilly and

Olhede (2009); Lilly and Olhede (2012); Lilly (2017). The advantage of the continuous wavelet transform is that wavelets provide improved along-track resolution by providing optimal basis functions that avoid spectral leakage when windowing the along-track data. To understand the theory behind the CWT, let us start by describing it in a mathematical sense. As defined in Lilly and Olhede (2009), the formal definition of the continuous wavelet transform is:

$$W(x,s) = \frac{1}{2\pi}\int_{-\infty}^{\infty} \Psi^*(s\omega)X(\omega)e^{i\omega x d\omega} \tag{1.5}$$

In Equation 5, $\Psi^*$ is the complex conjugate of the mother wavelet - which is the optimal basis function expressed in frequency space - and $X(\omega)$ is the Fourier Transform of the original signal (also now existing in frequency space). For the purposes of our calculations, we use the Morse Wavelet. This is a standard wavelet that is well documented and is described by Equation 6:

$$\Psi_{\beta,\gamma}(\omega) = U(\omega)\alpha_{\beta,\gamma}\omega^{\beta}e^{-\omega^{\gamma}} \tag{1.6}$$

In this expression, $U(\omega)$ is the Heaviside step function in frequency space with $\alpha$, $\beta$, and $\gamma$ all becoming scaling parameters having the relationship given by:

$$\alpha_{\beta,\gamma} = 2(e\gamma/\beta)^{\beta/\gamma} \tag{1.7}$$

The CWT that is obtained from Equation 5 is then a function of magnitude, distance, and frequency. From this, we then take roughness to be the integral of the wavelet transform with respect to the frequency at every distance. This in turn yields roughness as a function of distance

## 1.9 Calculation of Roughness

To calculate the roughness of ice shelves, we aim to bring together both the standard definition of roughness in glaciology along with the use of the CWT. As such, we will take roughness as being the integral of the CWT with respect to frequency at every distance step. From a mathematical standpoint, this can be represented by Equation 8:

$$\xi\ (x) = \int_{s_1}^{s_2} W(x, s) ds \tag{1.8}$$

Keeping in mind that the CWT is most accurate at the center of the transform (due to edge bleeding), we also aim to window the data prior to performing the operation. Because of this, we take the roughness at the center of each window and repeat the process until the roughness of the entire profile is resolved. Also removed is any linear trend in the data set. This is done so as to calculate the local roughness of the flight track without interference from the overall thinning of the ice. By windowing, we introduce two other variables, window length, and percent overlap.

To better understand how the process works, let us take for example a visual representation of the calculation. We take three variations of a sinusoidal function and perform the operation. The three test cases taken are:

$$F(x) = sin(x) \tag{1.9}$$

$$F(x) = sin(x) + x \tag{1.10}$$

(1.11) $$F(x) = sin(x) + sin(2x)$$

=

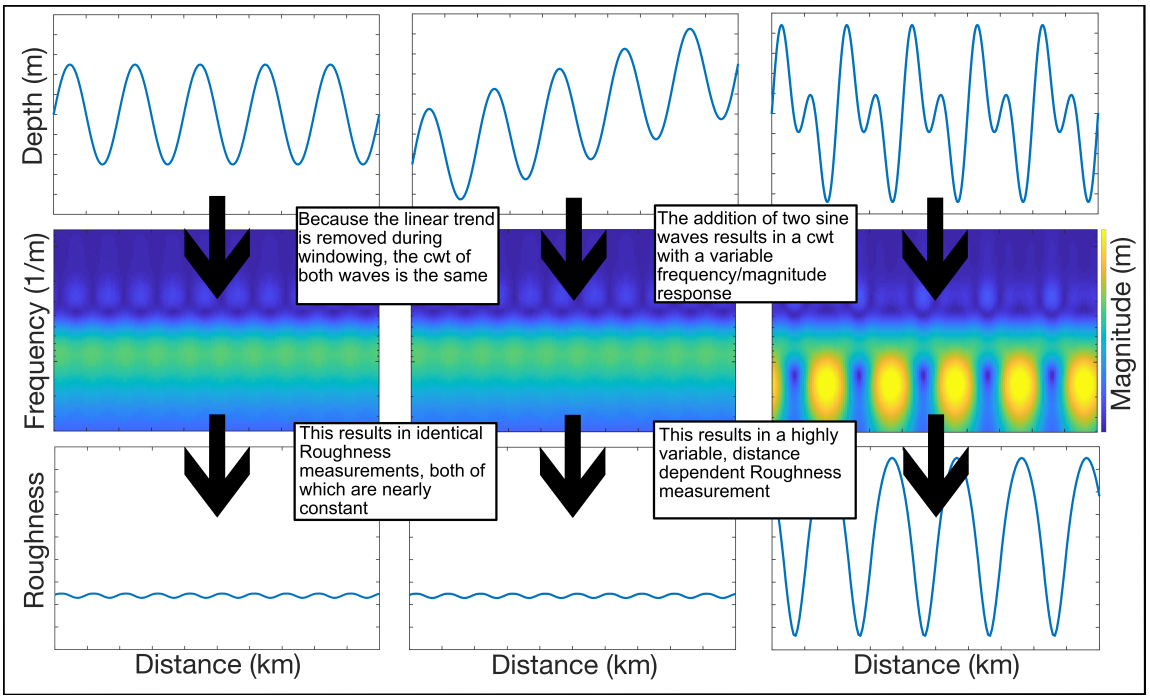


Figure 1.3: A depiction of the continuous wavelet transform and roughness calculation for multiple functions of sine. Moving from left to right at the top of the figure are Equations 1.9,1.10, and 1.11 respectively. Notice how the transform and roughness are unaffected by a linear trend in the data (due to detrending) but are highly affected when two sine waves both interfere constructively (resulting in an increase in roughness) and de-constructively (resulting in a decrease in roughness)

We choose these particular test cases due to the fact that they are fairly representative of the actual data. Equation 1.8 shows a profile oscillating at one particular frequency and amplitude, Equation 1.9 shows the same profile as Equation 1.8 but with an upward linear trend, and Equation 1.10 shows a spatially varying frequency function. Calculating the roughness of the three functions creates the result shown in Figure 1.3.

As can be seen, the roughness of Equation 1.9 is relatively low and also mostly constant. The slight variation in the roughness comes from the windowing aspect of the process, but the effect is minimal. Because of the linear de-trending, the

frequency response and the roughness of Equation 10 is identical to that of Equation 1.9. The roughness of Equation 1.11 becomes the most interesting in that it fluctuates between a high and low value based on the location of the profile. This is also reflected in the frequency spectrum of the equation in which there are regions of high-magnitude response.

## 1.10 Applying the hydro-static equilibrium assumption

The first step in calculating the roughness of ice shelves as a whole is to compute the roughness along a singular flight track. This is done in the same style as the methods section above. The data used throughout this work measures the ice surface, the ice base, and the ice thickness. For ice shelves that are freely floating, we can go back and forth between all three metrics, assuming we know the density of the ice as well as the seawater of which it is floating. Take for example the following equations:

$$Ice_{Bottom} = \frac{\rho_{Ice}}{\rho_{Water}} * Ice_{Thickness} \tag{1.12}$$

$$Ice_{Thickness} = Ice_{Surface} - Ice_{Bottom} \tag{1.13}$$

For the purpose of our calculations, the density of the ice $\rho_{Ice}$ and the density of seawater $\rho_{Water}$ are taken to be 920 $kg * m^{-3}$ and 1010 $kg * m^{-3}$ respectively. These numbers are fairly variable in nature based on numerous physical drivers. As such, these values were chosen so as to create a surface that lined up most accurately with physical results. Thus, given either the ice surface, ice thickness, or ice base, we can obtain the other measurements.

## 1.11 Using the CWT to calculate ice shelf roughness

Next, we must set the various parameters that will be used in conjunction with the CWT. We choose to window the data into 3 km wide segments. This number

was chosen somewhat arbitrarily, with window sizes within an order of magnitude having a minimal effect of the results. However, because most sub-ice shelf features fall within this order of magnitude range, we felt the selection of 3 km was an appropriate choice. With this, we also choose to use a window overlap of 99%. This provides us with a well-defined resolution and also ensures the computational efficiency of the calculation. In terms of the scaling parameters, we chose to use values that would produce the highest frequency resolution for the range of the apparent features. Finally, for the frequency bounds that were used in the integral that defines roughness, we choose to use bounds that go from 0 to 10 $km^{-1}$. These were chosen to encompass all features that can be resolved by the spatial resolution of the data. In addition, these bounds are also changed on a case-by-case scenario, corresponding to the resolution of the data source for which the roughness is calculated. In a concise form, all of the parameters that were used in the CWT are outlined in Table 1.1 along with their corresponding symbols and values.

Table 1.1: A listing of parameters used in the CWT

| Parameters | | |
|---|---|---|
| Parameter Name | Parameter Symbol | Parameter Value |
| Window Length (km) | $l$ | 3.00 |
| Window Overlap (%) | $w$ | 99.0 |
| Scaling Parameter 1 | $\beta$ | 3.00 |
| Scaling Parameter 2 | $\gamma$ | 1.01 |
| Low Frequency Bound (1/km) | $s_1$ | 0.00 |
| High Frequency Bound (1/km) | $s_2$ | 10.0 |

## 1.12 A note on Appendices D and F

At the end of this document are Appendices D and F which are two published manuscripts that deal mostly with the remote sensing of water quality on the Great Lakes in North America. This work was done as an aside to the main chapters in this dissertation as a way of furthering this author's scientific exploitation knowledge as

a whole. Particularly, these manuscripts involved in situ sampling campaigns which is a topic that is not covered by the content in the main chapters of this work. In addition, the work highlighted in these appendices performs two noteworthy scientific tasks. First, it serves to show that Light Detection and Ranging (LiDAR) based satellites can be used to monitor the Great Lakes (and other regions of similar size) from space. Second, the results show an excellent correlation between remote sensed results and in situ measurements, showing that results obtained from satellites are in fact reliable.

# CHAPTER II

# Roughness of Ice Shelves Is Correlated With Basal Melt Rates

This chapter appears in its entirety in the following:

Watkins RH, Bassis JN and Thouless MD (2021) Roughness of ice shelves is correlated with basal melt rates. *Geophysical Research Letters*, **48**(21) (doi: 10.1029/2021gl094743)

## 2.1 Introduction

Ice shelves—slabs of floating ice fed by flow from the grounded ice upstream—play a critical role in limiting the discharge of grounded ice from the Antarctic ice sheet into the ocean (Dupont and Alley, 2005; Pritchard and others, 2012; Gudmundsson, 2013; Shepherd and others, 2018). Because ice shelves are in contact with both the ocean and atmosphere, they are sensitive to atmospheric and oceanic warming. For example, the explosive melt-water related disintegration of the Larsen A and B ice shelves in 1995 and 2002, provide vivid illustrations of the speed with which ice shelves can disintegrate (Rott and others, 1996; Scambos and others, 2003; Robel and Banwell, 2019). Both of these events increased the amount of ice discharge into the ocean (Scambos, 2004; Rignot, 2004; Rignot and others, 2019b), linking the

demise of ice shelves directly with increased mass flux, and increased rise in global sea levels.

Although rising atmospheric temperatures are responsible for the meltwater driven collapse of sections of the Larsen ice shelf, the temperatures in many other parts of Antarctica, like the Amundsen Sea Embayment, remain cold and there is little sustained surface melting (Dixon, 2007; Trusel and others, 2013; Werner and others, 2018). Instead, thinning, grounding-line retreat, and the instability of these glaciers is connected with basal melt associated with the intrusion of warm ocean waters (Jenkins and others, 2018; Nakayama and others, 2019). Recent observations and simulations show that, in addition to eroding contact with the margins and pinning points, basal melt can sculpt complex and heterogeneous basal channels (Stanton and others, 2013; Dutrieux and others, 2013, 2014; Drews, 2015; Gourmelen and others, 2017). Similarly, deep basal crevasses that eventually penetrate the entire ice thickness and become rifts have also been observed across many ice shelves (McGrath and others, 2012; Jeong and others, 2016a).

Rifts, crevasses and melt channels contribute to the overall topography and roughness, defined here as topographic variations in the ice thickness varying from crevasses to large melt channels and rifts, of ice shelves. However, the connection—if any—between the processes responsible for these features remains poorly understood. One possibility is that increased basal melt results in decreased ice thickness, reducing the restraining lateral shear stresses and, potentially, allowing the ice shelf to become un-moored from pinning points (Still and others, 2018). This reduction in restraining forces could thus result in increased fracturing, and decreased mechanical stability (Favier and others, 2016). Thus, one hypothesis is that increased ocean forcing results in thinning, reducing buttressing and increasing crevassing and rift-

ing. Similarly, formation of melt channels can alter the stress distribution within the ice, promoting basal and surface fractures and/or excavating existing basal crevasses (Vaughan and others, 2012; Bassis and Ma, 2015a; Alley and others, 2016). This suggests the complementary hypothesis that ocean forcing may also directly increase fracture and failure of ice shelves through the formation of melt channels and/or excavation of basal crevasses, which have advected and deformed for decades, centuries (or longer) and which potentially take on a wide variety of shapes and sizes. Here, we use existing ground-penetrating radar measurements to characterize roughness of ice shelves and the relationship between roughness and basal melt for a suite of Antarctic ice shelves.

## 2.2 Methods

### 2.2.1 Data and Study Regions

We used ground-penetrating radar data from a variety of sources (Table 2.1) to determine the thickness of ice shelves. Most available data that covers the Pine Island, Ross, Thwaites, Dotson, Getz, Larsen C, and Filchner ice shelves were used. These ice shelves were chosen because multiple tracks covered the region, and because these regions provide contrasting environmental and glaciological conditions. For instance, the Pine Island and Thwaites ice shelves are subject to significant basal melting (Dutrieux and others, 2014; Webber and others, 2017; Shean and others, 2019), whereas the Ross and Filchner ice shelves are subject to colder ocean conditions and much lower melt rates (Dixon, 2007; Liu and others, 2015).

We performed a more detailed study of Pine Island and Ross because of the abundant data coverage for these two ice shelves, and because of the contrasting climatological forcing. For instance, Pine Island is subject to large basal melt rates along the grounding line that can exceed hundreds of meters per year (Dutrieux

and others, 2013; Shean and others, 2019), resulting in an elevated average basal melt across the entire ice shelf (Liu and others, 2015). The increased melt rate has triggered grounding line retreat (Favier and others, 2014) and, potentially, increased iceberg calving (Liu and others, 2015; Arndt and others, 2018; Joughin and others, 2021). By contrast, the Ross ice shelf experiences much lower basal melt rates (Das and others, 2020), with stable grounding line positions.

| Data Name | Data Source | Reference |
|---|---|---|
| MCoRDS L2 Ice Thickness | Operation IceBridge | (Paden and others, 2010) |
| Pine Island Ice Shelf 2011 | Geophysics Data Portal | (Vaughan and others, 2012) |
| Total Ice Thickness | ROSSETTA-Ice | (Das and others, 2020) |
| Average Basal Melt | Multiple Sources | (Liu and others, 2015) |

Table 2.1: List of data products used in this study

#### 2.2.2 Quantifying roughness

We followed Whitehouse (2004), and defined roughness (in meters) as the square root of the integral of the power spectral density $S(k)$:

$$R = \sqrt{\int_{k_1}^{k_2} S(k)dk}, \tag{2.1}$$

where $k$ (1/m) represents the wavenumber, and $k_1$ (1/m), $k_2$ (1/m) represent the range of integration in wavenumber space. The range is related to the resolution of the data and length of tracks analyzed.

To calculate spatial variations in roughness across individual ice shelves, we first computed power spectra at windowed distances of size $w$, set to 3000 m, and overlap percentage $m$, set to 99 %. Roughness was then obtained through numerical integration of Equation 2.1 along each of the windows. Traditionally, the Fourier transform is used to estimate the power spectral density. However, we instead used

a continuous wavelet transform, which produces improved along-track resolution by providing optimal basis functions that avoid spectral leakage when windowing the data (Sifuzzaman, 2009). This allowed us to resolve spatial variations in roughness at higher resolution.

We also computed the average roughness for each ice shelf by first computing the average power spectral density (obtained by averaging the spectra of all tracks), and then numerically integrating to find the average roughness. This approach has the advantage that it also provided an average spectrum for each ice shelf. We chose integration bounds between 0.0001 (1/m) for $k_1$ and 0.01111 (1/m) for $k_2$. This corresponds to looking at wavelengths between $\sim$ 90 m and $\sim$ 10 km, and was done so that we could consistently compare roughness between ice shelves of different dimensions. Our results are not sensitive to any windowing or scaling parameters when the parameters are varied over an order of magnitude. However, taking a track length much larger than 10 km, excluded a large number of tracks from the analysis. Moreover, we experimented with computing roughness and average roughness using a range of definitions, including just taking the mean of the windowed roughness measurements. Different definitions can influence the magnitude of roughness, but the trends and relative values are insensitive to any change in the definition of roughness used.

#### 2.2.3 Spectral characteristics of roughness

If the power spectral density has peaks associated with features that have specific wavelengths, we can identify the dominant wavelength (or wavenumber) from the power spectra. Alternatively, the topography of many surfaces on Earth, Mars and Venus follow a power-law over a range of wavelengths (Lovejoy, 1982; Mandelbrot and Wheeler, 1983). If the topography follows a power-law distribution, the power

spectral density, takes the form:

$$PSD(k) = S(k) = Ck^{-\alpha}, \tag{2.2}$$

where $C$ is a roughness scaling parameter, $\alpha$ is the power-law (or fractal) exponent , and $k$ (1/m) is the wavenumber. The exponent $\alpha$ is commonly represented as the fractal dimension $F_D$ (Joe and others, 2017), with the relationship between $\alpha$ and $F_D$ expressed by $F_D = \frac{-\alpha+8}{2}$.

We followed Clauset and others (2009) to estimate if the power spectral density could be described as a power-law. If it could, we then estimated the scaling exponent $\alpha$, including a minimum cutoff frequency into the fit of the exponent (Clauset and others, 2009) to account for limits in the resolution of our data. After estimating the exponent, we determined $C$ by preforming a least-squares regression to the power-law.

## 2.3 Results

### 2.3.1 Roughness of the Pine Island and Ross ice shelves

We first examined roughness of the Pine Island and Ross ice shelves. Roughness of Pine Island (Figure 2.1(a)) varies from close to $\sim$ 0 m in the central portions and near the calving front to around $\sim$ 60 m near the grounding line and pinning points. We see larger roughness in isolated regions of the ice shelf, corresponding to topographic features like pinning points (box A), melt channels (box B), crevasses in shear margins (box C), and rifts (box D). These structural features have all been previously documented in the ice shelf (Scambos and others, 2007; Vaughan and others, 2012; Lhermitte and others, 2020), however it is also possible the rift in box D may have initiated in the shear margin before becoming a rift, indicating that classifying features is ambiguous. Similarly, the pinning point in box B may

contain melt channels and crevasses. Moreover, Pine Island may have retreated off the pinning point (box A) between 2009 and 2011 (Favier and others, 2014), and the elevated roughness may be a legacy of previous episodic grounding on and/or processes associated with un-mooring from the pinning point. (Note the pinning point we document is further upstream than the pinning point noted by (Jenkins and others, 2010)).

By contrast, roughness of the Ross ice shelf (Figure2.1(b)) is much lower overall compared to Pine Island, with values rarely exceeding 10 m and it is less than 3 m on the majority of the ice shelf. Despite the smaller overall roughness of the Ross ice shelf, we still see elevated roughness relative to the mean for both ice shelves around pinning points, melt channels, shear margins and rifts (Figure 2.2). This is especially true for pinning points and shear margins. All of these structures create a topographic signature in roughness, but the magnitude varies substantially between ice shelves.

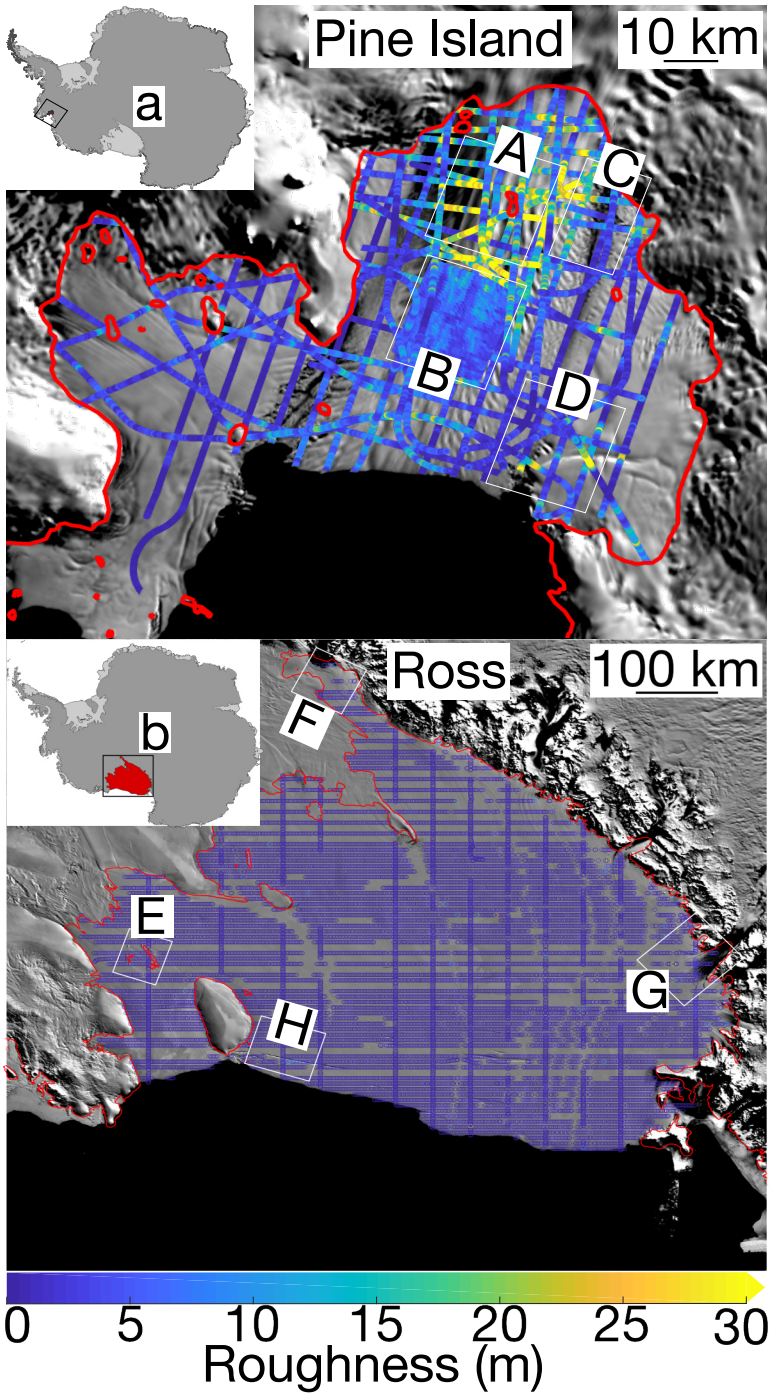


Figure 2.1: Spatial patterns of roughness for a) the Pine Island ice shelf and b)the Ross ice shelf. Roughness is color-coded and plotted over the MODIS Mosaic Image of Antarctica (Scambos and others, 2007). Shown in red is the grounding line for each ice shelf obtained from NASA's MEaSUREs data-set (Rignot and others, 2013). Also boxes A-H are subsets of each ice shelf, which are shown in greater detail in Figure 2.2

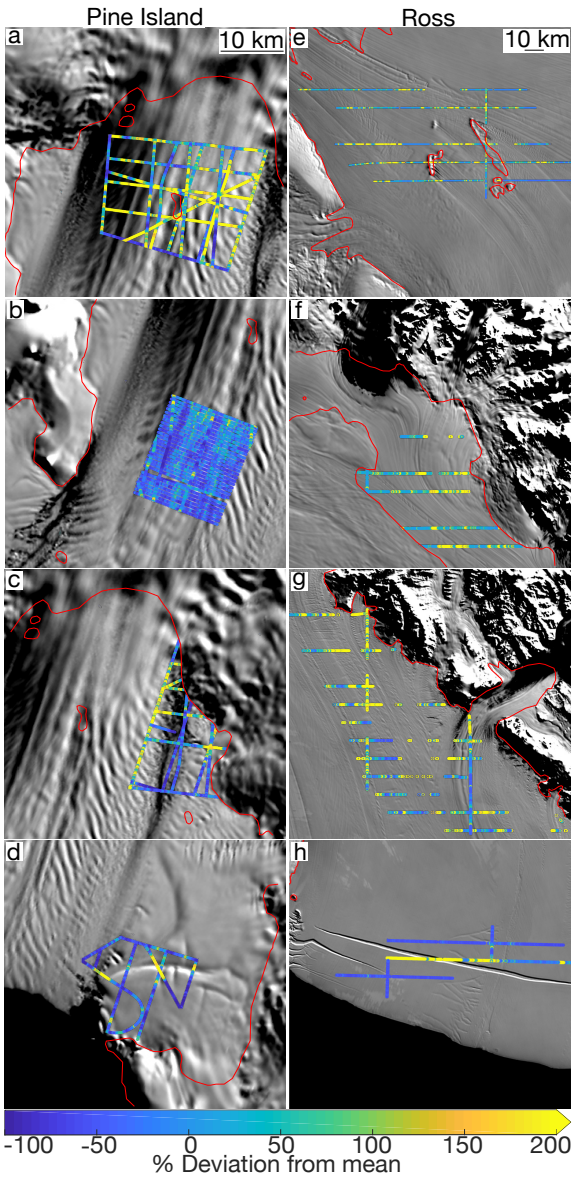


Figure 2.2: Percent deviation from the mean roughness for Pine Island (left) and Ross ice shelf (right). Panels a and e show pinning points. Panels b and f show melt channels. Panels c and g show shear margins. Panels d and h show rifts.

### 2.3.2 Average and spectral characteristics of roughness

We see clear differences in the magnitude of roughness between the Pine Island and Ross ice shelves. Because pinning points, melt channels, crevasses, and rifts elevate roughness, we anticipated that the topography associated with these features would have characteristic spectral signatures. To investigate the spectral characteristics

of roughness, we averaged the power spectral density for all the flight tracks over the Pine Island and Ross ice shelves (Figure 2.3). Contrary to our expectations, we do not see characteristic peaks in the power spectra corresponding to discrete wavelengths. Instead, the spectra for both Pine Island and Ross approximately followed power-laws. Moreover, the power-law exponent is statistically equivalent for both ice shelves, with the primary difference that the spectrum for Pine Island is shifted higher at *all* wavelengths compared to the Ross ice shelf.

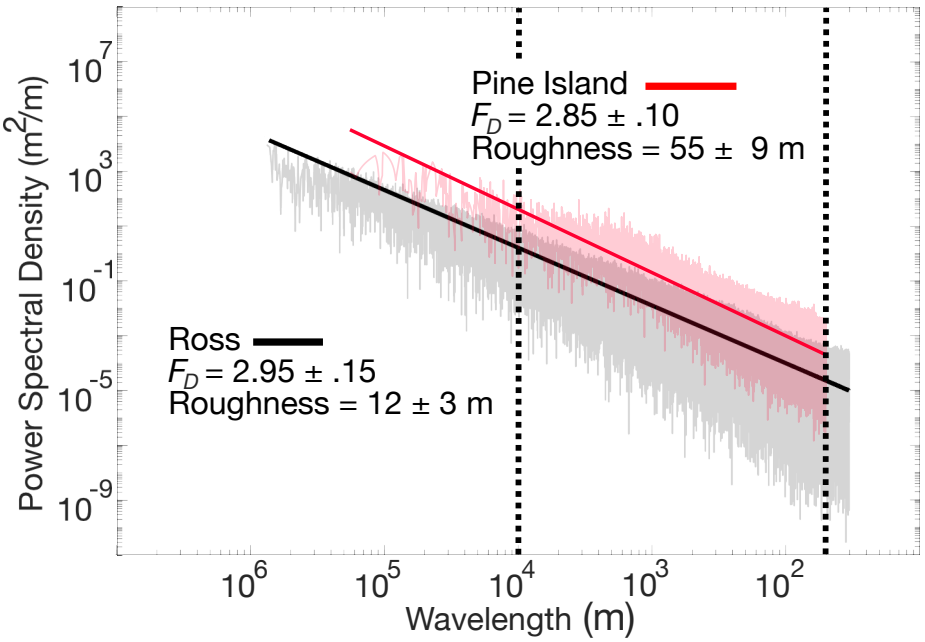


Figure 2.3: The power spectral density of all tracks going over the Pine Island and Ross ice shelves. Pine Island is plotted in light red and Ross is plotted in light grey. Also shown is a least squares fit of the power law equation to each spectrum. The solid red line represents the fit for Pine Island while the solid black line represents the fit for Ross. Integration bounds used for calculating the average roughness for each ice shelf are plotted by the black dotted lines.

We also characterized the average roughness for Pine Island and Ross by integrating over the average spectrum of each ice shelf between two wavenumber bounds (dashed lines in Figure 2.3). We found that the average roughness of Pine Island (55 m) was almost five times that of Ross (12 m). This result is consistent with our previous result in Figures 2.1 and 2.2, where we showed that roughness was consistently

larger on Pine Island then the Ross ice shelf.

The power-law behavior might be a consequence of the fact that tracks intersect with features at different angles, blurring out any characteristic peaks in the spectra. For Pine Island, where tracks are roughly oriented along-flow and transverse-to-flow, we also calculated the average transverse-to-flow roughness and the average longitudinal-to-flow roughness. The transverse-to-flow roughness was about twice as large as the longitudinal to flow roughness (66 m vs 30 m. In both cases however, the spectra of each approximately followed a power-law with a statistically identical scaling exponent. This indicates that although Pine Island is experiencing increased basal and excavation of melt channels, which are seen mostly in the transverse to flow tracks, the increased roughness is not solely due to the increased prevalence of melt channels. Instead, transverse-to-flow features, like crevasses, are also introducing a larger component of roughness.

### 2.3.3 Roughness is highly variable between ice shelves, but the power-law exponent is constant

To determine if these results hold for a larger suite of ice shelves, we next extended our roughness analysis to five other Antarctic ice shelves: Thwaites, Dotson, Getz, Larsen C, and Filchner. We again found that the power-law exponent was statistically identical for all of the ice shelves considered. However, the average roughness varied significantly (Figure 2.4). Measurements of the average roughness ranged over an order of magnitude, with a high of around 90 m for Thwaites and a low of around 12 m for Ross. However, we do see a pattern with larger roughness associated with ice shelves in the Amundsen Sea Embayment. We note that the Getz ice shelf may have slightly low roughness. However, given the small number of tracks, the low roughness of the Getz ice shelf is not statistically significant. Nonetheless, this

low roughness may be due to its slow flow (Selley and others, 2021) and complex bathymetry constrained by multiple pinning points (Cochran and others, 2020).

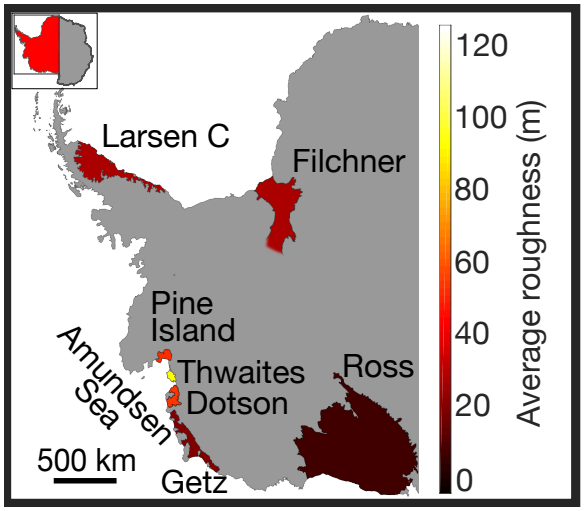


Figure 2.4: A mapping of roughness across several Antarctic ice shelves. Ice shelves are color coded to match up with the roughness axis

### 2.3.4 The average roughness of ice shelves is correlated with basal melt rates

Ice shelves in the Amundsen Sea Embayment have a larger roughness compared to other ice shelves (Figure 2.4). They also experience much larger basal melt rates due to the intrusion of warm water within the Amundsen Sea (Jenkins and others, 2018; Nakayama and others, 2019). To test for a connection with basal melt, we examined the relationship between the average basal melt rate, obtained from Liu and others (2015), and the average roughness of each ice shelf (Figure 2.5). We see a strong linear trend between increased basal melt and increased roughness. We also tested the effect of ice thickness on this trend and found that, even when the roughness is normalized with respect to the ice thickness, the strong linear trend remains. Crucially, this shows that basal melt correlates with—and perhaps triggers—increased roughness of the ice shelves. Intriguingly, based on its apparent power law nature, roughness also appears to increase across a broad spectrum of wavelengths, which may indicate a

complex interplay between increased basal melt and ice dynamics.

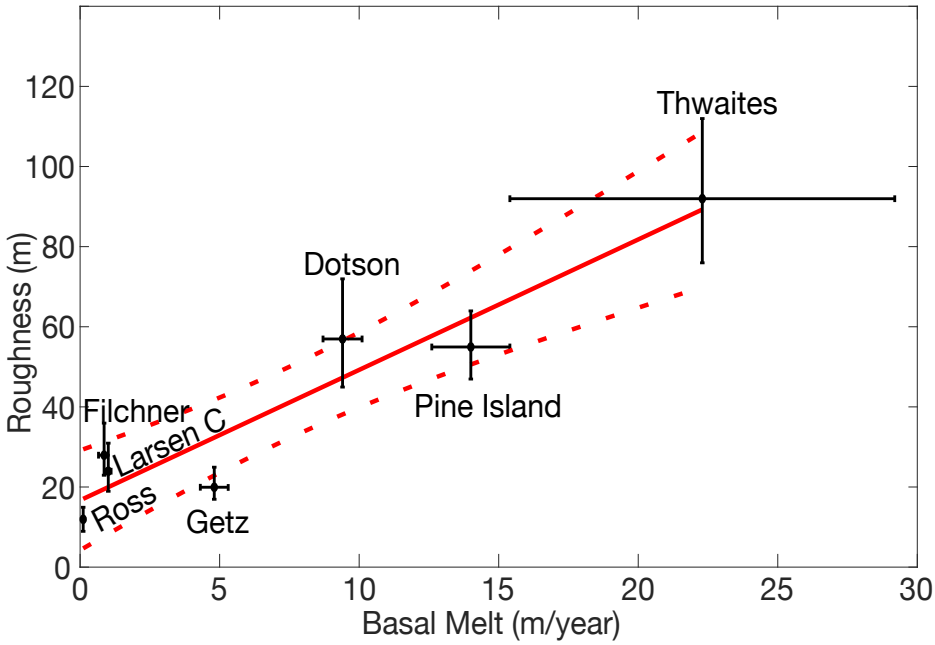


Figure 2.5: Least squares regression of basal melt and the average roughness of seven Antarctic ice shelves. Plotted in red is the best fit line with 95% confidence bounds

## 2.4 Discussion

Our results show a clear relationship between pinning points and roughness (Figure 2.2 and Figure A.1). Confining stresses associated with pinning points play a role nucleating crevasses and rifts and are involved in seeding the topographic expressions that eventually become rifts and melt channels (Still and others, 2018). Our results also show that roughness is increased relative to its *mean* over pinning points and other structural features, with very different roughness associated with these features between ice shelves (Figure 2.2 and Figure A.1). This, combined with the connection between roughness and basal melt, suggests basal melt might excavate localized topography, thereby enhancing roughness generated by pinning points and other features. Alternatively, refreezing in colder ocean environments, might fill topographic features, smoothing out the surface. This is similar to the mechanism

proposed by Bassis and Ma (2015a) where increased ocean-forcing excavates crevasses resulting in deeper and wider features, which is the inverse of processes on ice shelves over colder water where observations show marine ice filling suture zones between ice streams (Holland and others, 2009; Luckman and others, 2012). This hypothesis, however, contrasts with high-resolution, two-dimensional models of ice-ocean interaction within crevasses (Jordan and others, 2014). These models show that the pressure-dependence of the basal melt rate results in lower melt rates or refreezing within crevasses, implying that the ocean will smooth out features. More work is needed to disentangle the mechanisms responsible for the amplification of topography on the 1 m to 100 m scale, including (numerically expensive) three-dimensional models of circulation capable of resolving meter scale features.

Our results also indicate that roughness is strongly correlated with average basal melt rates beneath ice shelves. It is possible that the larger basal melt rates we observe are a direct consequence of the larger roughness. For example, the amount of energy transferred to the ice-ocean interface is often assumed to depend on roughness, albeit on millimeter-to-centimeter scales (Jenkins and others, 2010). Although the roughness-scale in turbulent energy transfer is much smaller than the scales we consider (and resolve), we also compared point estimates of roughness to basal melt rates (Adusumilli and others, 2020) for Pine Island, and found little correlation between basal melt rates across individual ice shelves and regions where the roughness across individual ice shelves is large. This implies that that the interplay between basal melt and roughness is the result of feedbacks that span large sections of ice shelves, rather than a purely localized response to increased basal melt. This hints that the increased roughness is at least partly caused by a change in the stress regime associated with increased basal melt. For example, increased basal melt may reduce

contact with pinning points and lateral margins, resulting in decreased buttressing that promotes crevassing. At the same time, basal melt channels seed crevasses (Vaughan and others, 2012; Favier and others, 2014) and crevasses may become excavated over time to become larger features such as melt channels.

Although we are unable to resolve anisotropy or directionality of roughness, increased basal melt appears to be associated with increased roughness across all scales. Instead of finding a strong spectral signature associated with different features, rough ice shelves are rough across a large range of wavelengths. This is broadly consistent with our hypothesis that increased basal melt alters the stress regime of the shelf, but does challenge our classification of features into ''basal melt channels" and "crevasses".

Our observations hint at complex interactions between the ice and ocean over a significant range of scales and features. Critically, however, roughness in ice shelves appears to be not only diagnostic of large basal melt rates, but correlates with ice shelves that are experiencing significant changes, including unpinning and grounding line migration (Favier and others, 2014; Milillo and others, 2019). This suggests that increased roughness may be an easily measurable proxy for ice shelf stability. Moreover, increased roughness associated with fracture and failure of ice might point towards future vulnerabilities to ice shelves to collapse through increased fracture and failure. Given that current ice shelf models predict much smoother topography than our observations indicate, we need to better understand the source and evolution of the topographic signature of roughness to better understand these links.

## 2.5 Conclusions

We find that roughness varies significantly within and between ice shelves. Pinning points, crevasses, melt channels, and rifts all increase roughness of ice shelves. Additionally, we find that the average roughness of ice shelves has a strong correlation with basal melt, with Amundsen Sea ice shelves that have experienced stark increases in ocean forcing, exhibiting the highest roughness. Moreover, we also find that the average roughness spectra of ice shelves approximately follow a power-law distribution with larger wavelength features having higher magnitude roughness, and smaller wavelength features having lower magnitude roughness. These results suggests that ocean-forcing is playing a dominant role in the evolution of roughness within and between ice shelves. The reason for this strong connection is less clear, but it hints that we will see continued transitions to rougher ice shelves as more ice shelves are subjected to increased basal melt rates. Crucially, the roughest ice shelves in our study have all experienced grounding line retreat and decreased buttressing, hinting at a direct connection between ocean forcing and the mechanical stability of ice shelves.

# CHAPTER III

# High Basal Melt Rates and High Strain Rates Lead to More Fractured Ice

This chapter is a manuscript currently under review for publication in *Journal of Geophysical Research: Earth Surface*.

## 3.1 Introduction

Ice shelves are floating slabs of ice that buttress and slow the flow of grounded ice into the ocean (Dupont and Alley, 2005; Gudmundsson, 2013). Ice shelves are also the primary conduits though which the Antarctic Ice Sheet discharges ice into the ocean. Across all ice shelves, this discharge takes place roughly equally between basal melting and iceberg calving (Rignot and others, 2013; Liu and others, 2015; Greene and others, 2022). Although not directly responsible for sea level rise, weakening ice shelves and ice shelf collapse can promote acceleration of grounded ice into the ocean, which does directly contribute to sea level rise (Scambos, 2004; Rignot, 2004; Rignot and others, 2019b). Moreover, ice shelf weakening and removal increases the susceptibility of ice sheets to marine ice sheet and marine ice cliff instabilities (Bassis and others, 2021a; Crawford and others, 2021). With the removal of ice shelves and the exposure of tall ice cliffs to the ocean, cliff collapse could lead to significant retreat

and sea level rise on decade to century time scales (Bassis and others, 2021b).

Because ice shelves are in contact with both the ocean and atmosphere, ice shelves are thought to be especially vulnerable to climate forcing (Obase and others, 2017). For example, the meltwater-triggered explosive-disintegration of sections of the Larsen ice shelf is thought to be related to hydrofractures driven by melt pond formation(Banwell and others, 2013). This breakup, which took place over only six weeks in 2002, is linked to atmospheric warming (both long term and near term) and highlights the speed at which ice shelves can collapse (Scambos and others, 2003; Scambos, 2004; Rignot, 2004; Rignot and others, 2019b; Robel and Banwell, 2019). By contrast, weakening of ice shelves in the much colder Amundsen Sea Embayment, like the Pine Island and Thwaites Ice Shelves, is thought to be linked to ocean forcing (Jenkins and others, 2018; Nakayama and others, 2019; Lhermitte and others, 2020; Watkins and others, 2021). Moreover, recent calving events on the Pine Island Ice Shelf have resulted in significant retreat of the calving front as well as an acceleration of grounded ice upstream of the grounding line (Arndt and others, 2018; Joughin and others, 2021).

Although observations indicate that melting ice shelves are retreating and, potentially, weakening (Jeong and others, 2016b; Liu and others, 2015; Alley and others, 2021), we don't yet understand the specific processes linking ice shelf demise to ocean forcing. Thinning marine ice and ice mélange, which can stabilize the rifting process (Kulessa and others, 2014; Larour and others, 2021), due to climate warming may reactivate dormant rifting. Ice shelf calving front retreat that causes ice shelves to retreat beyond the 'compressive arch' could lead to calving and possibly instability (e.g.,(Doake and others, 1998)). Furthermore, the erosion of pinning point contact due to the intrusion of warm waters underneath ice shelves (Still and others, 2018;

Wåhlin and others, 2021) can result in a decrease in buttressing and restraining forces that potentially cause crevassing, fracturing, and decreased mechanical stability (Favier and others, 2016; Wild and others, 2022). For instance, the formation of crevasses on ice shelves that eventually penetrate the entire ice thickness and become rifts (McGrath and others, 2012; Jeong and others, 2016b) can provide zones of weakness and may seed locations where the ice can fracture and fail.

Melting, in addition to sculpting channels, has been shown to alter existing crevasse penetration depths(Bassis and Ma, 2015b; Schmidt and others, 2023) and also promote the nucleation (or excavation) of surface and basal fractures at the apex of basal channels (Vaughan and others, 2012; Alley and others, 2016). As the depth of these crevasses and melt channels approach the ice thickness, the likelihood of calving increases (Bassis and Walker, 2011; Bassis and Jacobs, 2013). This hints that submarine melting may partially regulate and control crevasse penetration, which itself is related to rifting, iceberg calving, and overall ice shelf stability. Critically, all of the processes that impart crevasses and melt channels onto ice shelves may interact and conspire to reduce the the mechanical integrity of ice shelves. For instance, melt channels may seed crevasses and crevasses may initiate melt channels. Recently, Watkins and others (2021) showed that the roughness of ice shelves strongly correlates with basal melt rates. That study hinted that roughness, something easily measurable using remote sensing, might be a proxy for ice shelf vulnerability (Larter, 2022). However the specific mechanisms controlling roughness, and linking roughness across a range of scales to basal melt, remains unknown. Here we seek to bridge the gap between the complex processes occurring on ice shelves, such as melting and fracturing, and the size of features, such as melt channels and crevasses to better understand how they interact.

## 3.2 Data and Methods

### 3.2.1 Study Region

Our study focused on the Pine Island Ice Shelf (Figure 3.1a) because of the detailed data coverage, which were obtained via Operation IceBridge airborne campaigns, British Antarctic Survey campaigns, and others (Paden and others, 2010; Vaughan and others, 2012). In addition, Pine Island has experienced rapid grounding line retreat (Favier and others, 2016) and recent large calving events (Joughin and others, 2014; Liu and others, 2015; Arndt and others, 2018). Moreover, in a previous study Watkins and others (2021) found elevated roughness on the Pine Island Ice Shelf in regions surrounding melt channels, pinning points, shear margins and rifts. Here we examined two contrasting regions of the the Pine Island Ice Shelf in more detail. First, we examined the area surrounding a central flowline in the main trunk of the ice shelf containing documented melt channels (Vaughan and others, 2012; Shean and others, 2019) (blue box Figure 3.1a). Alley and others (2023) has defined basal melt channels as features typically $1-3$ km wide and $50\breve{}400$ m deep that occur where a plume of buoyant water melts a trough into the ice-shelf base.

In addition, we examined the area surrounding a flowline through the shear margin containing crevasses visible in satellite imagery (e.g., Lhermitte and others (2020)) and containing melt channels (Alley and others, 2019) (green box in Figure 3.1a). Most crevasses are taken to be narrow ($< 500$ m), penetrating fractures (Bishop and others, 2011; Ishalina and others, 2021), however some have been documented as being spaced between $0.5-2$ km and penetrating over 100 m deep (McGrath and others, 2012).

### 3.2.2 Ice Shelf Topography

We used gridded inferences of the ice shelf bottom obtained from BedMachine Antarctica Version 2 (Morlighem, 2019), part of NASA's Making Earth System Data Records for Use in Research Environments (MEaSUREs) program (Morlighem and others, 2019). The products used in constructing the BedMachine ice shelf bottom were collected between 1993 and 2016 (median year of 2012), and the grid posting of the data is 500 m.

Because we used ice shelf base data from BedMachine, ice shelf base data is limited by the hydrostatic assumption and thus both surface and bottom topography are proportional to ice thickness. Features less than 500 m in width are not resolved by the resolution of BedMachine and therefore not analyzed in this study. Moreover, the resolution of the data makes it challenging to resolve ice thickness and sub-ice thickness scale features so we do not attempt to correct the hydrostatic assumption to account for flexure. Although important, based on the power law found in Watkins and others (2021) these generally would have smaller magnitudes (penetration depths) than larger wavelength features resulting in a small roughness relative to the large wavelength features. As we are concerned with total roughness in this survey, small wavelength features would have small effects on this metric, and therefore can be safely ignored for the scope of this study.

Generally, for all ice bottom measurements (grounded and floating), errors associated with the BedMachine data products are around 30-40 m but could exceed 250 m in some sparsely surveyed regions (Morlighem and others, 2019). However, when we compare BedMachine data to high resolution Operation Ice Bridge data (Paden and others, 2010), we find that the mean absolute error of BedMahcine ice base measurements on the Pine Island Ice Shelf is approximately 30 m. This is likely

an overestimate as features are likely to have advected and (may have) evolved. We further compared features visible in the BedMachine data with features visible in satellite imagery in our survey regions and found excellent agreement indicating that the features we examine are robust and not artifacts of sparse data combined with the BedMachine inversion process.

#### 3.2.3 Flow lines through the main trunk and shear margin of Pine Island Ice Shelf

We traced two flowlines from the grounding line to the calving front of the Pine Island Ice Shelf using velocities from NASA's MEaSUREs data-set (Rignot and others, 2013). The flowlines were chosen to pass through the main trunk of the ice shelf, aligning with a basal melt channel (central flow line, blue box of Figure 3.1a), or the shear margin of the ice shelf, containing mostly crevasses (shear margin flow line, green box of Figure 3.1a). We also traced a sequence of transects perpendicular to the flow lines to sample both longitudinal and transverse to flow portions of basal melt channels and crevasses. Each transect is spaced approximately 500 m apart on the flow line and metrics (depth/width) are measured as an average across the transect).

#### 3.2.4 Strain rates and melt rates

Strain rates were calculated from surface velocity data derived using feature tracking between pairs of Sentinel-1 Synthetic Aperture Radar (SAR) images. Between October and December 2014, at the start of the EU Copernicus Program Sentinel-1 mission, 9 sequential images were acquired, enabling feature tracking between 8 image pairs separated by 12 days. Standard Gamma Software procedures were used (e.g. (Luckman and others, 2015)), feature tracking window sizes were 416 x 128 pixels ( 1 km in ground coordinates) and displacements were sampled every 50 x 10

pixels ( 100 m in ground distance). The resulting displacement fields were converted to velocity (divide by 12 to give meters per day), filtered using the signal to noise ratio, and geocoded to the standard polar stereographic coordinate system at a grid resolution of 100 m. The eight velocity maps were averaged to produce a smoother 2014 product and the magnitude of the first principal strain rate was calculated in a 9 by 9 neighbourhood from this projected velocity field. In addition, we also used first principal strain rate data obtained from Alley and others (2018) to perform a continent-wide analysis. Additionally, we used gridded melt rate products obtained from Adusumilli and others (2020), which used data between 2010 and 2018 and is posted at a grid resolution of 500 m. Where applicable, the melt rate and strain rate data are interpolated from the gridded products along the flow line.

#### 3.2.5 Depth, width and spacing of features

We defined "features" broadly as any topographic depression in the base of the ice shelf with width comparable or greater to the ice thickness. This includes melt channels and crevasses that are greater than 500 m in length. As we cannot resolve features smaller than 500 m due to data limitations, they are not considered in this study. We then characterized these features using the depth, width, and when applicable spacing between features (illustrated in Figure 3.1b). We defined the depth ($D$) of a feature as the average of the vertical distance between the two local minima (or in the case of channels, the deepest flanks) and the local maximum (or in the case of channels, the apex) of a feature on the ice bottom (red line in Figure 3.1b). The width of a feature ($W$) was defined as the horizontal distance between two local minimums in the ice bottom along a transect (white line in Figure 3.1b). We also defined the spacing between features ($\lambda$) as the horizontal distance between two local maximums in the ice bottom (black line in Figure 3.1b). This is taken as

the distance between features from left to right in the transverse direction. Because we are limited by the resolution of our data, in this study we examined features that are roughly wider than the scale of the ice thickness (approximately 500 m).

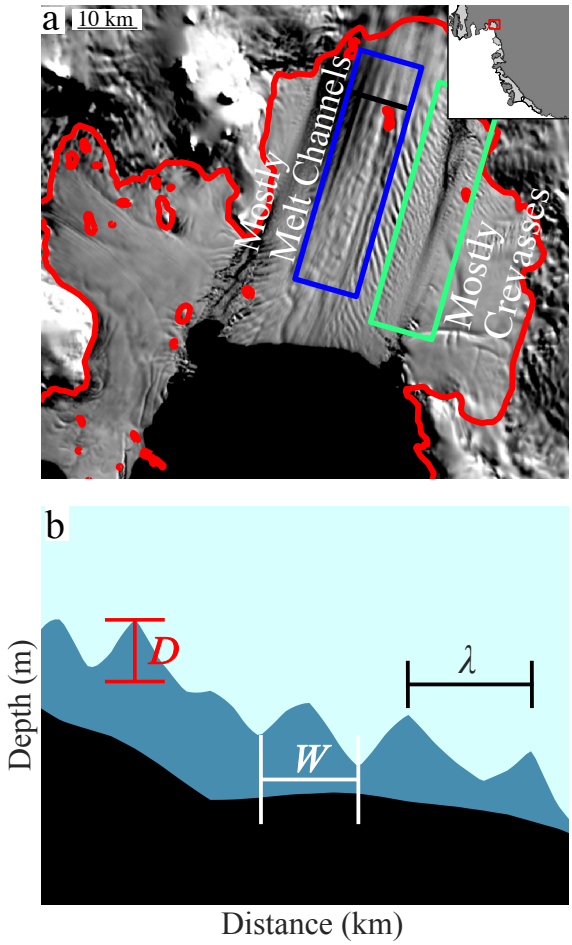


Figure 3.1: a) Map of the Pine Island Ice Shelf showing the location of a group of mostly melt channels in the central portion of the ice shelf (blue boxed region) and a group of mostly crevasses in the shear margin of the ice shelf (green boxed region). The black line inside the blue box represents the profile shown in b. The map inset represents the location on the Pine Island Ice Shelf (red box) within the Amundsen Sea Embayment in West Antarctica. b) Schematic showing how the depth ($D$, red), width ($W$, white), and spacing ($\lambda$, black) of features were measured.

### 3.2.6 Roughness

Roughness is defined here as topographic variations in the ice base varying from crevasses to large melt channels and rifts. As in Watkins and others (2021), we

followed Whitehouse (2004) and quantitatively defined roughness in a given direction (units meters) using the square root of the integral of the power spectral density $S(k)$ (units $m^3$):

$$R = \sqrt{\int_{k_1}^{k_2} S(k)dk}. \tag{3.1}$$

Here, $S(k)$ is the power spectral density of the ice shelf base, which is obtained using a continuous wavelet transform (Sifuzzaman, 2009; Watkins and others, 2021). The power spectral density is a measure of a how much power (or magnitude) a given profile as a function of wavelength (or wavenumber)(Stoica and Moses, 2005). In addition, $k$ (1/m) represents the wavenumber, defined as the inverse of wavelength, and $k_1 = 10^{-4}$ (1/m), $k_2 = 2 \times 10^{-3}$ (1/m) represent the bounds of integration in wavenumber that define the portion of the spectrum over which roughness is calculated. These bounds correspond to wavelengths between $\sim$ 500 m and $\sim$ 10 km. We also defined the along-flow ($R_x$) and transverse-to-flow ($R_y$) roughness for each point on the flowlines. The roughness at a given point is then defined as:

$$R = \sqrt{R_x^2 + R_y^2}. \tag{3.2}$$

This definition of roughness includes topographic variation both normal to and orthogonal to the flowline. We did a sensitivity study where we calculated roughness along different orthogonal directions and found that the total roughness, defined by Eqn. 3.2, was insensitive to the orientation of the axes. In addition, by defining roughness in this way, we can generate a 2D gridded roughness map of the entire ice shelf (Supplementary Figure B1).

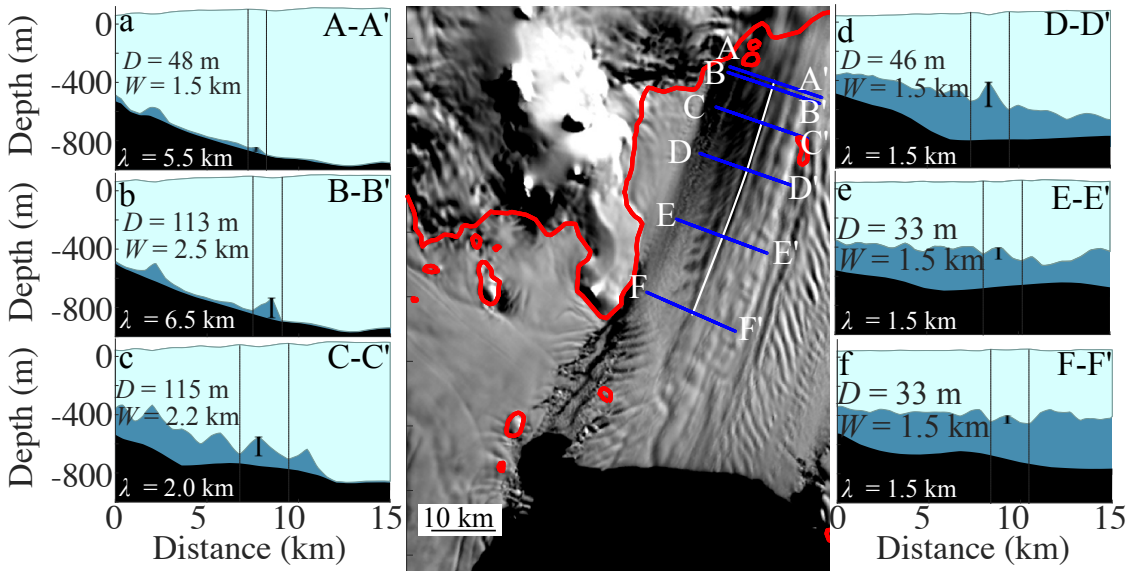


Figure 3.2: Melt channel growth and decay on the Pine Island Ice Shelf. Panels a-c show the initial growth in width and depth and decrease in spacing as channels advected downstream of the grounding line. Panels d-f show the later decrease in depth of the channels with near constant width and spacing further down the profile. The red line on the map indicates the grounding line. The black vertical lines in each panel show the domain of a single feature as it evolves between panels.

## 3.3 Results

### 3.3.1 Central flow line

We first examined a region on the Pine Island Ice Shelf where a series of melt channels that are aligned mostly in the along flow direction have been identified (Vaughan and others, 2012; Shean and others, 2019). We tracked the depth, width, and spacing of channels using a sequence of transects, both along and transverse to the flow line. The transects, which are depicted by the various panels in Figure 3.2, started from their origin near the grounding line. These transects along the flow line approached the calving front, where we could no longer identify undulations in basal elevation.

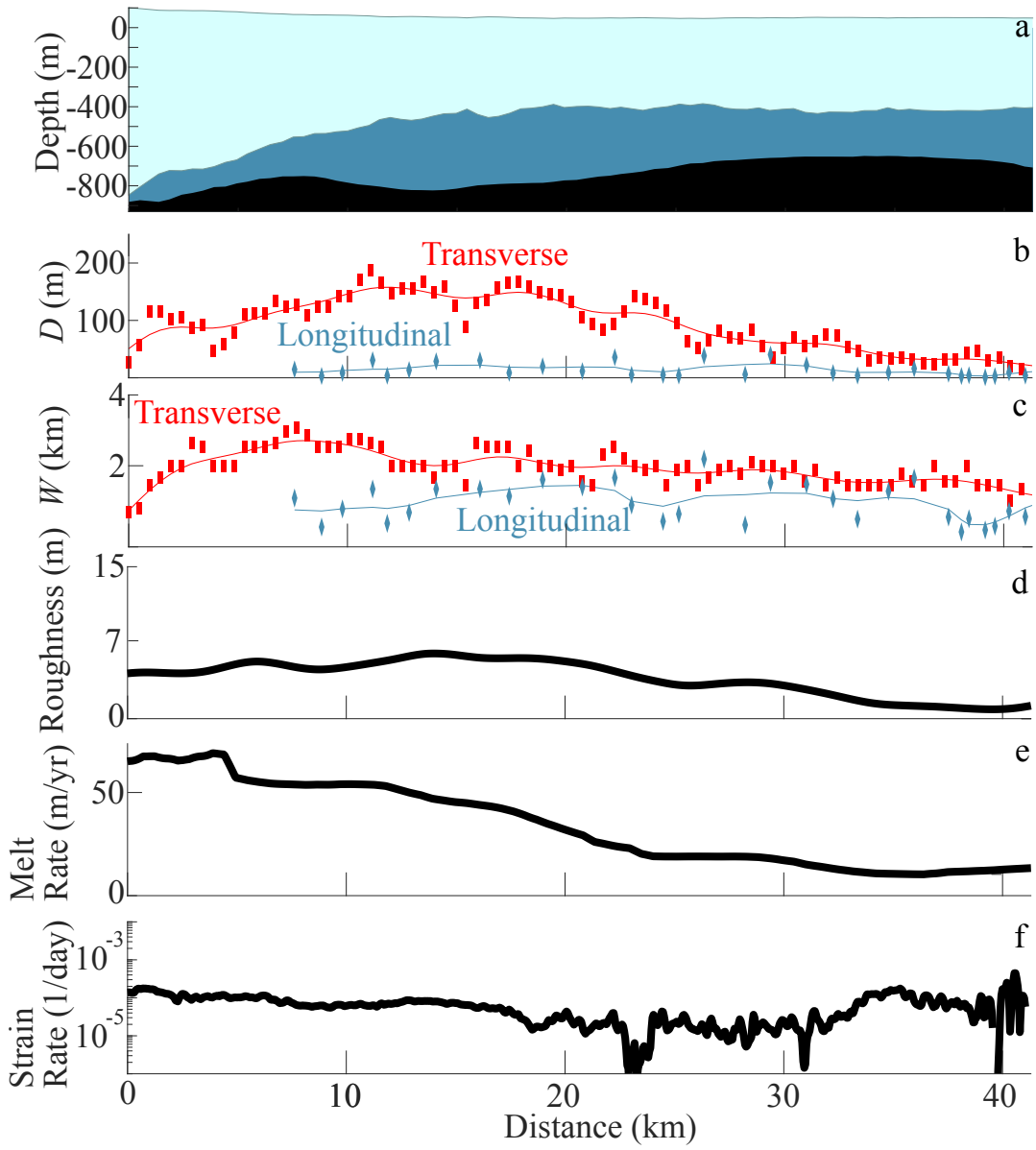


Figure 3.3: a) The along flow profile of the flow line (white line) shown in Figure 3.2 extending from the grounding line to the calving front. b) The transverse (red) and longitudinal (blue) depth of features on the ice shelf. The solid lines represent a moving mean of the data points. c) The transverse (red) and longitudinal (blue) width of features on the ice shelf. Solid lines represent a moving mean of the discrete measurements. d) The roughness of all features along the flow line on the ice shelf. e) The melt rate along the flow line. f) The first principal strain rate along the flow line.

**Channels grow rapidly, then decay**

From Figures 3.2a-b, we see the central channel that initiated near the grounding line deepened and widened rapidly, nearly doubling in depth from $\sim 48$ m to $\sim 113$

m and widening by $\sim$ 1 km (1.5 km to 2.5 km). These increases happened after only 1 km of flow distance, with channel spacing remaining roughly 6 km. As additional channels formed between the initial channels, the channel spacing decreased to $\sim$ 2 km (Figure 3.2c). The channels in the panel reached both their maximum depth ($\sim$ 115 m) and maximum width ($\sim$ 2.5 km) about 15 km downstream from the grounding line (Figure 3.2c). The width and depth of channels then decreased (Figure 3.2c-d), but the channel spacing remained roughly constant at $\sim$ 1.5 km. Further downstream, the depth further decreased until we could no longer identify the channels in the ice shelf bottom (after Figure 3.2f).

By contrast, we see little change to the width or depth of features in the longitudinal-to-flow profile from the grounding line to the calving front front (Figure 3.3a-c). We found that as expected, on average, the transverse-to-flow profiles (blue lines in Figure 3.2) were deeper ($\sim$ 83 m) and wider ($\sim$ 2.0 km) than their longitudinal to flow (white line in Figure 3.2) counterparts ($\sim$ 14 m depth and $\sim$ 1 km wide). We also computed roughness (Figure 3.3d) and because the depth of features was much smaller longitudinal-to-flow than in the transverse-to-flow direction (Figure 3.3b), roughness (which includes both directions) followed a similar trend to transverse-to-flow depth (Figure 3.3d).

**Comparison between central flow line features (channels), melt rates, and strain rates**

To better understand what drives channel growth and decay, we next compared the melt rate and largest principal strain rate to the depth, width, and roughness derived along the channel (Figure 3.3e-f). The melt rate along the channel was variable, ranging from over 50 m/yr to nearly $\sim$ 0 m/yr, with much of the high melt occurring within the first 25 km of ice flow. This corresponded with widening and deepening of all channels. The channels then started to decrease in depth as the melt

fell below $\sim$ 25 m/yr. This is likely related to no melting/freeze-on in the channel and high melting on the channel flanks (Dutrieux and others, 2013; Humbert and others, 2022).

In contrast, the strain rate along the channel was nearly constant, with a mean value of $1 \times 10^{-4}$ 1/day, not exceeding $2 \times 10^{-4}$ 1/day and rarely dropping below $0.5 \times 10^{-5}$ 1/day. We also examined the smallest principal strain rate. Smallest principal strain rates aligned roughly transverse to the channel and were, on average, smaller and negative (approximately $-1 \times 10^{-5}$ 1/day). This indicates that the channel closing is due to the (small) compressive strain rates. This secondary flow acting to close the channel is what we expect based on modeling studies (Bassis and Ma, 2015b).

### 3.3.2 Shear margin flow line

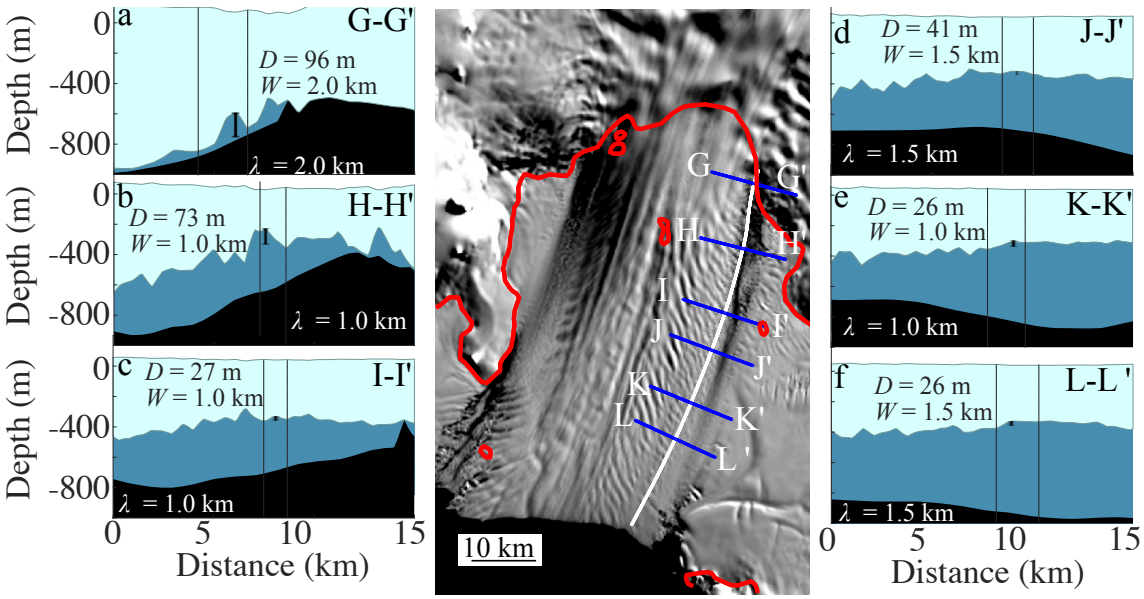


Figure 3.4: Feature growth and decay in the shear margin of the Pine Island Ice Shelf. Panels a-b show a growth in features, which resulted in an increase in width and depth and a decrease in spacing. Panels c-f show a shrinking of the features which resulted in a decrease in depth and little change in width and spacing. The red line on the map indicates the grounding line. The black vertical lines in each panel show the domain of a single feature as it evolves between panels. Note that the transects shown here are different than the transects shown in Figure 3.2.

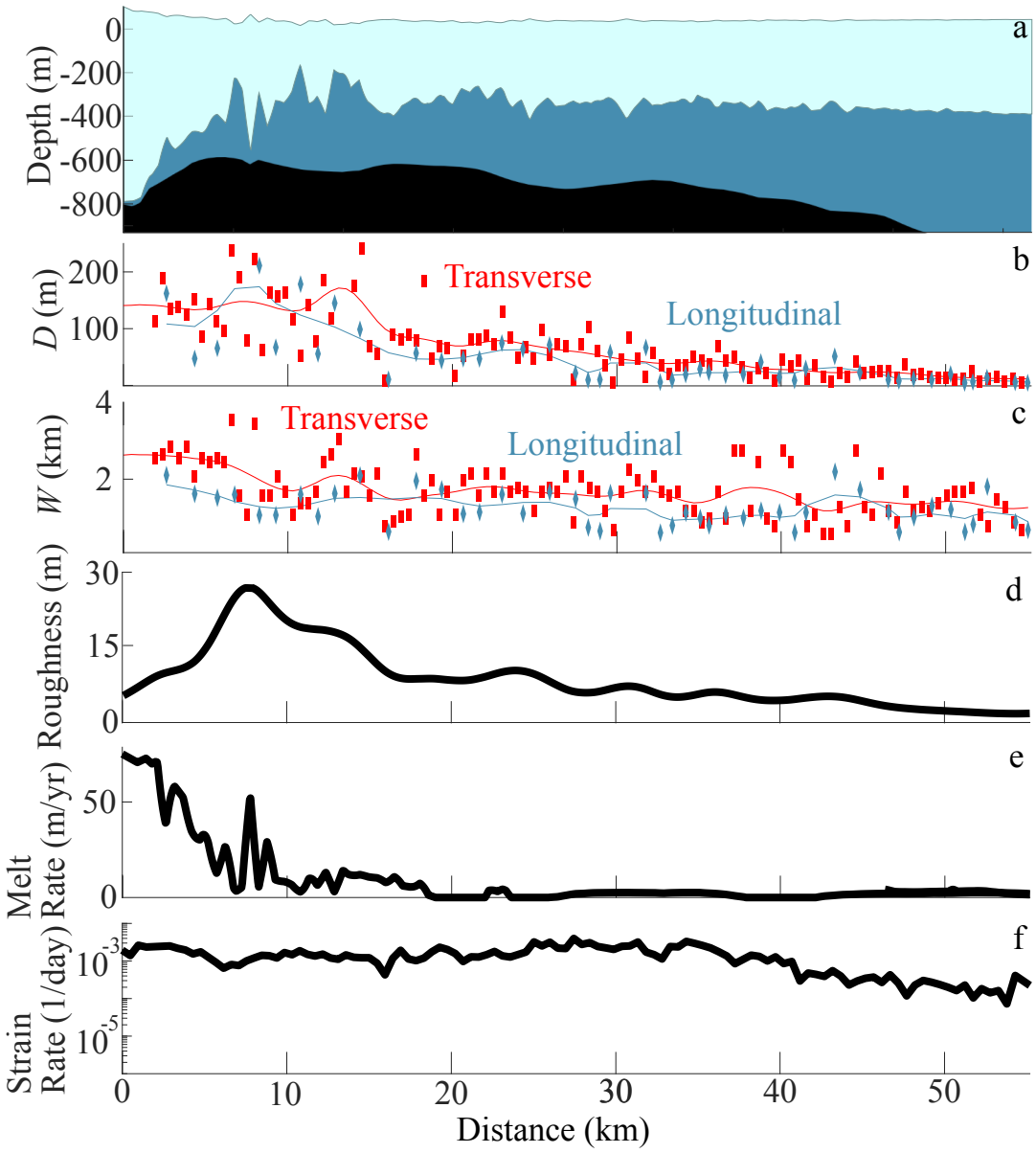


Figure 3.5: a) The along flow profile of the flow line extending from the grounding line to near the calving front (white line shown in Figure 3.4). b) The transverse (red) and longitudinal (blue) depth of features on the ice shelf. Here, the solid lines are a moving mean and the data points are the discrete measurements. c) The transverse (red) and longitudinal (blue) width of features on the ice shelf. Again, the solid lines are a moving mean and the data points are the discrete measurements. d) The roughness of all features along the flow line on the ice shelf. e) The melt rate along the flow line. f) The first principal strain rate along the flow line.

To contrast with the melt channels, we also examined profiles along the shear margin of the Pine Island Ice Shelf where heavily crevassed sections of the ice shelf

are prevalent (Figure 3.1a, and Figures 3.4-5). We again tracked the width, depth, and spacing of features in the margin using transects both along and transverse to the flow line. The transects are once again depicted by various panels (Figure 3.4), and started from their origin near the grounding line and then ran to near the calving front, where we could no longer identify the features in the margin flowline (channels and crevasses).

**Features in the margin deepen then decay**

Examining a series of transverse to flow profiles (Figure 3.4) we found that transverse features, similar to channels, formed as soon as the ice became buoyant at the grounding line. Between their initiation (Figure 3.4a) and the halfway point of the flow line (Figure 3.4c), the features reached a maximum depth of $\sim$ 160 m and maximum width of $\sim$ 2.0 km. After this point, the features appeared to be quasi-steady state (or uncharged upstream/downstream of a particular point along a flow line), with nearly constant width and depth (mean width of 1.5 km and mean depth of 26 m). The transverse to flow features had a characteristic spacing of $\sim$ 1.5 km between features. This pattern of evolution mimicked what we found for the transverse profiles of the central flow line (melt channels).

Like the central flow line, features in the shear margin were on average wider in the transverse to flow direction ($\sim$ 2 km, Figure 3.3c) as opposed to the along flow direction ($\sim$ 1 km, Figure 3.3c). In contrast to the central flow line containing mostly melt channels, in the shear margin the mean feature depth in both the longitudinal and transverse to flow directions was $\sim$ 46 m and $\sim$ 67 m, respectively. The values in the longitudinal direction are larger than observed for melt channels and are indicative that features cut across the flow line an angle, rather than being aligned in the flow direction as the channels are. Elevated feature depth in both directions

results in a roughness nearly double that of the melt channel region (11 m vs 6 m), showing that rougher features are tied to features which are deeper (in both directions). As before, as the ice flowed towards the calving front, the feature depth and the roughness decreased. We also found that the width of the features in the transverse direction decreased from $\sim 3.5$ km to $\sim 1$ km along the profile, while the width of the same features in the longitudinal direction was nearly constant at $\sim 1.0$ km.

#### Comparison between shear margin features, melt rates, and strain rates

Similar to the central flowline, we compared the width and depth of features to melt rates and strain rates. Melt rates are highest near the grounding line ($\sim 65$ m/yr), but melt rates fell off rapidly downstream to nearly 0 m/yr (Figure 3.5e). Over this interval, shear margin features (crevasses and channels) continued to deepen both transverse and longitudinal to flow. By contrast to the central flowline, the strain rate is over an order of magnitude higher than we saw in the melt channel region ($1.3 \times 10^{-3}$ 1/day vs $1 \times 10^{-4}$ 1/day). This strain rate varied along the profile, ranging over two orders of magnitude from $4 \times 10^{-3}$ 1/day to $5 \times 10^{-5}$ 1/day (Figure 3.5f). The elevated strain rate corresponded with a significant growth of features in both directions and this growth seems to be especially pronounced in regions that also experienced high melt rates.

## 3.4 Discussion

### 3.4.1 Comparison between features in the central flow line and shear margin flow line

Our analysis supports evolution patterns for basal melt channels consistent with previous studies where channels initiate near the grounding line, deepen downstream in the presence of large basal melt rates, and then begin to close as they advect to

regions with lower melt rates (Alley and others, 2016; Marsh and others, 2016). We found that basal melt channels on the Pine Island Ice Shelf typically have widths that range between $1-3$ km, consistent with previous studies (Rignot and Steffen, 2008; Vaughan and others, 2012). We also determined a characteristic spacing between channels that varied between $2-6$ km near the grounding line, with the range narrowing to $1-2$ km once the channels were fully formed downstream. The decrease in width is a result of the appearance of channels between the initial channels. This spacing is also similar to the range of spacing estimated based on a linear stability analysis of channel formation (Dallaston and others, 2015).

Somewhat surprisingly, we find similar patterns between the features in both the central and shear margin flow lines. However, features in the margin (combinations of crevasses and channels) are more than twice as rough as features in the central flow line (channels) and experience much higher strain rates. Nonetheless, shear margin features also initiate near the grounding line, deepen rapidly, and then become shallower as they advect to the calving front. For both the central flow line and shear margin flow line, we speculate that that bed geometry around the grounding line may act as an initiation point for features. This hypothesis comes from a qualitative analysis of the initiation of features with respect to the underlying bed in which the bed has a similar shape to the recently formed feature (leftmost feature Figure 3.2a and rightmost feature in Figure 3.4a). This formation is consistent with previous studies (Gladish and others, 2012; Sergienko, 2013; Jeofry and others, 2018), however uncertainties in the grounding line location limits us from performing more than a speculative analysis. Likewise we also see locations with little obvious signs that bed topography controls the initiation of features. For basal melt channels, subtle effects like sub-glacial discharge(Gladish and others, 2012; Dallaston and others,

2015) or unresolved bed topography(Sergienko, 2013) could trigger the in stability and suggests that large variations in bed geometry are not necessary for channel initiation, but can influence where a channel may form if they exist.

The features we analyzed here represent a small fraction of the ice shelf and only a limited portion of the spectrum of features quantified by Watkins and others (2021). We extended the analysis of roughness across the entire ice shelf. Figure 3.6 shows shows the depths and widths of all features measured in this survey. We found that the scaling (power law) from Watkins and others (2021) continues to hold, with a measured scaling parameter statistically the same in both cases. In addition, we see that there is a continuous distribution of features without clear clustering along the entire spectrum.

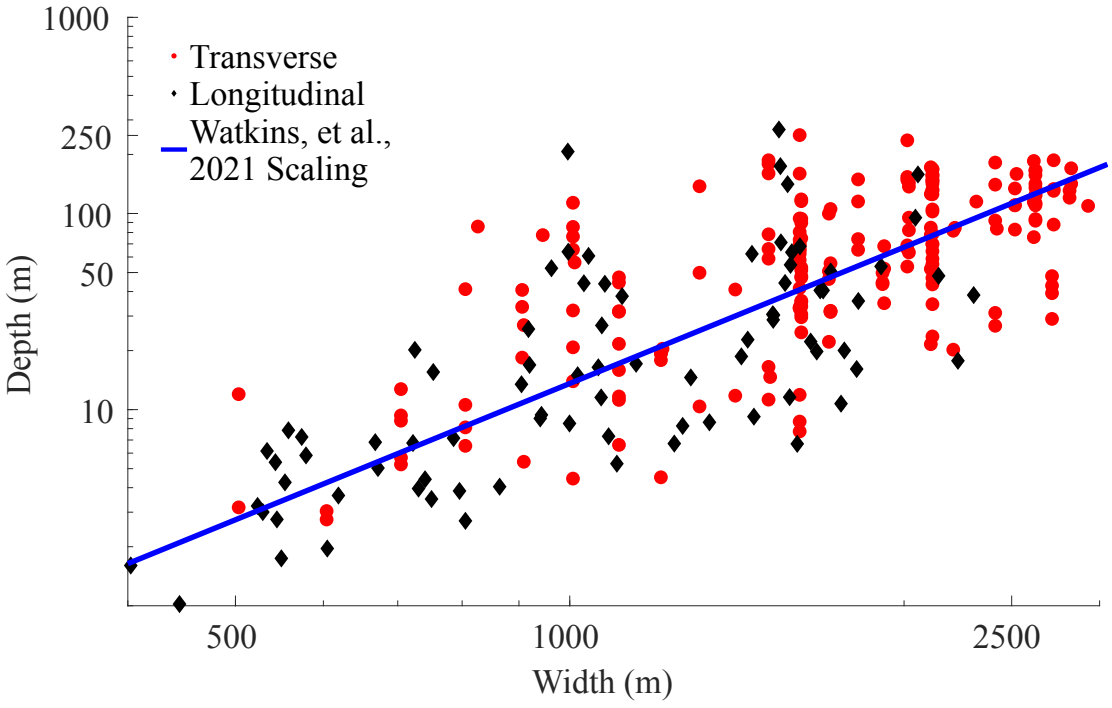


Figure 3.6: Width vs Depth of all features considered in this study. The black diamonds represent longitudinal features while the red dots represent transverse features. Note that the scaling here (data points, slope $\approx 2.2$) is nearly the same as in Watkins and others (2021) (blue line, slope $\approx 2.3$), in which the scaling follows a power law.

This scaling is intriguing because it supports the hypothesis that melt channels and crevasses exist on a continuum and overlap on the spectrum of features. Because some melt channels may fracture and become large crevasses and because some crevasses may melt and become small melt channels, both sets of features cannot be easily (or statistically) separated into distinct populations. This indicates that, although the features we identified can be roughly classified as "channels" and "crevasses" there are many more features across the ice shelf that have depth/width combinations that are between these two end members. However, the relationship between width and depth for the entire menagerie of features still roughly follows a power-law. Moreover this result, which shows that melt channels and crevasses fall on different ends of a scaling spectrum, could potentially show us how we might differentiate between crevasses and channels from (relatively coarse resolution) satellite data.

### 3.4.2 High melt rates and high strain rates trigger deeper channels and crevasses

To better examine the link between melt channels and crevasses, we analyzed the contribution of strain rate and melt rate to feature roughness. From Figure 3.5, we see that features are deepest in all directions when both melt rates and strain rates are high. To further examine this connection, we examined the relationship between strain rate, melt rate and roughness for all points on the Pine Island Ice Shelf (Figure 3.7a). This includes not only the melt channels and shear margins examined in our study, but also intermediate features that are not obviously melt channels or crevasses. From Figure 3.7a, we see four distinct quadrants. When both melt rate and strain rate were low (bottom left quadrant of Figure 3.7a), roughness was lowest ($\leq$ 5 m). When only melt rate is high (top left quadrant of Figure 3.7a) or when only strain rate was high (bottom right quadrant of Figure 3.7a), the roughness was

moderate (between 5 m and 20 m). Finally, the highest roughness occurred when both strain rate and melt rate were high (top right quadrant of Figure 3.7a).

For Pine Island, the strain rate threshold where we see a dramatic increase in roughness occurs at $\sim 0.001$ 1/day, consistent with an approximate range of both *in situ* and remote sensed values of strain rate needed for crevasses initiation (Scott and others, 2010; Wearing and others, 2015). This strain rate corresponds to a deviatoric stress of 200 kPa, which is similar to the yield strength inferred by Vaughan (1993), although this result may vary between ice shelves. Overall, these results suggest that large roughness is closely related to both crevassing and intense melting of ice.

To determine if our hypothesis that roughness is highest when both melt rate and strain rate are large, we expanded our analysis and used first principal strain rate data from Alley and others (2018) along with melt rate data from Adusumilli and others (2020) from across all Antarctic ice shelves where we had sufficient data. We then performed the same analysis as on Pine Island (Figure 3.7b). This result shows a similar trend to Figure 3.7a and suggests that results of this study are applicable to all ice shelves, and not just Pine Island.

Based upon the results of Figure 3.7, we speculate that feature (crevasses and melt channels) formation and propagation on ice shelves is correlated with and may be largely controlled by processes such as melt and fracture. Melting is likely to carve basal melt channels into the base of ice shelves, especially where ice thickness is high and warm ocean waters are able to intrude. Similarly, where strain rates are high, the ice will fracture causing crevasses (and eventually rifts) to form. Then, melt and fracture also may work in combination to both fracture existing channels and melt existing crevasses, thereby exacerbating the roughness and potentially decreasing the ice stability.

### 3.4.3 Mechanisms for feature formation on ice shelves and implications for ice shelf stability

Based on the link between high roughness and the combination of high strain rates and melt rates, we hypothesize that high melt rates provide the seeds for melt channel formation near the grounding line (Figure 3.8 a-a'). However, in regions where strain rates (and stresses) are also sufficiently large to trigger ice fracture, these melt channels will also seed basal crevasses and fracturing events (Figure 3.8 b-b'). This is similar to the mechanism proposed by Bindschadler and others (2011) in which they speculate that warm water (in the form of basal melting) can form channels which trigger basal crevasses, or basal crevasses form and are exacerbated by warm water to form channels. Alternatively, in regions where the melt rate is high enough, basal crevasses that form near the grounding line could be more easily excavated by high melt, growing deeper as they advect.

Either way, the combination of high melt rates and high strain rates results in increased quantity and deeper penetrating melt channels and crevasses on ice shelves. Similarly, portions of channels/crevasses that are not being eroded by basal melting can also trigger basal crevasses, assuming strain rates are sufficiently high (Figure 3.8 c-c') (Scott and others, 2010). However, in the absence of both high melt rates and high strain rates, deformation of the ice will cause topographic features to relax (Bassis and Ma, 2015b) (Figure 3.8 d-d'). Alternatively, crevasses (and melt channels that have crevasses within (Vaughan and others, 2012)) can then propagate and turn into full thickness rifts, which eventually propagate across the ice shelf to isolate an iceberg, thereby triggering calving event. Increased rifting can result in decreased stability and increased vulnerability of the ice shelf to disintegration (Liu and others, 2015; Dow and others, 2018). This hints that increased melting may be

tied to increased ice shelf vulnerability though the promotion of rifting, similar to the mechanism proposed in (Alley and others, 2019). However, further work remains in identifying the links between the penetration depth of deep features on ice shelves and increased rifting, increased calving, potential ice shelf disintegration.

## 3.5 Conclusions

Our results build on previous studies that highlight the link between ocean forcing and ice shelf stability. Consistent with previous studies, we find that high melt rates promote basal melt channels with depths and widths broadly comparable to previous studies. Somewhat surprisingly, we also found that features in the margin have similar characteristics to features in the central flow line, although these features are deeper in all directions. This results in a roughness that is nearly a factor of two bigger. In fact, we find that the combination of high melt rate and high stain rate yield the roughest sections of the Pine Island Ice Shelf where features such as melt channels and crevasses penetrate the deepest in all directions. This result also holds when applied to all Antarctic ice shelves, highlighting the robustness of this survey. Our results point to basal melt and strain rate contributing together towards deeper penetrating features on ice shelves. We speculate that these rough features then may promote increased fracturing of ice and therefore a potential for increased vulnerability to retreat and failure. However, further work remains in directly tying roughness — shown here to be a proxy for the presence of basal melt channels and crevasses — to increased calving and ice shelf instability. Larter (2022) recently suggested that roughness may in fact be a health bar for ice shelf vulnerability and expansion to other ice shelves across all of Antarctica and elsewhere may prove useful in diagnosing which ice shelves may be susceptible to future instabilities and

collapse.

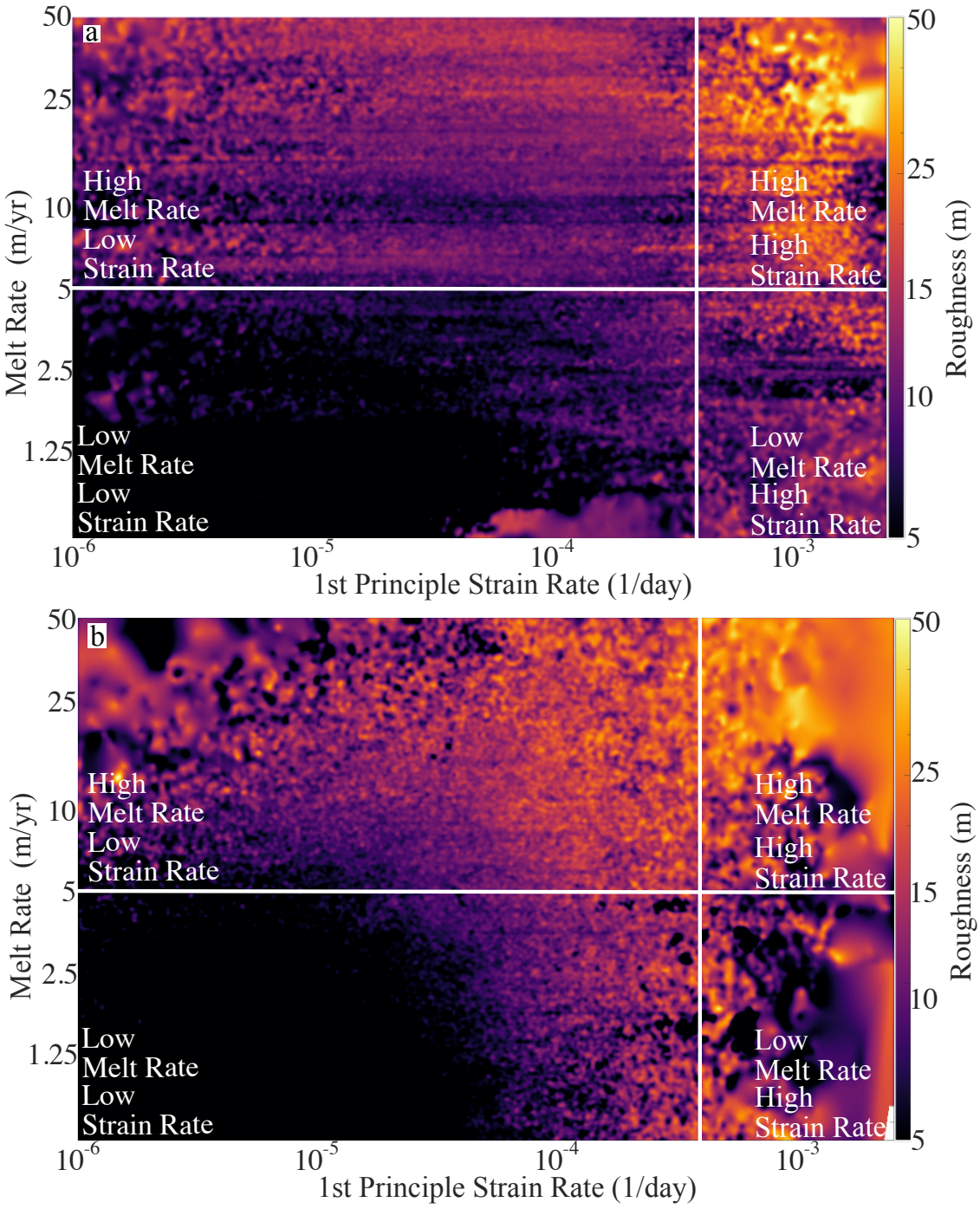


Figure 3.7: a) The relationship between the 1st principal strain rate , melt rate, and roughness for the Pine Island Ice Shelf. This figure was created by taking all melt rate, strain rate, and roughness data across Pine Island. Using this scatter data, a nearest neighbor interpolation was done on strain rate and melt rate grids to produce the gridded roughness that is a function of strain rate and melt rate. Note that other interpolation methods were done as well as just plotting the scatter data itself, and the trend remained the same in each case. We find results cluster in 4 distinct quadrants, with only the upper right quadrant with high melt rates and high strain rates resulting in high roughness. b) The relationship between the 1st principal strain rate , melt rate, and roughness for the all Antarctic ice shelves, this time using strain rates obtained from Alley and others (2018).

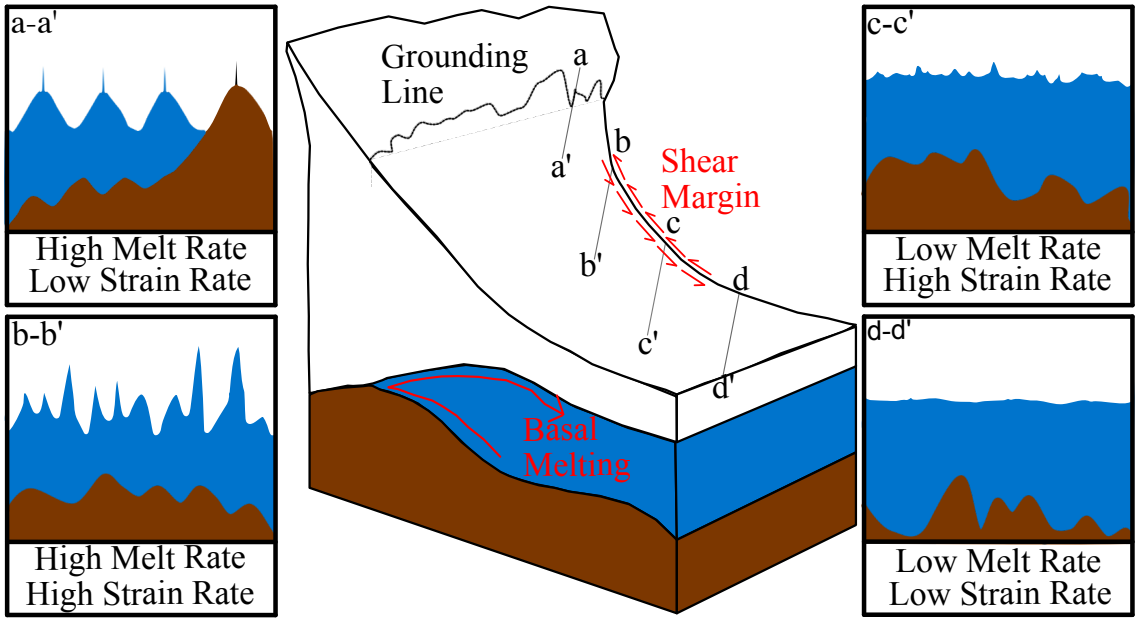


Figure 3.8: An illustration of the roughening (then smoothing) of an ice shelf. Each of the grey lines represents a transect of the ice taken at an angle to the flow direction. a) High basal melt rates near the grounding line roughen ice shelves by carving channels. b) These channels then fracture in high strain rate environments., such as shear margins. c) As the melt rate decreases toward the middle of the ice shelf and the ice thins, channels disappear. d) Finally, when strain rates are no longer high the ice has low roughness at horizontal scales greater than 500 m .

# CHAPTER IV

# Increases in Ice Shelf Roughness Precede Ice Shelf Retreat and Disintegration

This chapter is a draft manuscript currently in preparation for publication in the *Journal of Glaciology*.

## 4.1 Introduction

The stability of the Antarctic Ice Sheet is closely tied to the permanent, floating sections of ice that fringe the ice sheet's coast, known as ice shelves. Ice shelves play a critical role in buttressing and slowing the discharge of grounded ice from the Antarctic Ice Sheet into the ocean (Dupont and Alley, 2005; Gudmundsson, 2013). Ultimately, the potential loss of ice shelves due to changing environmental conditions has the potential to lead to significant increases in sea level rise (Rignot and others, 2019a). This is because when ice shelves that buttress grounded ice catastrophically fail, they lose their buttressing effect, causing land-based ice to speed up and increase the discharge of grounded ice into the ocean (Scambos, 2004; Rignot, 2004). One well-documented example of this is the Larsen B Ice Shelf collapse in 2002, which occurred due to atmospheric warming-triggered hydro-fractures (Banwell and others, 2013). The ice shelf collapsed over a four-week period, (Pritchard and Vaughan,

2007), highlighting the speed at which ice shelves can collapse (Scambos and others, 2003). The loss of the ice shelf triggered a four-fold acceleration from the tributaries that fed the ice shelf, highlighting both the vulnerability of ice shelves and the critical role that ice shelves play in stabilizing grounded ice sheet discharge Rignot (2004).

Ice shelves currently lose mass through a roughly equal combination of basal melting and iceberg calving (Rignot and others, 2013; Liu and others, 2015; Greene and others, 2022). Moreover, when environmental impacts, such as atmospheric or oceanic warming, increase melting, these changes have been linked to increased calving(Arndt and others, 2018; Joughin and others, 2021). Predicting the timing, location, and processes responsible for the retreat and collapse of ice shelves, however, remains challenging. Recent studies have shown that ice shelves in the Amundsen Sea Embayment in West Antarctica are particularly vulnerable (Jenkins and others, 2018; Martin and others, 2019). Due to warming ocean waters, ice shelves such as Pine Island, Thwaites, and Crosson have shown noticeable grounding line retreat (Jenkins and others, 2010; Khazendar and others, 2016; Seroussi and others, 2017). The grounding line of Pine Island, for example, retreats $\approx$ 120 m/year, the grounding line of Thwaites $\approx$ 450 m/year, and the grounding line of Crosson $\approx$ 280 m/year, which are some of the highest rates across the continent (Konrad and others, 2018). In addition, since 2003, Pine Island has lost $\approx$ 17 percent of its area, while the floating portion of Thwaites Glacier has lost $\approx$ 70 of its area (Greene and others, 2022). The shear margin of Pine Island has also become significantly more damaged in the past decade (Lhermitte and others, 2020).

In addition to the Amundsen Sea, other ice shelves across Antarctica have also seen major change or collapse since 2000. For example, the Larsen B collapsed in 2002 with remnants of the ice shelf collapsing in 2022, following unusually warm tem-

peratures (Wille and others, 2022). Similarly to Larsen B, the Wilkins Ice Shelf in West Antarctica disintegrated in 2008, potentially driven by hydro-fracture (Scambos and others, 2009). Additionally, other studies have indicated that a handful of ice shelves in East Antarctica, particularly those in Wilkes Land such as Moscow University and Totten ice shelves, may also be at risk of change (Stokes and others, 2022). Furthermore, the Conger ice shelf notably experienced collapse in March of 2022, perhaps in association with an atmospheric river and above average temperatures(Horton, 2022).

Recent studies have shown that roughness—a measurement of bumpiness for the surface or bottom of ice shelves—is associated with both basal melting and fracture (Watkins and others, 2021; Larter, 2022). Melting can carve melt channels into the ice (Stanton and others, 2013; Dutrieux and others, 2013; Gourmelen and others, 2017) as well as excavate existing crevasses (Bassis and Ma, 2015a). Alternatively, fracture can create crevasses that may eventually propagate through the entire ice shelf thickness to become rifts (McGrath and others, 2012; Jeong and others, 2016b), as well as form at the apex of melt channels (Vaughan and others, 2012; Alley and others, 2016). Critically, roughness has been shown to quantify the magnitude of these features, with the roughest sections of ice shelves coinciding with high melt regions (full of melt channels) and high strain regions (full of crevasses). Elevated amounts of melt and fracture however do not necessarily indicate instability. Moreover, some ice shelves naturally experience elevated melt and fracture, have high roughness, and have not seen thinning or area loss over large periods of time. A prime example of this is the Drygalski Ice Tongue, which is filled with melt channels, crevasses, and rifts, but has not shown signs of significant thinning or area loss (Rignot and others, 2013; Indrigo and others, 2020; Greene and others, 2022).

Here, we hypothesize that increases in the roughness of ice shelves may be indicative of their potential vulnerability. To this end, we have conducted an analysis of satellite (ICESat,ICESat-2), airborne survey (Operation IceBridge), and digital elevation model (REMA) data collected over the past two decades, focusing on 20 ice shelves across Antarctica. We start by examining the difference between roughness and change in roughness for the ice shelves in our survey. Then, we examine which ice shelves have roughened the most and attempt to link changes in roughness to changes in ice shelf area, thickness, and volume. This allows us to identify which ice shelves are undergoing the most change and speculate on using roughness to help identify the potential vulnerability of these regions on the continent.

## 4.2 Materials and Methods

### 4.2.1 Study Region

We conducted our analysis on a selection of 20 ice shelves from across the Antarctic Ice Sheet (Figure 4.1). This selection includes ice shelves located in the Amundsen Sea Embayment, a well-studied region with glaciers that are currently experiencing dramatic changes (Jenkins and others, 2018). Our analysis also includes the largest ice shelves across the continent (Ross, Filchner-Ronne, Amery, and Larsen C) which are generally considered stable but comprise a significant percentage of the ice shelf mass in Antarctica. In addition, we included ice shelves in Wilkes Land, East Antarctica (West, Shackleton, Conger, Totten, Moscow University) as recent research has suggested some of these ice shelves may be more vulnerable to change relative to others in East Antartica(Stokes and others, 2022). Finally, we also included the George VI, Land, Drygalski, Lazarev, and Brunt ice shelves because these ice shelves were relatively well sampled and filled in the gaps between the other sampled regions. Moreover, some of these ice shelves, such as Brunt and Drygalski, have experienced

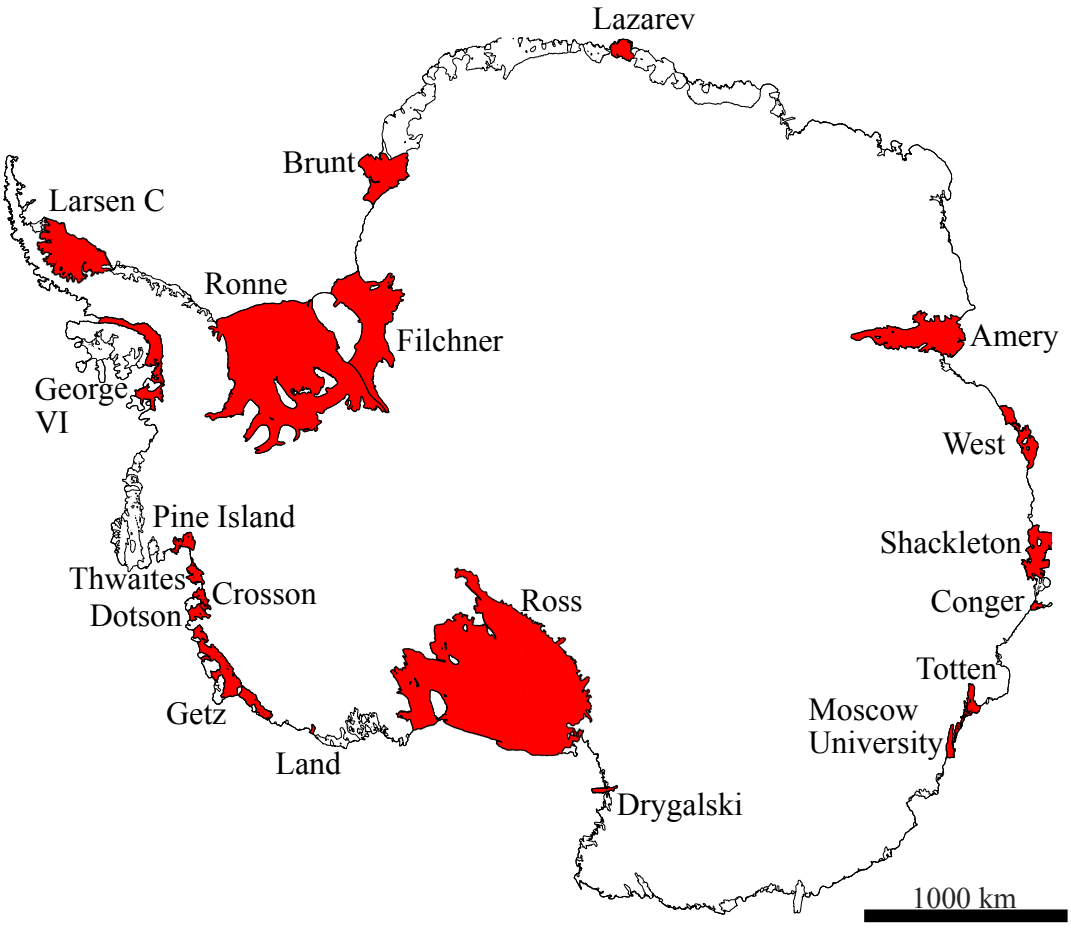


Figure 4.1: The locations of ice shelves from across Antarctica examined in this study.

well-documented stable calving cycles (Rydt and others, 2019), but are known to be rough with large structural heterogeneity.

#### 4.2.2 Data

To conduct our survey, we used ice shelf elevation data collected over a period of nearly two decades from four distinct sources. First, we used ICESat Global Elevation data between 2004 and 2009 (Zwally and Schutz, 2014). Second, we utilized Operation IceBridge (OIB) data between 2009 and 2019, specifically surface elevation data from the Multichannel Coherent Radar Depth Sounder (MCoRDS) sensor (Allen and others, 2010). Third, we used the Reference Elevation Model of Antarctica

| Data Name | Years | Reference |
|---|---|---|
| ICESat GLAS L1B Global Elevation Data | 2004-2009 | (Zwally and Schutz, 2014) |
| Operation IceBridge (OIB) MCoRDS L2 Ice Surface | 2009-2019 | (Allen and others, 2010) |
| Reference Elevation Model of Antarctica | 2016 | (Howat and others, 2022) |
| ICESat-2 L3B Slope-Corrected Land Ice Height | 2019-2021 | (Smith and others, 2022) |
| Ice Shelf Area | 2004-2021 | (Greene and others, 2022) |
| Ice Shelf Thickness Trend | 2008 | (Rignot and others, 2013) |

Table 4.1: List of data products used in this study as well as there time frame and supporting citations

(REMA) digital elevation model (DEM), which has a median date of 2016 for all elevation data (Howat and others, 2022). Finally, we included ICESAT-2 Ice Sheet Elevation data from between 2018 and 2021 (Smith and others, 2022).

In addition to the ice shelf elevation data, we also used a recent time series of ice shelf area obtained from Greene and others (2022). This data was used to compute changes in the area for each ice shelf over the time period of the elevation data. Trends in ice thickness were obtained from Rignot and others (2013) and were normalized relative to the average ice mass over the time frame of this study. Changes in percent ice thickness and percent ice area were then summed to create a percent change in the ice shelf volume metric. Changes in ice shelf volume do not take into account changes in grounding line positions and instead reflect changes in the area associated with calving. Table 2 provides a detailed overview of these data sources.

#### 4.2.3 Ice Shelf Roughness

Based on Whitehouse (2004) and Watkins and others (2021), we defined roughness along a given direction or track (measured in meters) as the square root of the integral of the power spectral density $S(k)$ (measured in $m^3$):

$$R = \sqrt{\int_{k_1}^{k_2} S(k)dk}. \tag{4.1}$$

Here, $k$ (measured in 1/m) represents the wavenumber. The lower and upper

bounds of integration in wavenumber are $k_1 = 10^{-4}$ (1/m) and $k_2 = 2 \times 10^{-3}$ (1/m), respectively. These bounds define the portion of the spectrum over which roughness is calculated, corresponding to wavelengths between approximately 500 m and 10 km. We chose the lower bound of this resolution to be around 500 m, based on the resolution of the crudest data in our survey. This ensures that roughness from all data sources can be compared. Finally, for each year of the data on each ice shelf, we take the median of all roughness values. This results in a year by year measurement of ice shelf roughness.

#### 4.2.4 Uncertainty Characterization

Because we are comparing roughness computed from instruments with different instrument characteristics, spatial coverages, and temporal coverages, we started by assessing the uncertainty in our roughness calculations using a bootstrap analysis. The details of this analysis are included in Appendix E, but we summarize it here. We categorized the source of uncertainty into (1) uncertainty related to spatial coverage (i.e., how many tracks cross the ice shelf in a given interval of time) and (2) uncertainty related to track orientation (tracks oriented along different directions will resolve different components of roughness). There are also sources of uncertainty from the data sources themselves, but they are small relative to uncertainty of coverage and orientation and therefore are not considered here.

We then defined the total uncertainty as the sum of the square root of the squares. To estimate the uncertainty associated with both track and spatial coverage we used the REMA surface elevation for each ice shelf as a reference. We then generated synthetic "tracks" with different spacing and orientations and calculated the roughness based on these synthetic tracks to estimate an error associated with the orientation and spacing of tracks. Generally, uncertainty increases for smaller and more sparsely

covered the ice shelves. Given the fact that roughness is changing, it is possible that our bootstrap analysis could underestimate roughness in regions where the roughness increased dramatically. However, for the ice shelves considered here, the uncertainty is dominated by the relatively sparse spacing of tracks for most ice shelves. Our uncertainties are likely high estimates of what the true uncertainty would be. Our uncertainties are also small enough for us to draw statistically significant conclusions from the data. We also tested to see if changes in roughness could be attributed to improved sensor quality and found little correlation between roughness and sensor for many ice shelves.

## 4.3 Results

### 4.3.1 Ice shelf roughness does not correlate with ice area, thickness, or volume

We first examined the relationship between the average surface roughness over the entire time record for the 20 ice shelves as a function of percent change in ice shelf area, ice shelf thickness, and ice shelf volume (Figure 4.2). We defined the percent change in shelf volume as the sum of the percent change in ice shelf area (derived from a slope of a linear fit over the data record of ice shelf area from Greene and others (2022)) and the percent change in ice shelf thickness per year (obtained directly from Rignot and others (2013)). We normalized the change in ice shelf volume as a percentage relative to the first year of the data record due to the large range of ice shelf sizes in this study. In contrast, roughness was not normalized, as median roughness is independent of ice shelf size (Watkins and others, 2021).

From Figure 4.2, we find no clear trend between the median roughness and either the area change (Figure 4.2a), thickness change (Figure 4.2b), or volume change (Figure 4.2c) of ice shelves. The roughest ice shelves in this survey are Totten, Thwaites, and Drygalski which have varying degrees of area, thickness, and volume

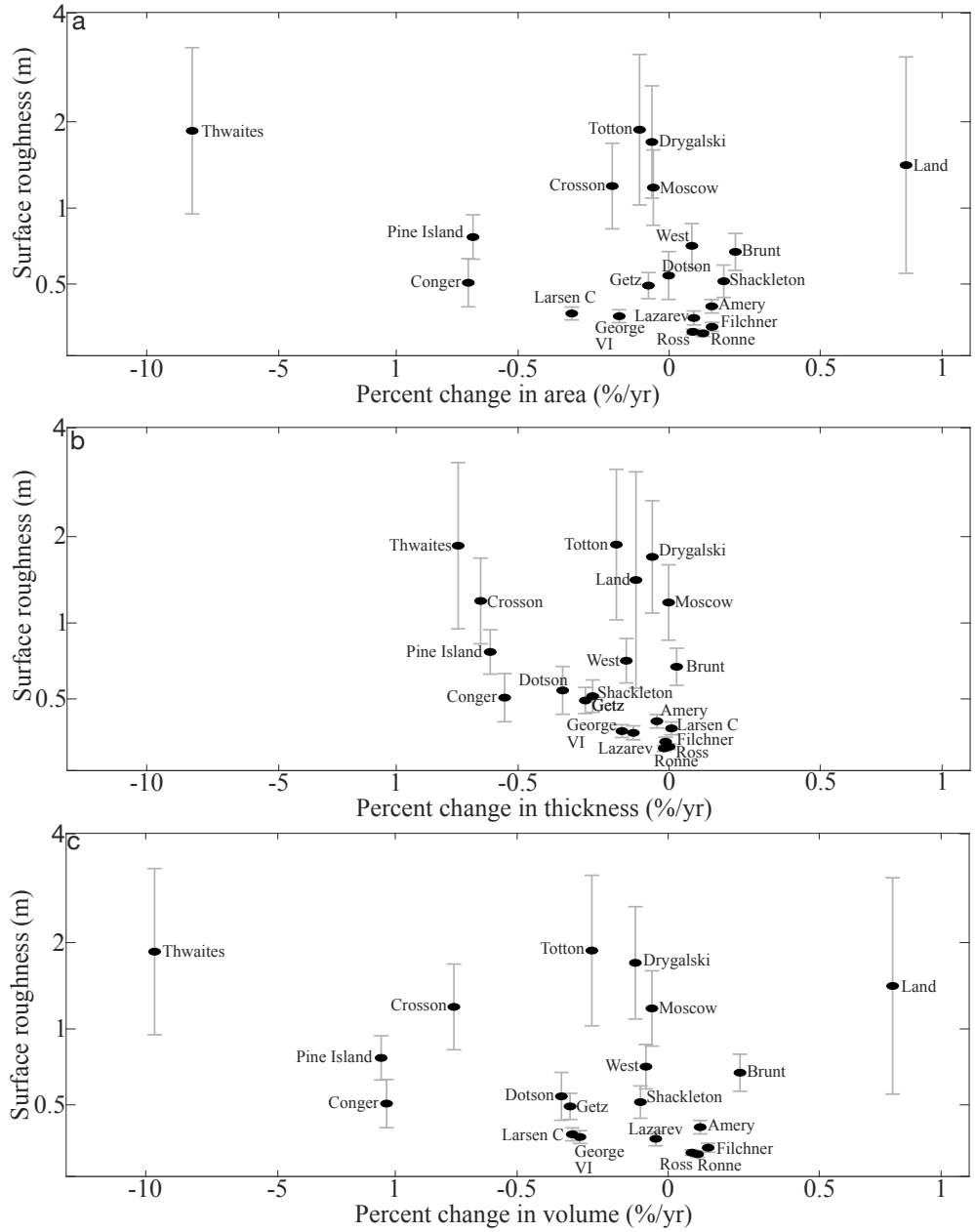


Figure 4.2: Mean roughness vs a) change in ice shelf area, b) change in ice shelf thickness, and c) change in ice shelf volume for 20 ice shelves across Antarctica. Error bars represent errors from data orientation as well as data coverage, as described in Appendix C.

change associated with them. In contrast, the smoothest ice shelves are the Filchner-Ronne, Ross and Amery ice shelves, all of which have not changed significantly in their area, thickness, and volume.

#### 4.3.2 Change in ice shelf roughness is correlated with change in ice shelf area, thickness, and volume

For a large suite of ice shelves, we found that roughness did not correlate to area, thickness, or volume change. Next, we examined the relationship between the change in roughness and the percent change in ice shelf area, thickness, and volume. We estimate the change in roughness from the slope of a linear fit to the time series of roughness for each ice shelf over 20 year period of our observations. The results of this comparison are shown in Figure 4.3.

From Figure 4.3, we see that a trend exists between increased change in ice shelf roughness and increased percent change in ice shelf area, thickness, and volume. Thwaites experienced the greatest change in roughness, roughening by $\approx 0.04$ m/year. Contrary to Thwaites, the Land ice shelf experienced a decrease of roughness over the 20-year period of $\approx 0.02$ m/year as well as a significant increase in area and volume. However, errors associated with the Land ice shelf are large due to limited data coverage, so this decrease in roughness may be an artifact of the sparse data coverage and therefor isn't statistically significant. We find that the percent change in area (Figure 3a), percent change in thickness (Figure 4.3b), and percent change in volume (Figure 4.3c) all correlate well with the change in roughness. To quantify, we performed a least squares linear regression and found $R^2$ values of $0.7756 \pm 0.0887$ (Area), $0.6328 \pm 0.1068$ (Thickness), $0.8590 \pm 0.0673$ (Volume). For each, the error on the $R^2$ values is the result of a bootstrap, which calculated the fit of each line using only half the data. For the error, we report the standard deviation of these fits,

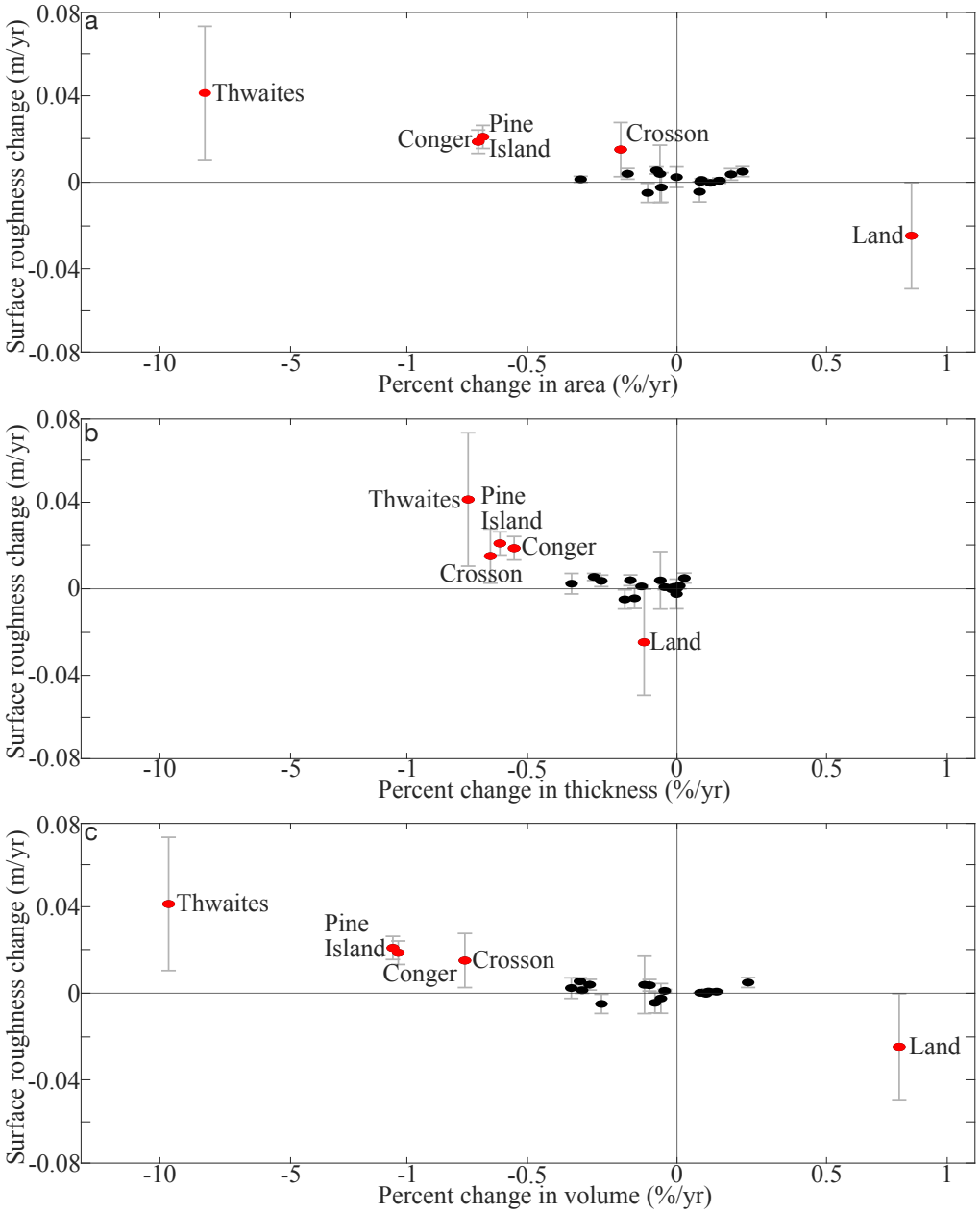


Figure 4.3: Change in roughness vs a) change in ice shelf area, b) change in ice shelf thickness, and c) change in ice shelf volume for 20 ice shelves across Antarctica. Error bars represent the root mean square error for each time series of ice shelf roughness. Only ice shelves with a roughness greater than the standard deviation are shown in red and labeled

which shows that even when high-roughness ice shelves are removed from the fit, the trends still remain. In addition, these results show that all three metrics of change correlate with the change in roughness and that, intriguingly, the volume change has the strongest correlation

#### 4.3.3 Most ice shelves are not changing significantly

The results from Figure 4.3c, in addition to showing a trend in the change in roughness to the change in ice shelf volume, also show that the majority of ice shelves are clustered around the origin of the plot. This indicates that the majority of ice shelves are exhibiting little or modest changes. Figure 4 shows the time series of roughness for Drygalski ice tongue, Totten ice shelf, Brunt ice shelf, Larsen C ice shelf, and Amery ice shelf.

From Figure 3.4 we see that over the approximately 20 year data record, these ice shelves vary in their magnitudes of roughness, but the roughness remains relatively constant over time (within our estimated error bars). Some ice shelves have a larger magnitude of roughness (Drygalski and Totten, roughness ∼1-2 m), with magnitudes comparable to those of the ice shelves in the Amundsen Sea Embayment. In contrast, some ice shelves are much smoother (Brunt, Larsen C, and Amery, roughness ∼0.3-0.7 m). For all cases in Figure 4.4 however, there are no statistically significant trends in the roughness over time, despite the fact that these ice shelves experienced significant calving events during the observation period (Hogg and Gudmundsson, 2017; Walker and others, 2021; Francis and others, 2022). In addition, the roughness from the ICESat-2 era is no higher in most cases (except Brunt) than the ICESat era, illustrating that increases in roughness of other ice shelves is unlikely related to improved sensor quality or track spacing.

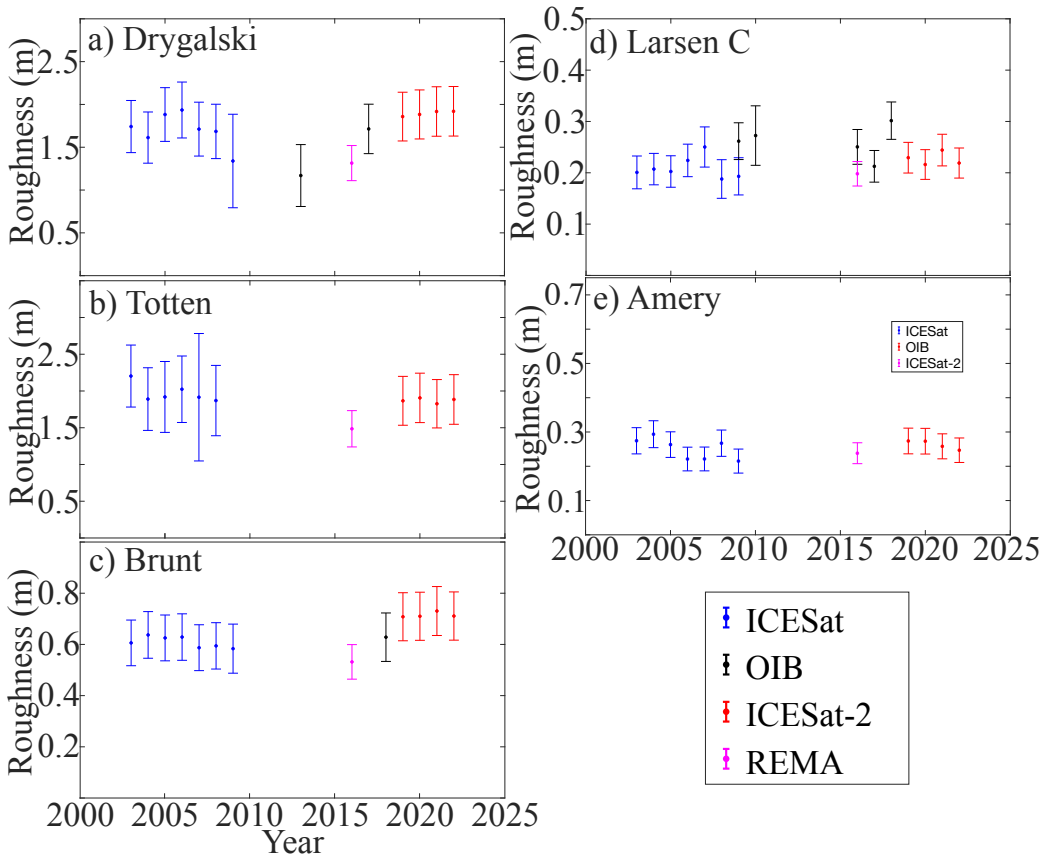


Figure 4.4: Roughness over time for the a)Drygaski, b)Totten, c) Brunt, d) Larsen C and e)Amery ice shelves. Note that the y-axis is different for each of these plots. Error bars represent errors from data orientation as well as data coverage, as described in Appendix C.

### 4.3.4 Ice Shelves in the Amundsen Sea are roughening the most

Most ice shelves in this survey did not change significantly in roughness nor change in area, thickness, or volume. However, the Amundsen Sea ice shelves have experienced the largest increase in roughness relative to 2004. This is particularly evident in changes to Thwaites and Pine Island but is also visible in the Crosson ice shelf (Figure 4.3). By contrast, of the remaining Amundsen Sea ice shelves, Getz and Dotson both show much smaller changes to their roughness that are not statistically significant. To see if roughness changed stepwise or continuously through the time period, we plotted roughness vs time for each of the Amundsen ice shelves (Figure 4.5). These ice shelves are all proximal to each other and have likely experienced similar large-scale climate forcing.

From Figure 4.5 we see that Pine Island, Thwaites, and Crosson ice shelves each experienced the largest increase in roughness over the time period of the survey. These ice shelves also all mostly changed step-wise throughout the data record, rather than continuous yearly increases. Of these three ice shelves, Thwaites both started out as the roughest, as well as exhibiting the largest increase in roughness over time. Interestingly, the changes in ice shelf roughness for Thwaites and Crossen show periods of low roughness in the early 2010s, followed by current high roughness states. In addition, Pine Island and Crosson ice shelves started out at different levels of roughness (with Crosson starting higher), but increased by similar magnitudes of roughness over the survey period. Of the other two Amundsen Sea ice shelves in this survey, Getz and Dotson both still increased in roughness, however, this increase was smaller than Pine Island, Thwaites, and Crosson. In addition, both Dotson and Getz both started out considerably smoother than their other ASE counterparts.

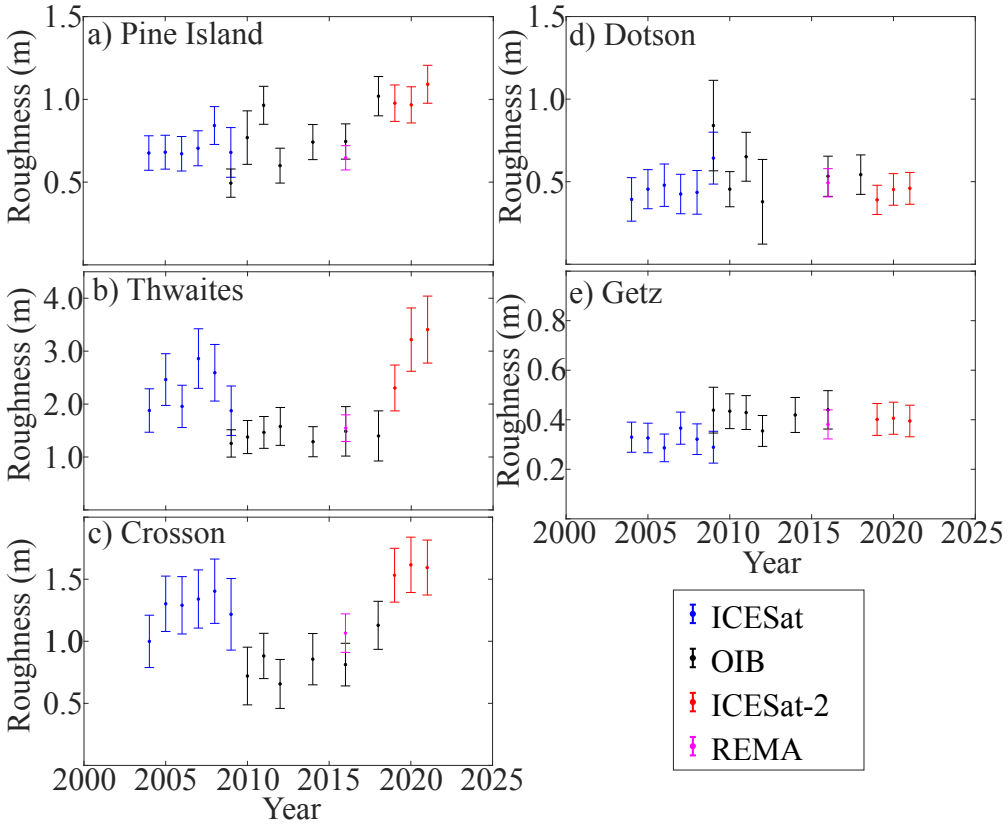


Figure 4.5: Roughness over time for ice shelves within the Amundsen Sea Embayment: a) Pine Island, b) Thwaites, c) Crosson, d) Dotson and e) Getz ice shelves. Note that the y-axis is different for each of these plots

## 4.4 Discussion

### 4.4.1 Many high roughness ice shelves are stable

Our results show that the roughness of ice shelves varies over an order of magnitude, which is consistent with previous work (Watkins and others, 2021). However, we also show that some high-roughness ice shelves are not necessarily changing in terms of their extent (area, thickness, and volume). Two examples of this are the Dygalski ice tongue and the Totten ice shelf, both of which have large median roughnesses that are comparable to those of Pine Island and Thwaites glaciers (Figure 4.2). Both Drygalski and Totten are visually rough in the satellite imagery, and studies have shown numerous basal melt channels as well as crevasses/rifts (Dow and others, 2018; Indrigo and others, 2020). Drygalski has been shown to be generally unchanged in area over at least the last 50 years (Wuite and others, 2009; Hesari and others, 2022), while Totten ice shelf has shown small amounts of thinning and grounding line retreat (Li and others, 2015). Currently, the grounding line position at Totten ice shelf is stable, but small changes to ocean temperatures could force future retreat and area loss (McCormack and others, 2021). Monitoring future changes in the roughness of Totten, and potentially other ice shelves that are fringing the line between stable and unstable, may be insightful to determine if the ice shelf may be vulnerable.

### 4.4.2 Mechanisms for roughening in the Amundsen Sea

Amundsen Sea ice shelves, specifically Thwaites, Pine Island, and Crosson, all roughened over the data record of this study. In contrast to many parts of Antarctica, surface temperatures in the Amundsen Sea remain cold (Dixon, 2007; Trusel and others, 2013; Werner and others, 2018). In gauging then the specific mechanisms that

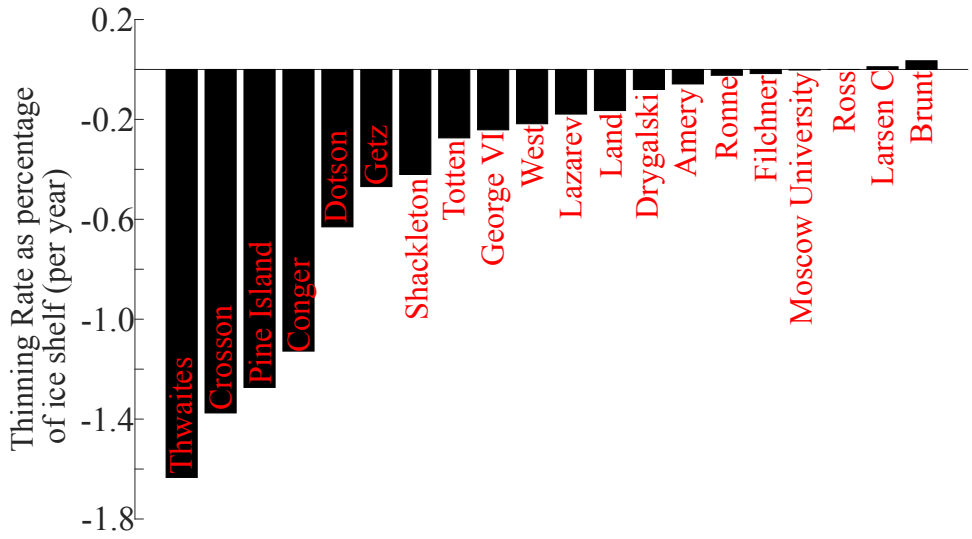


Figure 4.6: A bar graph using data from Rignot and others (2013) showing the ice shelf thinning rates as a percentage of mean ice shelf mass for all ice shelves in this survey

may drive the roughening (and increased volume loss) of ice shelves in the region. A previous study has shown that basal melt rates correlate with the magnitudes of ice shelf roughness (Watkins and others, 2021). However, as there is no data set on how basal melting for ice shelves evolves over time, we cannot compare changes in melt rates to changes in ice shelf roughness. Instead, we can examine the normalized thickness trend over the survey period to see which ice shelves are thinning the most (Figure 4.6). From Figure 6, we can clearly see that of all the ice shelves in this survey, Thwaites, Pine Island, and Crosson have the largest thinning rates. This indicates that the roughening of ice shelves in the Amundsen Sea is likely driven by ocean forcing, which is consistent with other studies suggesting ocean forcing is causing a change in the region (Jenkins and others, 2018; Nakayama and others, 2019).

Also notable is the fact that both the Thwaites and Crosson ice shelves experienced periods of high roughness up until approximately 2010 followed immediately by a steady period of low roughness until approximately 2017 (Figure 4.5b and c). This

was then immediately followed by a period of high roughness which continues into the present day. Interestingly, on Thwaites periods of high roughness overlap with periods of documented structural weakening (2006-2012: 2016-2018), and periods of low roughness overlap with periods of re-advance (2012-2015)(Miles and others, 2020). This indicates that as the ice shelf was weakening, it likely roughened as more fracture occurred and as it re-advanced, it smoothed as some of this fracture was healed. This hints that increases to the roughness may have been indicative of the ice shelf vulnerability.

#### 4.4.3 Using changes in roughness to predict ice shelf vulnerability and collapse

As changes in ice shelf roughness correlate with changes in ice shelf thickness, area, and volume, we speculate that high changes in ice shelf roughness may be indicative of ice shelves that are primed for collapse. This is further highlighted by the Conger ice shelf, notable for it's collapse in March of 2022, which saw the third highest change in roughness in this survey. As this ice shelf was an outlier in terms of its high change in roughness relative to its location on the continent, we examined it's roughness change in more detail (Figure 4.7). Specifically, we plotted the roughness of the Conger ice shelf since 2004 and examined if there were changes both in the short term (within the last 2-3 years) as well as the long term (over the last 20 years) for the roughness.

From Figure 4.7, we see that there was a considerable jump in roughness from 2004 to just before the collapse event. This increase is statistically significant and cannot be attributed to just fluctuations in the data or changes in sensors. This suggests that the roughness increase before Conger's demise hints that the increased roughness foreshadowed the ice shelves demise and that longer-term changes appear to have manifested as a visible increase in roughness. Studies also suggest that

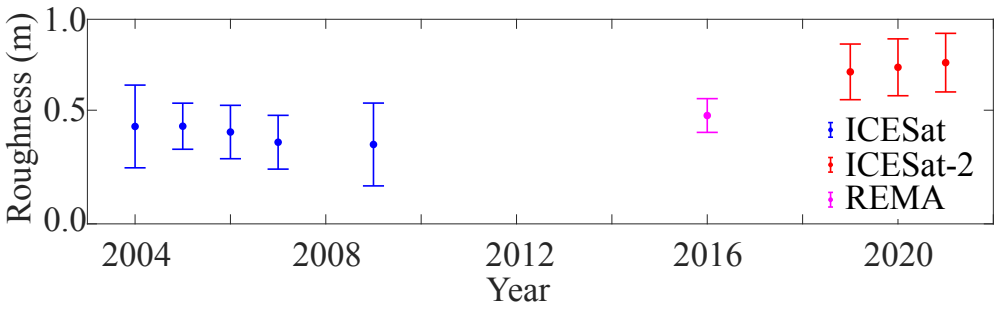


Figure 4.7: Roughness of the Conger ice shelf between 2004 and 2021. The ice shelf collapsed in March of 2022.

the Conger ice shelf experienced increased basal melt(Bernales and others, 2017) as well as increased crevassing and rifting (Rignot and others, 2022) in the lead-up to its collapse. Decreases in thickness and area are similar to what the fast-changing Amundsen Sea ice shelves are also experiencing (Figure 4.3). In contrast to the Amundsen Sea shelves, the Conger ice shelf experienced extreme temperature events as a result of an atmospheric river which likely pushed it to a breaking point Horton (2022). Although temperatures in the Amundsen Sea currently remain coldDixon (2007); Trusel and others (2013); Werner and others (2018), trends in temperature are drifting upwards, which may push the already fragile ice shelves in the region past stable thresholds. As such, the complex processes that are indicative of collapse would likely be reflected in increasing roughness, hinting that roughness may be a metric for gauging future ice shelf stability.

## 4.5 Conclusions

Here, we investigated changes in ice shelf roughness over the past two decades and its correlation with ice shelf area, thickness, and volume changes. Our findings demonstrate a strong connection between roughening ice shelves, which are characterized by increased melt channels, crevasses, and rifts, and ice shelves that are losing

the most volume. Our results reinforce previous research showing that ice shelves in the Amundsen Sea, specifically Pine Island and Thwaites, have undergone the most significant changes in the region and across the continent. However, the majority of ice shelves in our survey have not experienced significant roughening or volume loss. We propose that, while these ice shelves appear to be stable currently, continued climate forcing may cause future instability. Monitoring roughness changes may offer a valuable tool to track if an ice shelf transitions from a stable to an unstable state. This speculation is supported by our examination of the roughness of the Conger Ice Shelf leading up to its collapse in March 2022 which found that it experienced significant increases in roughness over the past two decades. We suggest that this increase in roughness likely primed the ice shelf for collapse, which was triggered by abnormally warm atmospheric temperatures. In addition, our analysis of ice shelves in the Amundson Sea also shows that roughness increased ahead of fragmentation and retreat events. While further verification of our results is required due to data limitations, our findings suggest that changes in ice shelf roughness may serve as an easily measurable indicator of ice shelf stability.

# CHAPTER V

# Conclusion

Our work focuses on the spatial variations in easily measurable parameters (such as the thickness) of ice shelves can tell us. Specifically, we define these spatial variations as roughness and investigate how the presence of features, such as melt channels and crevasses, contribute to that roughness. This is done in an attempt to more thoroughly understated how ice shelves behave and how these features may affect their stability.

In Chapter II we defined our method for quantifying roughness. We did this by using the continuous wavelet transform and windowing along track segments of ice thickness data collected over a 10-year period. We first analyzed Pine Island and Ross ice shelves and found that on both shelves, roughness was elevated surrounding melt channels, crevasses, rifts, and pinning points. However, the Ross ice shelf was the opposite of Pine Island ice shelf and was considerably rougher. This was true across all wavelengths of roughness. In addition, roughness was found to be fractal (scaling with wavelength), which seemed to indicate that crevasses and melt channels exited on a continuous spectrum of features. Finally, we expanded our analysis to five other ice shelves. We found that ice shelves in the Amundsen Sea were roughest, and that roughness in general correlated with basal melt rates. This hinted that may

be more tightly controlled by ocean forcing than previously thought.

Using the principles of ice shelf roughness defined in Chapter II, we expanded upon our analysis in Chapter III by investing how melt and fracture impart melt channels and crevasses onto ice shelves and how these features affect ice shelf roughness. We did this by using gridded ice shelf base data to investigate how basal melting and ice deformation contribute to crevasse and melt channel formation and evolution on the Pine Island Ice Shelf in the Amundsen Sea. We found that high basal melt rates and high first principal strain rates lead to substantial roughening of the ice shelf through a collection of features, including melt channels and crevasses. Critically, melt channels and crevasses are the deepest at locations where melt rates *and* strain rates are highest. This hints that the combination of melt rates and strain rates work in tandem to excavate and seed the deepest melt channels and crevasses on ice shelves. These features then may form lines of weakness that transform into rifts and, ultimately, the detachment boundary for calving events. This again suggests that the ocean may play an important role in controlling the future stability of ice shelves.

Using the knowledge from Chapter II and Chapter III that ice shelf roughness is linked to melting and fracturing of ice shelves, we investigated if changes in roughness reveal increasing ice shelf vulnerability. We anticipated that the addition of melt channels, crevasses, and rifts could potentially lead to increased ice fracture and ice shelf vulnerability. However, this relationship between melting, fracturing, and ice shelf failure is complex. We hypothesized here that the evolution of the ice shelf surfaces may hint at which ice shelves are most vulnerable and at-risk ice for collapse and retreat. To examine this hypothesis, we analyzed 20 years of ice surface observations. In contrast to Chapter II, for a much larger suite of ice shelves, we saw

very little correlation with melt rate. However, using the knowledge from Chapter III that high strain rates are also elated to ice shelf roughness as well as changing our assumptions of ice shelf roughness over time, we found that increasing roughness of ice shelves correlated with ice shelves that are losing volume. This is especially true in the Amundsen Sea, where Pine Island and Thwaites Glacier tongues have experienced large-scale increases in roughness and ice loss since 2000. In addition, the Conger Ice Shelf, which collapsed in 2022, also showed an increase in roughness in the years leading up to its collapse. These findings suggest that roughness could be a valuable tool in identifying those ice shelves most vulnerable to collapse and retreat.

Based upon the results of Chapter IV, future work involving the roughness of ice shelves would be well suited toward high-resolution monitoring of gridded ice shelf thickness over time. This could potentially be done using Digital Elevation Models derived from Synthetic Aperture Radar Images of ice shelves from across the continent. By using the gridded product, uncertainties related to track coverage and orientation could be mitigated, which could produce a more robust result. In addition, the incorporation of ice shelf roughness into models could prove to be valuable in predictions of ice shelf stability. Based on the results of Chapter III, this could potentially be accomplished by using model knowledge of strain rates and melt rates to infer what the ice roughness should actually be. The challenging part here would be taking the step from roughness back to actual thickness, but could potentially be accomplished by an inverse continuous wavelet transform. At any rate, using roughness to monitor ice shelf "health", as suggested by Larter (2022), seems like it could be a potentially valuable tool going forward.

# APPENDICES

# APPENDIX A

# Supplementary Information for Chapter 2

This appendix, which constitutes the supporting information for Chapter 2, appears in its entirety in the following:

Watkins RH, Bassis JN and Thouless MD (2021) Roughness of ice shelves is correlated with basal melt rates. *Geophysical Research Letters*, **48**(21) (doi: 10.1029/2021gl094743):

## Introduction

This supporting information document contains four supporting figures and one supporting table. The first figure (Figure A.1) shows the distribution of roughness over pinning points and shear margins for Pine Island and Ross. The second figure (Figure A.2) shows the spectra of tracks going in the along flow and transverse to flow directions for the Pine Island ice shelf. The third figure (Figure A.3) shows the spectra for the remaining ice shelves in our survey. The last figure (Figure A.4) shows melt rate vs roughness for Pine Island, taken on a point by point basis across the ice shelf. Finally, Table A.1 includes direct links to the data sets that were used in our manuscript.

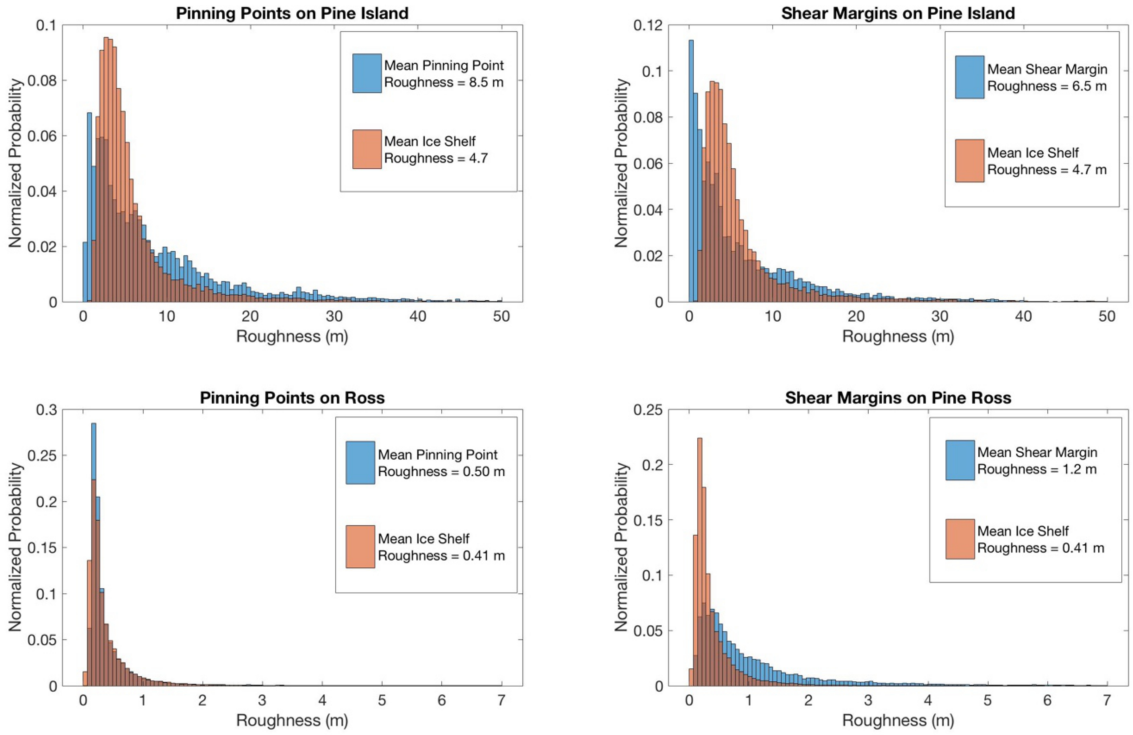


Figure A.1: Distributions of roughness around pinning points and shear margins for both Pine Island and Ross compared to the distribution of roughness across each total ice shelf. For both features of both ice shelves, roughness is always higher relative to the mean roughness, indicating that pinning points and shear margins make ice shelves rougher. The analysis for pinning points is taken for all documented pinning points on each ice shelf, rather than just the example pinning point shown in text.

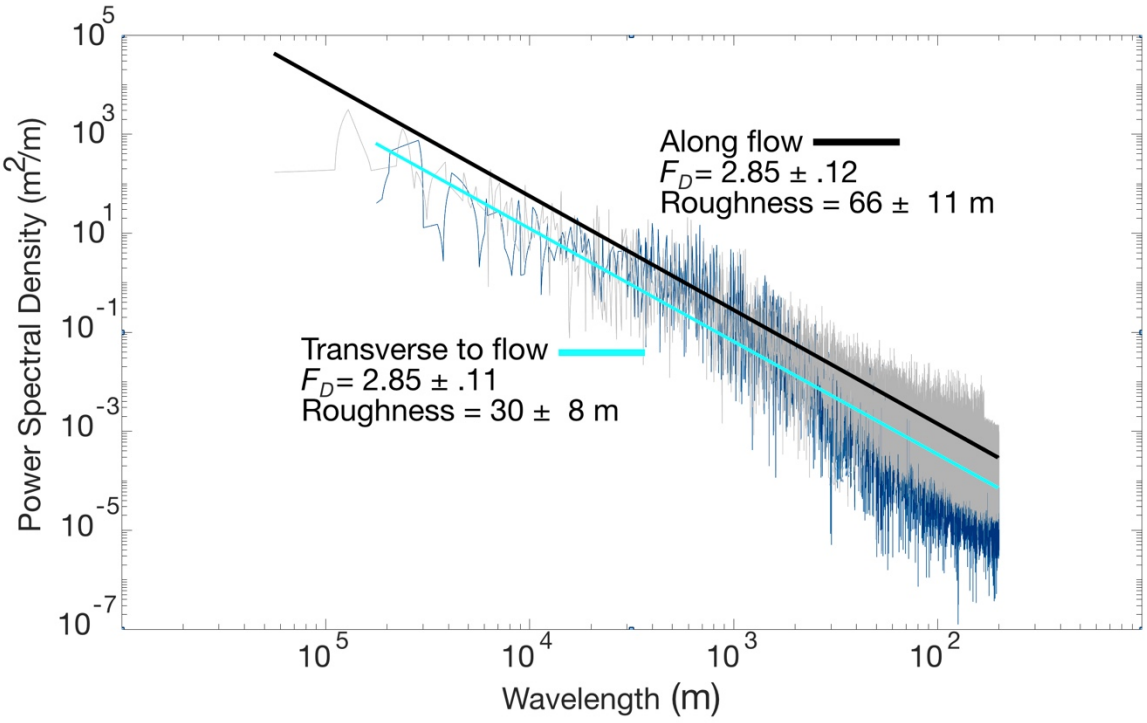


Figure A.2: The spectra of tracks going roughly in the along flow (grey spectra) and transverse to flow (blue spectra) directions for Pine Island. When taken individually, both spectra still obey a power law with a statistically similar slope to that of the ice shelf as a whole.

| Data Name | Data Source | Reference | Link to data | Data Time frame |
|---|---|---|---|---|
| MCoRDS L2 Ice Thickness | Operation IceBridge | Paden and others (2010) | https://nsidc.org/ice-bridge/portal/map | 2009-2016 |
| Pine Island Ice Shelf | Geophysics Data Portal | Vaughan and others (2012) | https://legacy.bas.ac.uk/data/aerogeo/dataset/pig/ | 2011 |
| Total Ice Thickness | ROSSETTA-Ice | Das and others (2020) | http://wonder.ldeo.columbia.edu/data/ROSETTAIce/DerivedProducts/DICEIceThickness/ | 2019 |
| Average Basal Melt | Multiple Sources | Liu and others (2015) | https://www.ncbi.nlm.nih.gov/pmc/article/PMC4371949/bin/pnas.1415137112.sd01.xls | 2005-2011 |

Table A.1: Table 2.1 with expanded links to data products. Note that many of the data products require user registration in order to access.

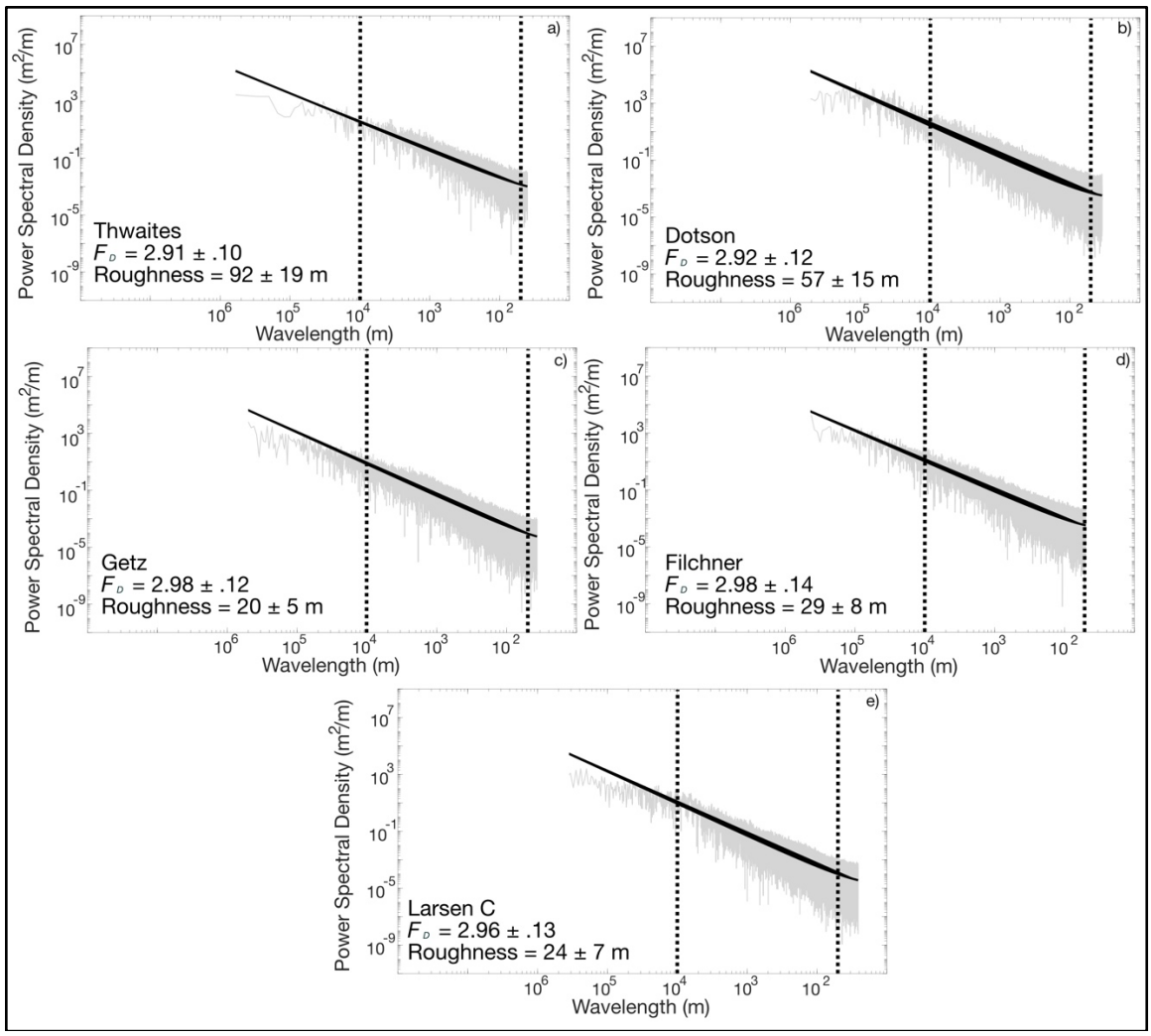


Figure A.3: . The power spectral density of all tracks going over the a) Thwaites, b) Dotson, c) Getz, d) Filchner, and e) Larsen C ice shelves. Also shown is a least squares fit of the power-law equation to each spectrum. Integration bounds used for calculating the average roughness for each ice shelf are plotted by the black dotted lines.

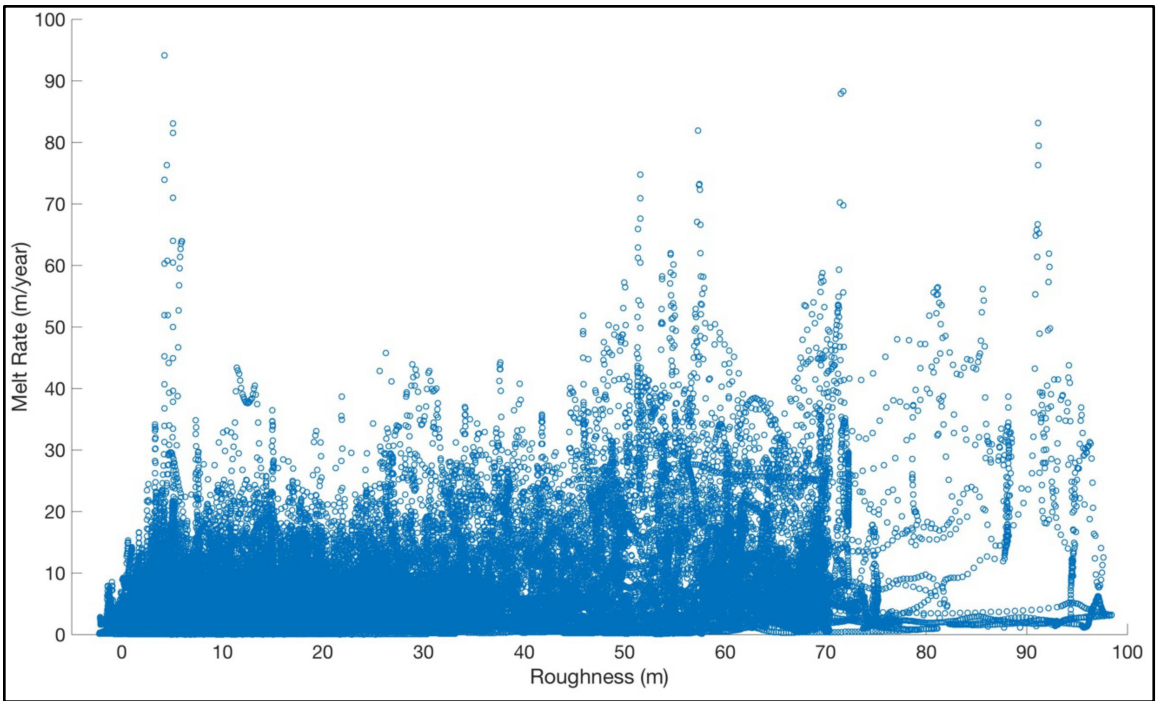


Figure A.4: Melt rate vs roughness for the Pine Island Ice Shelf. Melt rates are obtained Adusumilli and others (2020). Little correlation exists between roughness and basal melt when plotted on a point by point basis across the ice shelf.

# APPENDIX B

## Supplementary Information for Chapter 3

This appendix constitutes the supporting information for Chapter 3:

### Introduction

The supporting information in this document contains two supplementary figures. The first figure (Figure B.1) shows the 2D gridded roughness (calculated from BedMedmachine) across all of the Pine Island Ice Shelf. The second figure (Figure B.2) shows the distribution of roughness values across all of the Pine Island Ice Shelf as well as across all Antarctic ice shelves.

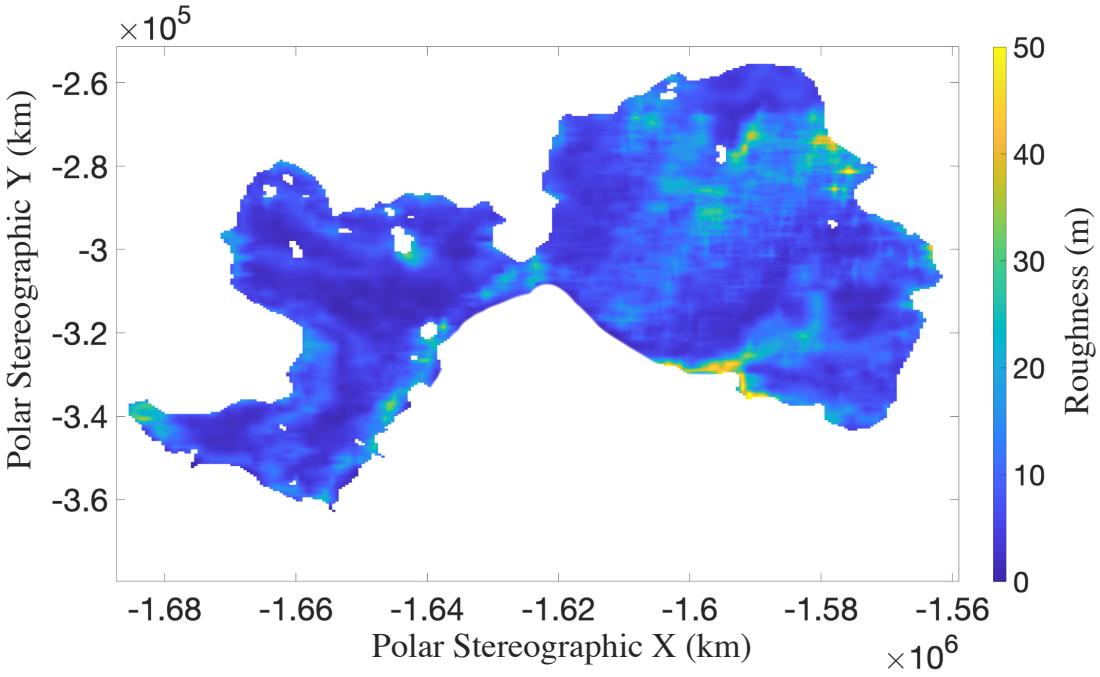


Figure B.1: A 2D map of roughness across the Pine Island Ice Shelf

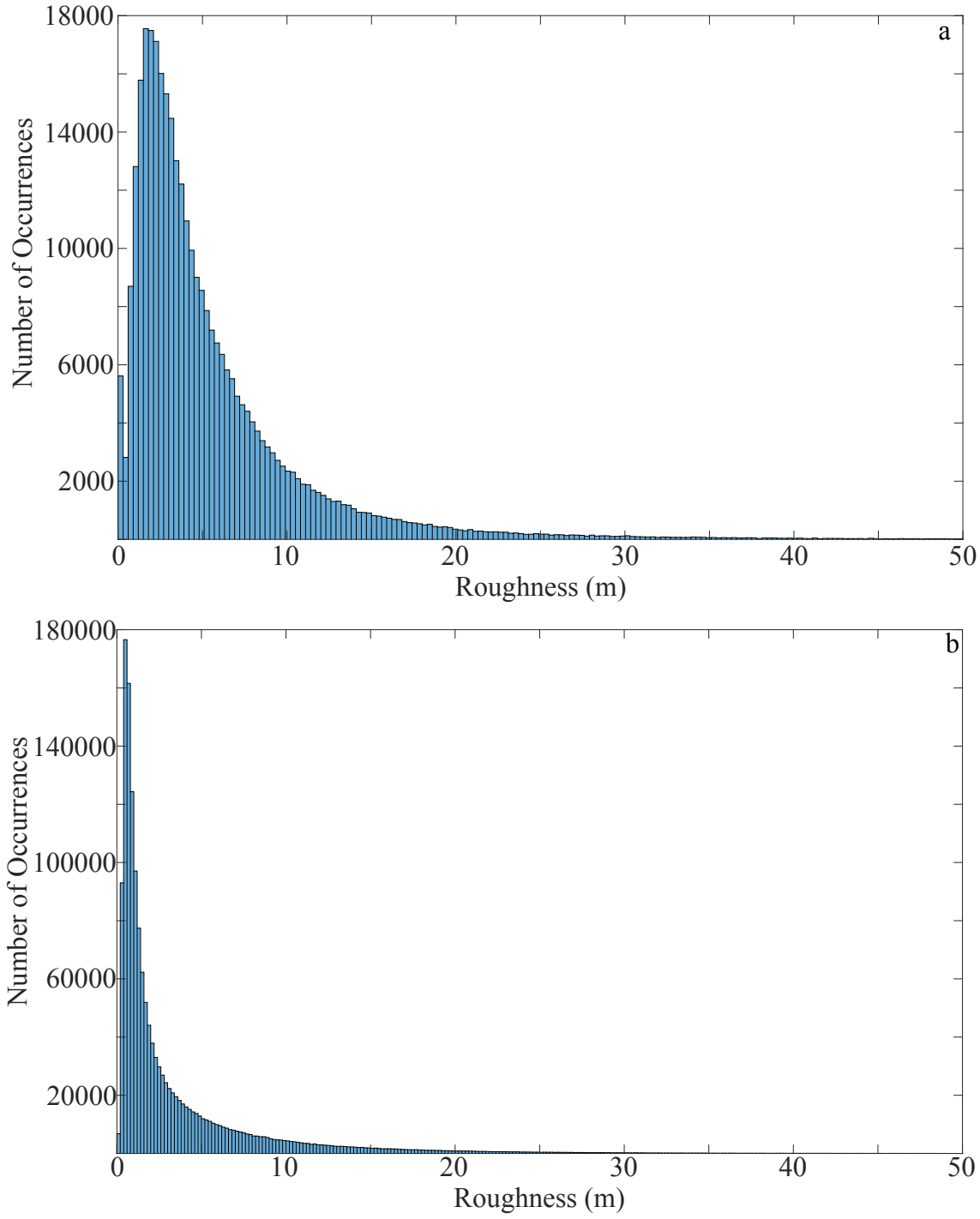


Figure B.2: a) Distribution of roughness values across the Pine Island Ice Shelf b) Distribution of roughness values across all Antarctic ice shelves

# APPENDIX C

# Supplementary Information for Chapter 4

This appendix constitutes the supporting information for Chapter 3:

## Detailed Roughness Uncertainty Characterization

When comparing roughness measurements obtained from various data sources with different sampling methods, it is essential to consider uncertainty. To achieve this, we conducted Uncertainty characterization for each ice shelf and year under study. In this section, we discuss the two primary sources of uncertainty associated with roughness measurement and their quantification. Furthermore, we show our definition of the total uncertainty, which we use consistently throughout this study.

### Uncertainty from Data Coverage

We first examined the uncertainty arising from data coverage, given that each of the four data sources we used exhibits considerable variability in terms of the extent to which a particular ice shelf is surveyed annually. It is therefore crucial to include this factor in our analysis of uncertainty. Figure C.1 illustrates this issue with the roughness measurements obtained from the Pine Island Ice Shelf by our four data sources over four specific years. It is evident from the visual representation that the extent of data coverage over the ice shelf fluctuates significantly from one year to another.

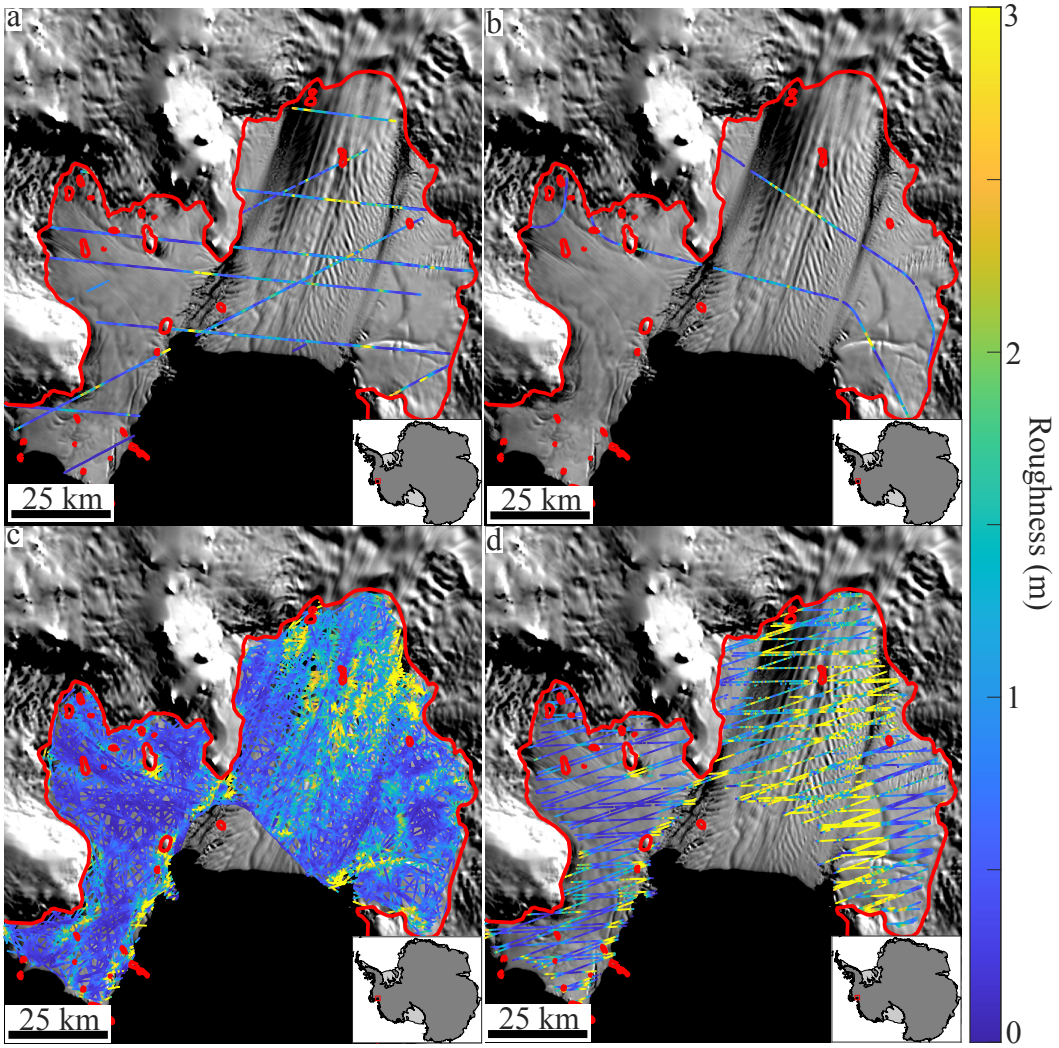


Figure C.1: Roughness measurement distribution across the Pine Island Ice Shelf for four different data sources over four different years. a) ICESat, 2005 b) OIB, 2012 c)REMA, 2016 and d) ICESat-2, 2021. The red line once again shows the proximate location of the grounding line.

To quantify this uncertainty, we utilize the REMA dataset, which is a gridded dataset with minimal data coverage gaps. By prescribing increasing numbers of random oriented "tracks" over an ice shelf, we can calculate the median roughness. As we obtain more randomly oriented "tracks" over the ice shelf, we sample more and more of the ice shelf's surface. We can represent the median roughness of an ice shelf as a function of the amount of surface area surveyed by plotting it. Figure C.2a illustrates this concept using data from the Pine Island Ice Shelf. The graph shows that the variability in the median roughness decreases as more of the ice shelf is surveyed. This is further demonstrated in Figure C.2b, which plots the standard deviation of the median roughness as a function of ice shelf data coverage. The graph shows that as the amount of the ice shelf surveyed increases, the uncertainty in roughness due to data coverage decreases, following an exponential decay. Therefore, we can use this method for each ice shelf in any given year to address the uncertainty in data coverage.

**Uncertainty from track orientation**

The second source of uncertainty in roughness that we examined was the uncertainty resulting from track orientation. As roughness is defined as an along-track variable in this assessment, the roughness measurement would be affected by the angle at which the track was sampled on the ice shelf surface. For instance, if a satellite sampled ice elevation data in parallel with a melt channel, the roughness measurement would likely be significantly lower than if the satellite sampled the elevation perpendicular to a channel. To evaluate the uncertainty in orientation, we again utilized the REMA dataset and randomly oriented tracks. We analyzed all the data points where two tracks intersected and computed the median roughness and standard deviation at each intersection point. The resulting plot shows that the

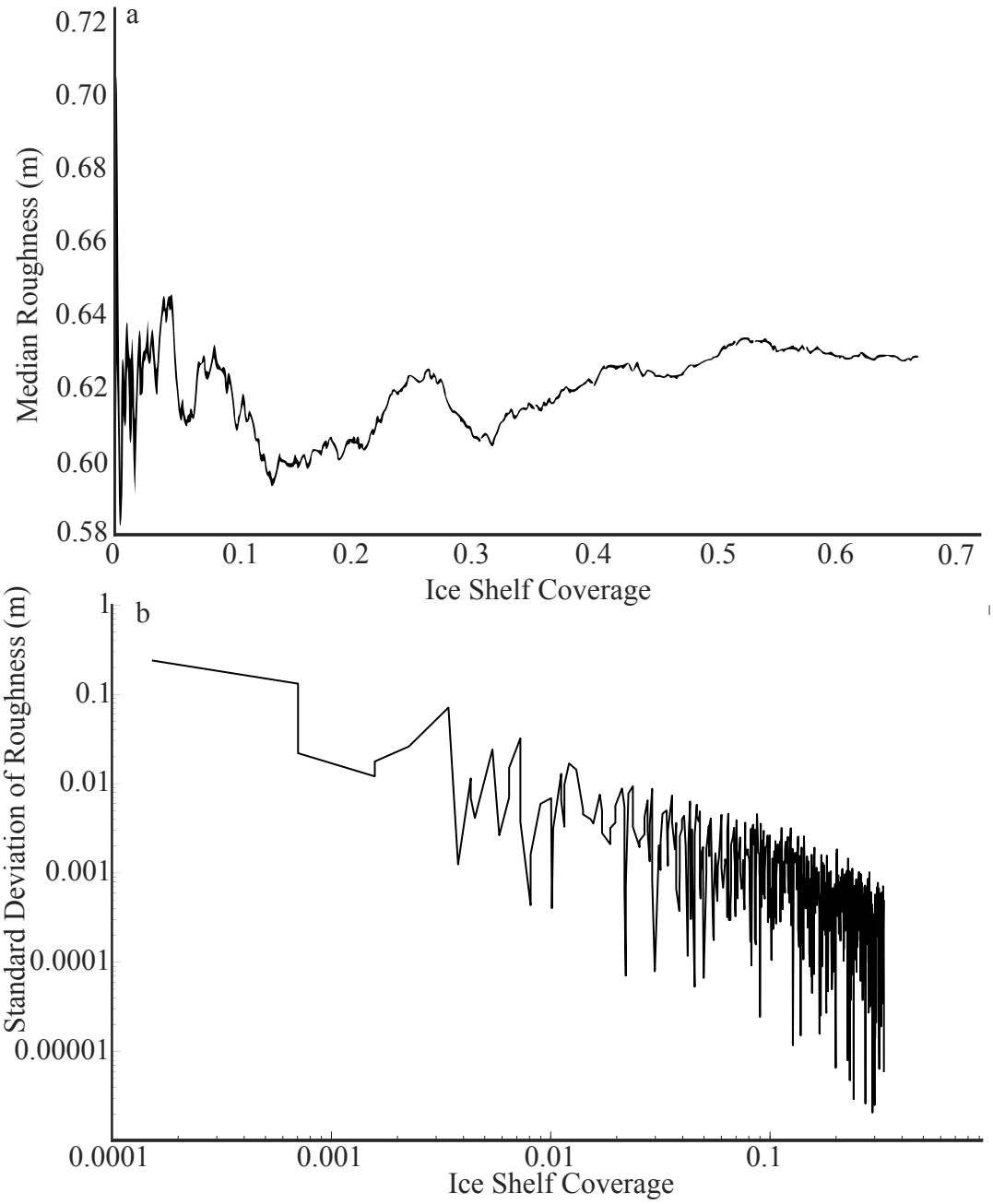


Figure C.2: a) Median roughness of Pine Island from REMA as a function of ice shelf coverage. b)Standard deviation of the median roughness as a function of ice shelf coverage. As more of the ice shelf is sampled, the standered deviation in the roughness decreases exponentially

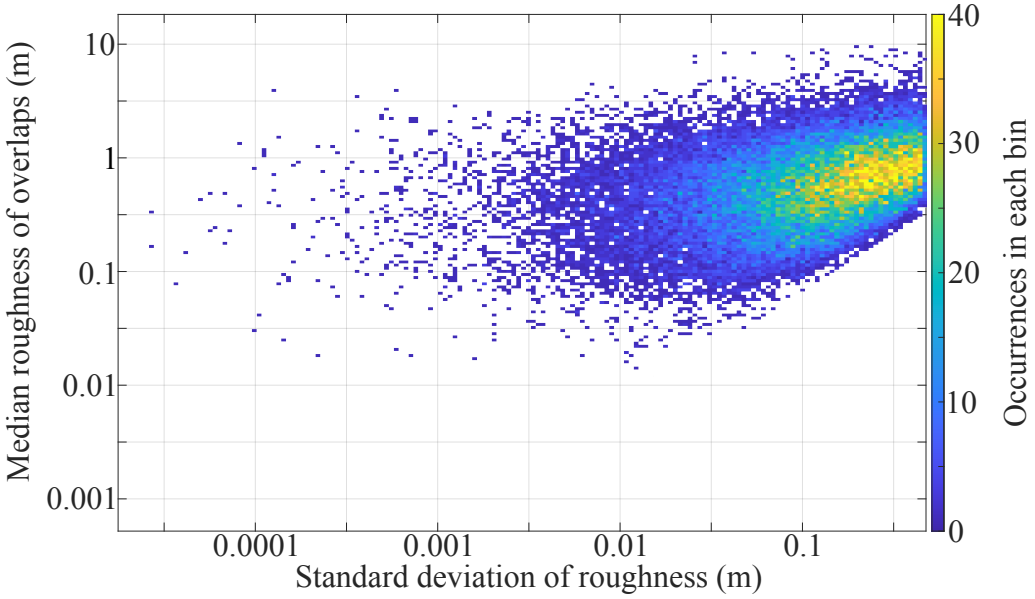


Figure C.3: The standard deviation of each roughness overlap vs the median roughness of that overlap point on the Pine Island Ice Shelf. Note that the higher the roughness, the higher the standard deviation (from track orientation)in the roughness will be.

higher the median roughness, the greater the uncertainty arising from track orientation, as demonstrated in Figure C.3. Using this technique, we can quantify this aspect of uncertainty for each ice shelf and each year under study.

**Total uncertainty in roughness**

After identifying the primary factors that contribute to the uncertainty in our roughness measurement, we aim to combine them into a single measure of uncertainty. To accomplish this, we take the sum of the root of the two standard deviations previously defined and combine them into the total uncertainty, represented by $\sigma$:

$$\sigma = \sqrt{(\sigma^2_{Coverage} + \sigma^2_{Orientation})}, \tag{C.1}$$

Here, $\sigma_{Coverage}$ indicates the uncertainty arising from the data coverage over an

ice shelf, while $\sigma_{Orientation}$ reflects the uncertainty from track orientation. =

## APPENDIX D

# Assessment of Using Spaceborne LiDAR To Monitor the Particulate Backscatter Coefficient on Large, Freshwater Lakes: A Test Using CALIPSO on Lake Michigan

This appendix, which constitutes a supplementary chapter of this thesis, appears in its entirety in the following:

Watkins RH, Sayers MJ, Shuchman RA and Bosse KR (2023a) Assessment of using spaceborne LiDAR to monitor the particulate backscatter coefficient on large, freshwater lakes: A test using CALIPSO on lake michigan. *Frontiers in Remote Sensing*, **4** (doi: 10.3389/frsen.2023.1104681)

## Introduction

The particulate backscatter coefficient, or $b_{bp}$ ($m^{-1}$), is a central inherent optical property that gives important insight into ecological processes that happen in large bodies of water. Specifically, $b_{bp}$ has been used as a proxy for particulate organic carbon in regions where inorganic material concentrations are low (Cetinić and others, 2012). Through this connection, on the global oceans $b_{bp}$ has been used to quantify global carbon stocks (Loisel and others, 2001; Stramski and others, 2008; Martinez-Vicente and others, 2013; Behrenfeld and others, 2013), track the vertical migrations of ocean animals (Burt and Tortell, 2018; Behrenfeld and others, 2019), quantify pri-

mary production (Behrenfeld and others, 2005; Westberry and others, 2008; Schulien and others, 2017), and can be used to potentially monitor the overall health of water environments. Typically, $b_{bp}$ has been sampled globally on the open oceans via two methods. First, by way of in situ collected measurements from ship (Concannon and Prentice, 2008; Dickey and others, 2011), aircraft (Hair and others, 2016; Churnside and others, 2017; Churnside and Marchbanks, 2019), and float surveys (Bittig and others, 2021). Second, by using ocean color data derived from optical imagery satellites such as the MODerate-resolution Imaging Spectroradiometer (MODIS), in which a gridded $b_{bp}$ product is created (Mélin, 2011; Blondeau-Patissier and others, 2014). Both of these methods have paved the path of $b_{bp}$ monitoring over the last 20 years.

While in situ sampling and passive sensors are able to provide $b_{bp}$, they are not without drawbacks. In situ measurements via ship and aircraft are costly and the network of ARGO floats is limited in its spatial coverage. Likewise, MODIS derived $b_{bp}$ can only be collected in the daytime and can have errors associated in excess of 50 percent (Hostetler and others, 2018; Jamet and others, 2019). These drawbacks gave rise to a new era of $b_{bp}$ collection: LiDAR based satellites (Hostetler and others, 2018; Bisson and others, 2021). The Cloud-Aerosol LiDAR and Infrared Pathfinder Satellite Observation (CALIPSO) satellite was launched in 2006 with the primary goal of measuring the properties of clouds and aerosols in Earth's atmosphere using LiDAR (Winker and others, 2009, 2010). However, over the 15 year lifespan of the satellite, secondary uses were identified including its ability to obtain $b_{bp}$, which was first done a decade ago (Behrenfeld and others, 2013). Since then, numerous studies have been done using CALIPSO and other LiDAR based satellites as a way of collecting $b_{bp}$ (Behrenfeld and others, 2016, 2019; Lu and others, 2014a, 2016, 2020;

Bisson and others, 2021).

Most studies which have obtained $b_{bp}$ from CALISPO have done so on the global oceans, though there have been studies done on a more localized scale (Dionisi and others, 2020). To date however, none have been done in a large freshwater environment. This is likely due to the spatial resolution of CALISPO satellite tracks, which are spaced at $\approx$ 150 km apart. On the global oceans this is an acceptable resolution for binning the data into 2 $^\circ$ by 2 $^\circ$ boxes, such as in Behrenfeld and others (2019). However on study regions similar in size to the Great Lakes, this would be ineffective as one bin would span the entire basin of a lake. Another likely reason that CALIPSO has not been used to study large lakes is the need for high resolution (in both time and space) wind speed measurements, which play a large roll in the calculation of $b_{bp}$ (Behrenfeld and others, 2013; Hu and Zhai, 2016).

Inland, freshwater lakes can also be optically complex (case 2, (Morel and Prieur, 1977)) when compared to marine environments (case 1, (Palmer and others, 2015)). This stems mainly from differences in concentrations of optically active constitutes (OAC) compared to sections of the global oceans(Morel and Prieur, 1977; Gons and others, 2008; Mouw and others, 2015). Likewise, the specific biological makeup of phytoplankton assemblages can differ substantially between freshwater and marine environments (Elser and Hassett, 1994). In addition, changes in the vertical distribution of particulate assemblages can vary substantially on freshwater lakes when compared to their marine equivalent (Scofield and others, 2020). These phenomenon present their own set of challenges and are unique to the freshwater remote sensing world.

Drawbacks aside, CALIPSO does make passes over some of the worlds largest freshwater lakes, specifically Lake Michigan in the United States. While it is im-

possible to map trends across the entire lake using CALIPSO, it is possible to map trends across individual, satellite flyover tracks. In the scope of Great Lakes ecosystem, $b_{bp}$ is important to the monitoring of overall lake health. Decreases in $b_{bp}$ over a 14 year period on Lakes Michigan and Huron have been tied to the effect of dreissenid mussels, phosphorus abatement, and climate change on the lakes (Yousef and others, 2017). In addition, $b_{bp}$ has been monitored and used on the lakes as a metric to assess particulate assemblages and better regulate optical signal remote sensing. As the fishing industry on the Great Lakes is upwards of a $7 billion per year trade, being able to remotely sense/monitor the health of the ecosystem through $b_{bp}$ would be extremely valuable (Roth and others, 2012).

Because of high resolution wind speed forecasting obtained from the National Oceanic and Atmospheric Administration (NOAA)'s Great Lakes Coastal Forecasting System (GLCFS) (NOAA, 2022), we are able to obtain $b_{bp}$ from CALIPSO across the lake. Likewise, because of both NOAA cruises over the last decade and because of recent advances in using MODIS to obtain $b_{bp}$ (Shuchman and others, 2013), we are able to compare the results obtained from CALIPSO to others sampled over similar time periods and locations. Here we show a method of obtaining LiDAR derived $b_{bp}$ on large, freshwater lakes and the challenges associated with it. We then compare these results to both in situ values and results obtained through passive sensors. We close by speculating on the roll that LiDAR obtained $b_{bp}$ can play in the future of Great Lakes remote sensing.

## Material and Methods

### CALISPO $b_{bp}$

Data used in deriving bbp from CALIPSO comes from NASA/CNES's LiDAR Level 1B profile data, Version 4-10 product (Winker and others, 2009). For the

majority of this assessment, we followed Behrenfeld and others (2013), implementing changes that have come about over the last decade to improve the reliability of the results (Lu and others, 2013, 2014a, 2021c; Bisson and others, 2021). A schematic of how $b_{bp}$ is derived from CALIPSO is shown in Figure D.1. For the scope of this analysis, $b_{bp}$ refers to the backscatter sampled at 532 nm. At every point along the satellite track, the co-polarized and cross-polarized channel returns are extracted. A cross-talk correction between the two channels is implemented and the transient response from the surface is removed (Lu and others, 2014a, 2021c). The corrected signal is then used to calculate a depolarization ratio ($\delta_t$) between the two channels for the first three bins below the surface of the water. Following this, a series of filtering is done to eliminate signals that would result in a contaminated result. Implementation of this filtering is as follows, as was done in Dionisi and others (2020):

1) Removal of signal that is flagged as saturated in the data product.

Lu and others (2018) implemented a signal saturation flag to the CALIPSO data product. Here, we only consider data that is not saturated in any way, and ignore data that is flagged as possibly saturated or certainly saturated as this signal would not yield reliable results.

2) Removal of signal that had cloud coverage.

Clouds are identified though two sources. First, if the water surface peak from the LiDAR return is not within 120 m of the actual surface (derived from the Digital Elevation Model (DEM) flag on the CALIPSO data), then the signal is considered to be polluted by clouds. Second, if the integrated attenuated backscatter (IAB) for the entire LiDAR return is greater than a threshold value ($0.017sr^{-}1$), then the signal is considered contaminated by clouds (Dionisi and others, 2020).

3) Removal of the signal where the depolarization ratio ($\delta_t$) exceeded 0.5.

Realistic values of the depolarization ratio ($\delta_t$) certainly would be below 0.5 (Dionisi and others, 2020). As such, all data returns with a depolarization ratio greater than 0.5 are not considered.

4) Removal of the signal where the wind speed is less than 2 m/s and greater than 9 m/s.

Low wind speeds (less than $2m/s$) result in signal saturation and high wind speeds (greater than $9m/s$) result in turbid waters. As each of these cases would result in an unreliable signal, they are therefore not considered.

After preliminary filtering of the signal, we were able to start the calculation of $b_{bp}$. This was done through the use of parameters taken from Behrenfeld and others (2013), Bisson and others (2021), and though two dynamic variables. A listing of the constants and values are shown in Table D1. The first dynamic variable used in deriving $b_{bp}$ is the diffuse attenuation coefficient for downwelling irradiance ($K_d$), which is obtained from MODIS optical imagery. Specifics surrounding the acquisition of $K_d$ are shown in Section D.2.2. We chose to directly use the MODIS derived $K_d$ measurements rather than using the empirical relationship for $K_d$ in Bisson and others (2021) because we are analyzing a freshwater environment. As such, the relationship between MODIS $K_d$ and the depolarization ratio ($\delta_t$) may be different. However, it is likely that using either method will result in a very similar result, as the $K_d$ used in Bisson and others (2021) is still derived from MODIS via an empirical relationship.

The second and most important dynamic variable in the derivation of $b_{bp}$ from CALIPSO is water surface wind speed ($v$). Wind speed is used in deriving wave height (Cox and Munk, 1954; Hu and others, 2008), which is directly used in cal-

culating $b_{bp}$ from the depolarization ratio ($\delta_t$). For every point along the CALIPSO tracks, we used a dynamic wind speed obtained from NOAA GLCFS (NOAA, 2022). The high temporal resolution of the wind speed model allowed us to have wind speed measurements down to the same hour of each CALIPSO flyover. High winds will result in waves that make the water too turbid to obtain reliable $b_{bp}$ measurements and low wind speeds can result in signal saturation (Behrenfeld and others, 2013). As such, we implemented a filter by removing all measurements that had a wind speed greater than 9 m/s and less than 2 m/s (Dionisi and others, 2020), as is shown in the pre-processing steps. Thus, we can now define $b_{bp}$ as a function of the depolarization ratio ($\delta_t$), wind speed ($v$), the attenuation coefficient for downwelling irradiance ($K_d$), and the combination of previously defined constants ($C$) following the relationship shown in Behrenfeld and others (2013) as:

$$b_{bp} = C * f(\delta_t, v, K_d) \tag{D.1}$$

**MODIS $b_{bp}$ and $K_d$**

Level 2 MODIS imagery intersecting Lake Michigan was downloaded through the NASA Ocean Biology Processing Group (OBPG; https://oceancolor.gsfc.nasa.gov/). Each image was processed using the Color Producing Agents Algorithm (CPA-A; Shuchman and others (2013)) in order to derive estimates of chlorophyll-a concentration, suspended minerals concentration, and CDOM (Colored Dissolved Organic Matter) absorption. Using these three estimates, bulk absorption and bulk backscatter coefficients were derived for the following MODIS bands: 412, 443, 488, 531, 547, and 667 nm. At the same bands, $b_{bp}$ was computed from the bulk backscatter by removing the backscatter due to pure water (coefficients derived from Morel and oth-

ers (1974)). The diffuse attenuation coefficient ($K_d$) at the above wavelengths was estimated using a method outlined in Lee and others (2005), which uses the bulk absorption and backscatter coefficients as well as the solar zenith angle.

Yearly average images were also computed for both $b_{bp}$ and $K_d$. First, daily average images were generated by computing the mean of overlapping pixels within all satellite images from a given day. The yearly average images were then computed as the mean of all daily images within that year.

**In situ $b_{bp}$**

In situ $b_{bp}$ was sampled by the National Oceanic and Atmospheric Administration's Great Lakes Environmental Research Laboratory (NOAA GLERL). This was done primarily in the spring (March-May) and summer (June-August), with a scattering of samples in the fall (September- November), at several stations on Lake Michigan between 2015 and 2019. Observations of $b_{bp}$ were derived from data collected by a WET Labs BB9 sensor, which measures volume scattering coefficients at 9 wavelengths (412, 440, 488, 510, 532, 595, 650, 676, and 715 nm). During sampling, the BB9 is mounted in a package along with other sensors including a WET Labs ac-s, Sea-Bird CTD, and WET Labs fluorometer. Packaging these sensors provides concurrent measurements of salinity, temperature, and absorption which are necessary for processing BB9 data to $b_{bp}$. The package was deployed vertically through the water column using a crane.

Using the WAP software package (WET Labs), ac-s, CTD, and BB9 data were converted from binary data to text files, and BB9 data were processed to $b_{bp}$ using protocols outlined in Zaneveld and others (2003). First, the total volume scattering function ($\beta_t$) is corrected using the coincident total absorption ($a_t$) measurements from the ac-s after having been re-sampled to the BB9 wavelengths. Next, the vol-

ume scattering function of the water ($\beta_w$) was calculated according to Boss and Pegau (2001), utilizing the coincident CTD-measured temperature and salinity. The particulate fraction of the volume scattering function ($\beta_p$) is calculated as the difference between $\beta_t$ and $\beta_w$. $b_{bp}$ is then computed according to the following equation using a $\chi$ factor of 1.1 (Sullivan and others, 2013):

$$b_{bp} = 2\pi * \chi * \beta_p \tag{D.2}$$

Finally, the $b_{bp}$ data is binned to 1 meter with the vertical profiles then averaged between 0 to 50 m below the water surface.

**Study Regions**

For the scope of this assessment, we chose to limit our study to only Lake Michigan rather than any of the other Great Lakes. This was done purposefully for a two main reasons. First, the way the CALISPO flyovers were oriented coincided very well with the geometry of the lake. For Lake Michigan, the satellite had two unbroken and intersecting day/night tracks that spanned a few degrees of latitude (Figure D.2). This match up allowed us to effectively preform our analysis even with the limited spatial coverage of the CALISPO satellite. Secondly, the distribution of in situ sampled $b_{bp}$ values was the highest in Lake Michigan. This distribution of samples along similar lines of latitude to that of the CALIPSO tracks allowed us to compare our derived product effectively. A map of both of the CALISPO tracks used in this survey along with the locations of all in situ sampling stations is shown in Figure D.2.

## Results

### Yearly average $b_{bp}$ on Lake Michigan

As a first test of the ability to derive $b_{bp}$ from CALIPSO, we computed an average $b_{bp}$ across the entire lake for every year in the data record. We did this for both the daytime and nighttime CALIPSO tracks. To ascertain how this value compared to other measurements of $b_{bp}$, we took a yearly average $b_{bp}$ for the MODIS data at the same location as the CALIPSO data. In conjunction with CALIPSO and MODIS, we also calculated a yearly average $b_{bp}$ for the in situ data across the entire lake. We compared the three metrics in Figure D.3A (daytime) and Figure D.3B (nighttime). As MODIS is unable to sample at nighttime and as there is no documented nighttime $b_{bp}$ samples on Lake Michigan, the nighttime $b_{bp}$ from CALIPSO is compared to daytime measurements.

Our results for the daytime flyovers showed more yearly variability in the CALIPSO $b_{bp}$ than the MODIS $b_{bp}$ (Figure D.3A). However, over the course of the 15 year period, there was no discernible trend in $b_{bp}$ (p value $> 0.05$). The 95 % confidence bounds for the CALIPSO $b_{bp}$ were similar to that of the MODIS derived results, and much smaller than the bounds on the in situ sampling. These results also held for the nighttime CALIPSO results (Figure D.3B). However, the nighttime results are systematically lower for every year in the record when compared to their daytime counterparts and the MODIS/in situ data.

### Seasonal $b_{bp}$ across Lake Michigan

Both cloud cover and high wind speeds limited the return rate of usable CALIPSO data and therefore did not allow us resolve seasonal trends across the lake on a yearly basis. However, because trends across the 15 year time period of the CALIPSO,

MODIS, and in situ data were largely unchanged (relative to the standard error of the in situ measurements), we felt justified in combining the entire time record into a seasonally divided data set and then evaluating this data set spatially across the lake. We did this for both the daytime and nighttime measurements. To start, the daytime measurements across Lake Michigan are shown in Figure D.4A. These results are divided up into four seasons: Spring (March through May), Summer (June though August), Fall (September though November) and Winter (December through February).

At a first order evaluation, for the spring, summer, and fall we see very good coherence between all three methods of collecting Daytime $b_{bp}$ (Figure D.4A). In the winter, we see a much larger divergence between measurements, which is not surprising in that the MODIS result is not well calibrated for winter. This could be related to one or more of the following potential issues. First, the CPA-A, which is used to generate the MODIS $b_{bp}$ estimates, is calibrated based on in situ measurements throughout the lakes (Shuchman and others, 2013). However, because our in situ dataset does not include any measurements collected in winter, it is unclear how suitable the current calibration is during the winter season. Second, the CALIPSO result may also be influenced by ice in the lake. With these issues in mind, CALIPSO may be able to supplement non existent winter sampling campaigns if validation of the result could be performed. The nighttime measurements from CALILPSO again show systematically lower response across all sections of the lake when compared to the daytime sampled results (Figure D.4B). The usable data retrieval rate of the nighttime measurements was also nearly an order of magnitude higher then that of the daytime (7 % vs 1 %).

Also of note is the lack of CALIPSO daytime data between 42.5° and 43.5° lat-

itude. This likely is a direct result of the optical complexity of the waters of Lake Michigan in this region. Satellite optical imagery frequently shows the existence of sediment plumes in this part of the lake (Vanderploeg and others, 2007; Lohrenz and others, 2004), which may be resulting in a CALIPSO return that is flagged as contaminated (for one or more of the previously shown filtering steps). Likewise, this part of the CALIPSO track is mostly nearshore, which further increases the optical complexity of the water and may result in further signal loss. This is also related to the large variability of in situ values in these optically complex waters, which are likely to have more variability in their $b_{bp}$ relative to portions of the lake that are more spatially consistent.

**Comparison of CALIPSO vs MODIS daytime $b_{bp}$**

To a higher level analysis of the daytime results, there is some smaller scale divergence across the lake between the CALIPSO and MODIS measurements. This is especially prevalent in the spring time (Figure D.4A). Taking the in situ values as being ground truth, we next compared the daytime CALIPSO and MODIS $b_{bp}$ results to the their closest measurement spatially on a seasonal basis, taking a median percent error for each season and instrument. We did this for both the spring and the summer separately (when in situ measurements were available) and then also combined the results across all seasons (Figure D.5).

We found that CALIPSO derived $b_{bp}$ showed better agreement relative to the in situ sampling than the MODIS derived $b_{bp}$. This was especially true in the springtime where the CALIPSO $b_{bp}$ had a median percent error of 7 % and the MODIS $b_{bp}$ had a median percent error of 27 %. In the summer, both instruments were nearly the same in their performance, with the CALIPSO (14 % error) only sightly outperforming the MODIS (15 % error). Finally, taken together regardless of season, CALIPSO (8

%) was closer to in situ values than MODIS (18 %).

## Discussion

### Weather dependent return rate of CALIPSO

Our results indicate that CALIPSO can retrieve a reliable $b_{bp}$ signal on a large, freshwater lake. However, deriving trends with a higher resolution than yearly across the entire lake or seasonally across the entire data record is impractical using the CALIPSO data. This is due to a weather dependent return rate of usable CALIPSO backscatter data across the lake. For daytime measurements, the amount of good measurements after filtering is around 1 %. This improves substantially for the nighttime measurements where the amount of usable data climbs to approximately 7 %. However, even at 7 % retrieval, the limited spatially coverage of CALIPSO prevents a more in depth analysis.

Reasons for the low usable data percentage of CALIPSO on the Great Lakes stems mostly from two sources. First, average wind speeds on Lake Michigan are generally around 6 m/s, with values varying both spatially and temporally (Li and others, 2010b). Due to turbid waters at high wind speeds and to signal saturation at low wind speeds, a range of wind speeds of between 2 m/s and 9 m/s is required in order to reliable derive $b_{bp}$ from CALIPSO (Behrenfeld and others, 2013). Many of the CALIPSO flyovers on Lake Michigan take place when the wind speed is greater than the maximum allowed wind speed, resulting in a considerable loss of data. The second major source of data loss comes from the cloud coverage on the great lakes, where the percentage of cloud free days is less than 50 % (Ju and Roy, 2008). Clouds prevent reliable retrieval of the signal from CALIPSO and therefor result in a null measurement.

A final note on the return rate of usable data from CALIPSO is the substantially

higher retrieval rate in the nighttime hours to that of the daytime hours (7 % vs 1 %). This is likely due to the behavior of clouds on wind speeds on Lake Michigan between the daytime and the nighttime. In the daytime, temperature gradients between the lake and the land produce high winds, an effect which may be diminished in the nighttime when temperature gradients are much less steep (Laird and others, 2001). This could result in both less cloud coverage and lower wind speeds on the lake in the evening hours, resulting in a higher data usability rate.

**Substantial Day/Night Difference in CALIPSO $b_{bp}$**

As the usable data retrieval rate for nighttime measurements is higher for CALIPSO, it would be advantageous to use nighttime measurements of $b_{bp}$ to further monitor the Great Lakes. However, our results indicate that there is a substantial offset in nighttime $b_{bp}$ across all years (Figure D.3B) and seasons (Figure D.4B). This offset is sometimes more than 50 % lower than the closest daytime measurement. Theory on the open ocean suggests that the nighttime measurement should be intrinsically 10 % lower due to the diurnal size differences in particulates (Kheireddine and Antoine, 2014; Behrenfeld and others, 2019). This difference could be exacerbated in the freshwater ecosystem where zooplankton and phytoplankton are stoichiometricly distinct compared to their marine equivalent, and therefore could have much different and more amplified diurnal difference to their combined back-scattering (Elser and Hassett, 1994).

The challenge with validating the nighttime CALIPSO measurements is the lack of other sources of nighttime $b_{bp}$ to compare it to. MODIS can only sample in the daytime as it is an optical instrument and there has not yet been any effort to sample $b_{bp}$ in the nighttime across the Great Lakes. Because all current and future LiDAR based satellites will sample in the nighttime, and because the retrieval rate of usable

data for nighttime measurements is nearly an order of magnitude better than daytime measurements, future sampling efforts across the Great Lakes should be gauged to have a nighttime component. This would serve to validate any future spaceborne LiDAR derived $b_{bp}$ measurements.

**CALIPSO $b_{bp}$ as compared to MODIS $b_{bp}$**

Our results indicated that daytime derived CALIPSO $b_{bp}$ aligned better with the in situ sampling when compared to MODIS derived $b_{bp}$. This was especially true in the springtime where CALIPSO measurements were more than 20 % closer to the in situ values than MODIS measurements. However, in the summer months CALIPSO was only slightly closer than MODIS, with a difference between them of less than 1 %. This result is in line with previous studies on the global oceans, where CALIPSO performed better than MODIS when compared to in situ data gathered by the network of ARGO floats (Bisson and others, 2021). However, it should be noted that in situ sampling is quite variable and further analysis would be needed to further examine the performance of the CALIPSO measurements to MODIS measurements. For example, in situ measurements of $b_{bp}$ on Lake Michigan are taken only periodically (usually twice a year) and only at one particular section of the lake. These sampling campaigns also are done via shipborne collection, which are intrinsically time consuming. To set up a more consistent and more efficient sampling campaign, it would be advantageous to establish a system of floats (similar to the open ocean) that could collect in situ values of $b_{bp}$ regularly throughout the year. This would vastly improve the analysis.

The difference in reliability between the spring and summer for MODIS is likely due the summer biasing of the $b_{bp}$ derivation from optical imagery. MODIS derivered $b_{bp}$ is calculated, in part, by using in situ values to calibrate the method. Most of the

in situ sampling that is used to calibrate the MODIS derived product comes from summertime measurements. This results in a heavy biasing towards the summer months which yields a summertime MODIS $b_{bp}$ that aligns better with in situ measurements and a springtime MODIS $b_{bp}$ that diverges. Moreover, there is very little difference in coherence between seasons for CALIPSO because CALISPO derived $b_{bp}$ is independent of in situ sampling campaigns.

**The future of CALIPSO and LiDAR in large lake monitoring**

Here, we derived $b_{bp}$ from a spaceborne, LiDAR based, satellite on a large freshwater lake. We found that $b_{bp}$ derived in this manner matches well with in situ sampled and MODIS derived $b_{bp}$ values. We also found that the LiDAR derived values tend to be closer than the MODIS derived values when compared to the in situ values, however variability in the in situ sampling may be biasing this relationship. That said, the practicality of CALIPSO derived $b_{bp}$ is limited on the Great Lakes due to three main reasons:

1) The weather dependent retrieval rate of daytime measurements is less than 1 %, which makes monitoring small scale trends nearly impossible.

2) The spatial coverage of CALIPSO is limited in the scope of the Great Lakes, where the satellite only makes a few flyovers across repeat tracks.

3) CALIPSO, after 15 years in service, is nearing the end of its usable life and therefor further data that will be acquired by the satellite is likely minimal.

With these drawbacks in mind, the usability of CALIPSO derived $b_{bp}$ on the Great Lakes likely lies in it ability to supplement in situ measurements, which are used to validate the gridded $b_{bp}$ MODIS products. Previously, we stated that CALISPO was more in line with in situ measurements than MODIS, especially in the springtime. This is due to summer biasing which is related to the heavy summer distribution of

in it situ measurements. However, CALIPSO derived results may be able to serve as proxy "in situ" $b_{bp}$ values. This would greatly supplement current sampling efforts and improve MODIS derived $b_{bp}$ products.

Even with CALISPO coming to an end, the future of spaceborne LiDAR derived $b_{bp}$ on the Great Lakes is still bright. Recent studies on the global have used a new LiDAR based satellite that was launched in 2018, ICESat-2, to calculate $b_{bp}$ both as an along track variable and as a function of water depth (Lu and others, 2020, 2021c,b). With considerably higher spatial coverage than CALIPSO and the ability to profile $b_{bp}$ at depth, ICESat-2 could provide valuable information about water quality on the Great Lakes. With that in mind, we believe that that spaceborne LiDAR will be a major component of monitoring efforts on the Great Lakes over the next 10 years.

| Variable Name | Variable Value | Reference |
|---|---|---|
| Below-surface depolarization ratio($\delta_w$) | 0.1 | (Voss and Fry, 1984; Kokhanovsky, 2003) |
| CALIOP's off-nadir pointing angle ($\theta$) | 3 ° | Winker and others (2009) |
| Water surface transmittance ($t$) | 0.98 | (Gilman and Garrett, 1994) |
| CALIPSO to MODIS wavelength conversion ($b(\pi)/b_{bp}$) | 0.32 | (Bisson and others, 2021) |

Table D.1: A listing of the constants used to derive $b_{bp}$ from CALIPSO channel returns. Further information on the derivation can be found in Behrenfeld and others (2013)

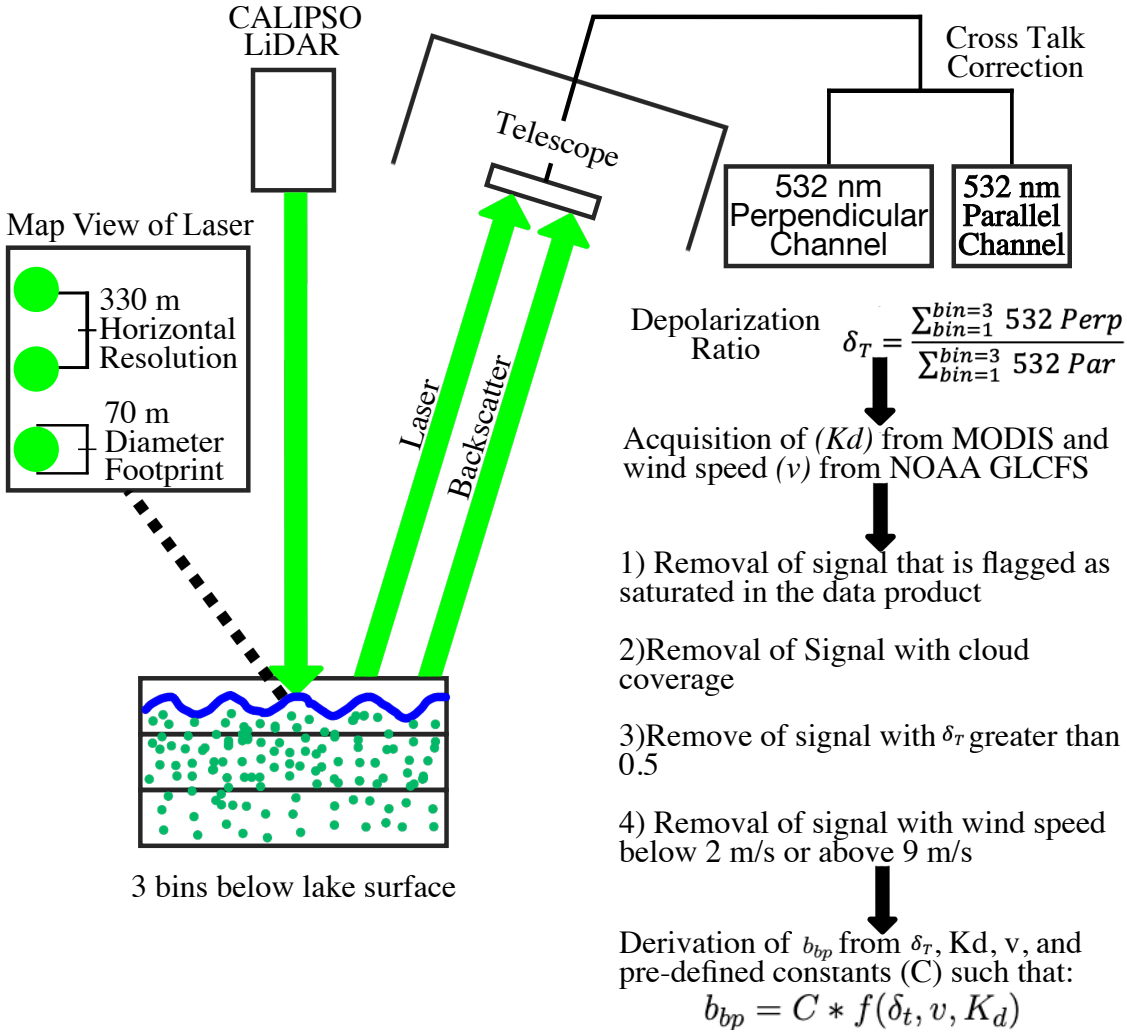


Figure D.1: A schematic of how $b_{bp}$ is obtained using the CALIPSO LiDAR. Briefly, the CALIPSO LiDAR profiles the water using two channels. A depolarization ratio ($\delta_t$) is then calculated from the return, which is then further turned into $b_{bp}$ following the method outlined in the text.

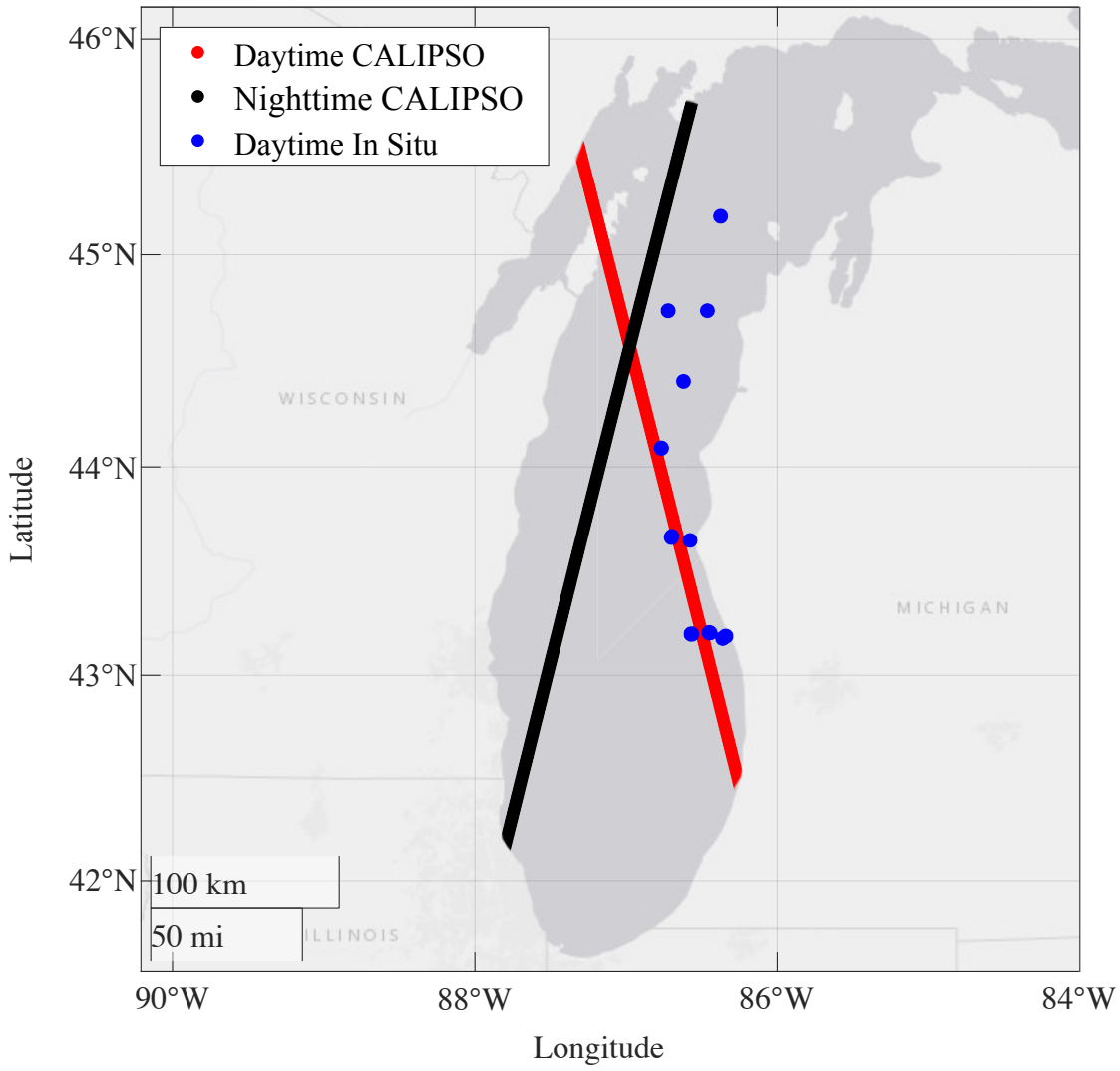


Figure D.2: A map showing the location of the CALIPSO daytime (red), nighttime (black), and in situ (blue) measurement locations across Lake Michigan.

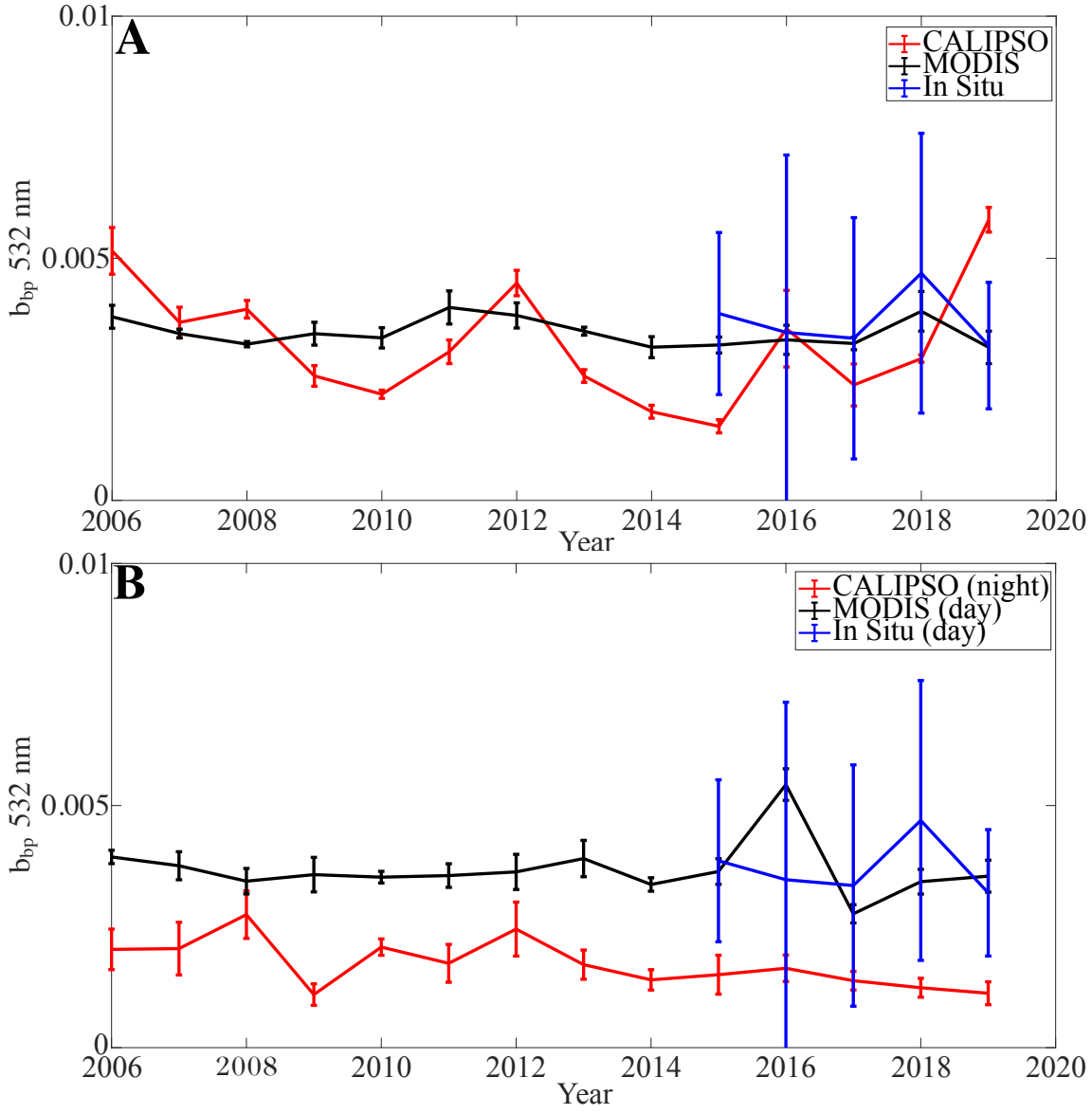


Figure D.3: A) Yearly $b_{bp}$ daytime average across Lake Michigan for CALIPSO (red), MODIS (black), and in situ (blue). B) Yearly $b_{bp}$ nightime average across Lake Michigan for CALIPSO (red), MODIS (black), and in situ (blue). Here, MODIS and in situ values are still sampled in the daytime. Error bars for A) and B) represent 95 % confidence. intervals. Here, MODIS derived values are different across the lake because the daytime and nighttime CALIPSO tracks differ spatially

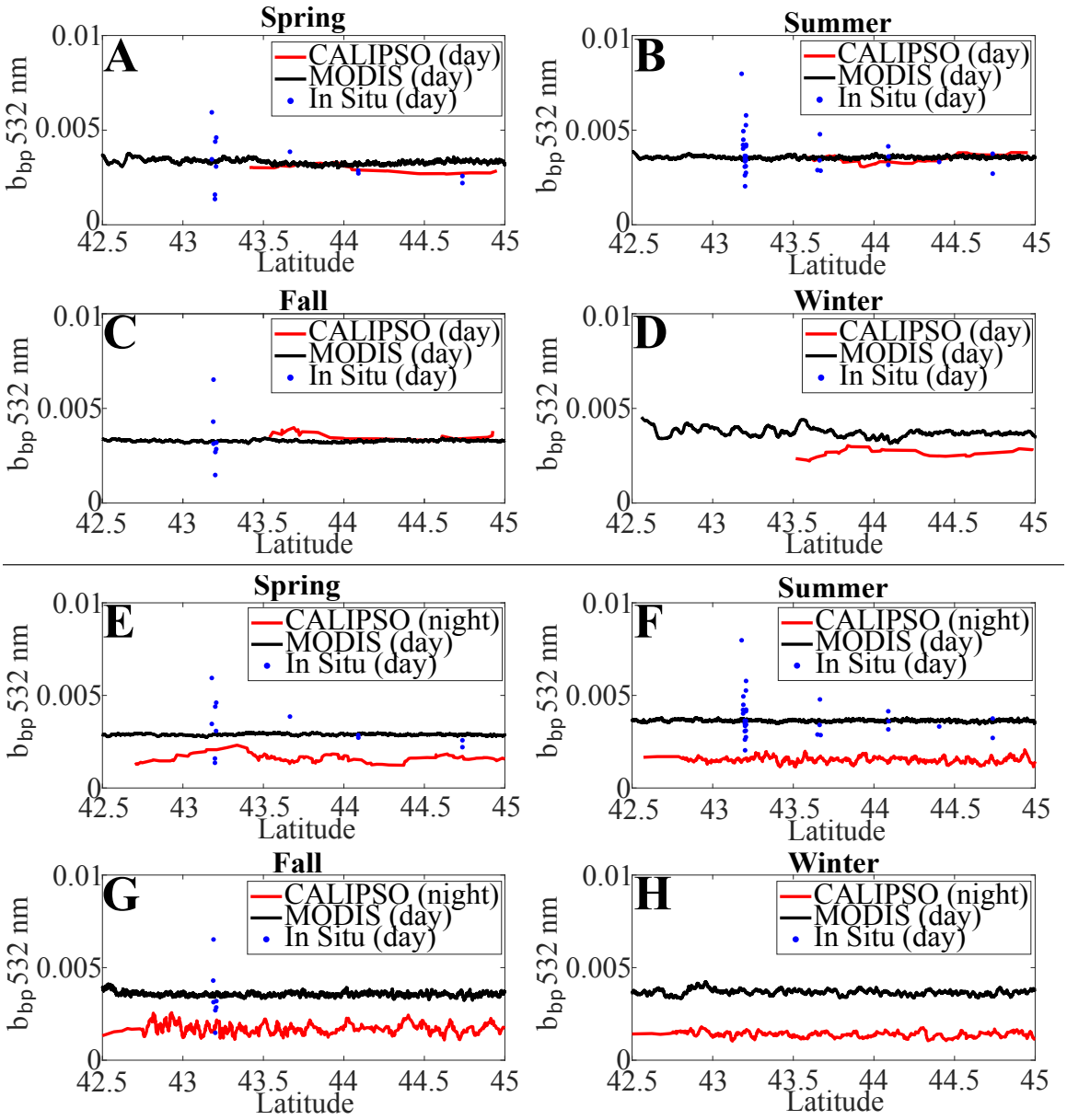


Figure D.4: A-D) Daytime, seasonal measurements for CALIPSO (red), MODIS (black), and in situ (blue) values of $b_{bp}$. E-H)Nighttime, seasonal measurements for CALIPSO (red), MODIS (black), and in situ (blue) values of $b_{bp}$. Once again, MODIS and in situ values are still sampled in the daytime. Large variations in in situ values can be partially attributed to differences in sampling longitude.

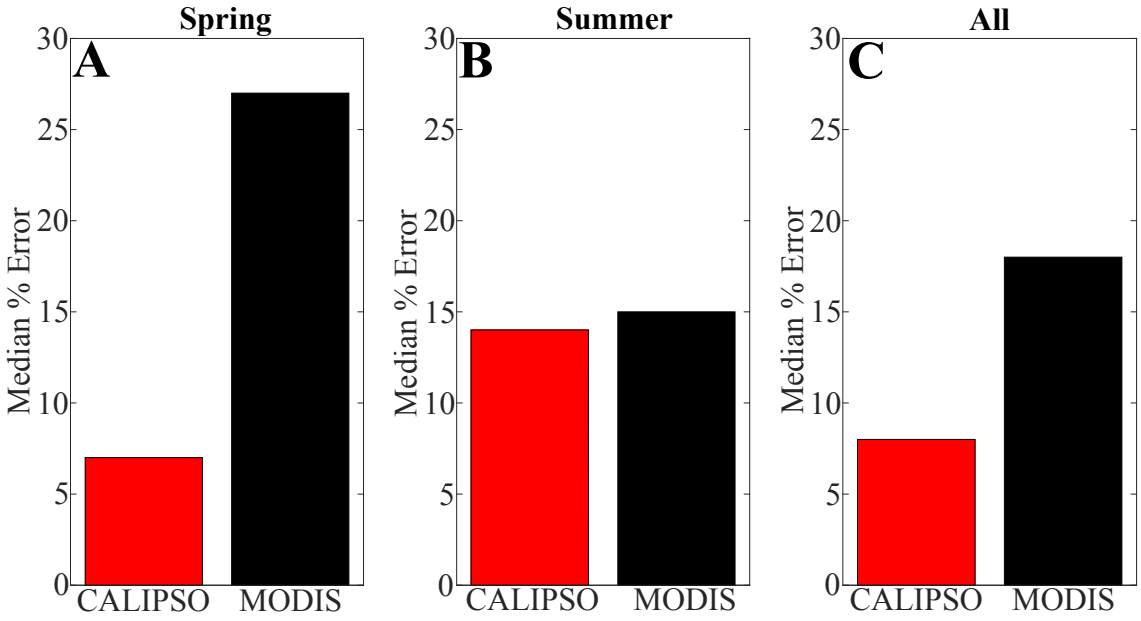


Figure D.5: A) Spring, B)Summer and C)Total percent error in CALISPO (red) and MODIS(black) for daytime measuremnts of $b_{bp}$

## APPENDIX E

# Validation of ICESat-2 Derived Data Products on Freshwater Lakes: Bathymetry, Diffuse Attenuation Coefficient for Downwelling Irradiance ($K_d$), and Particulate Backscatter Coefficient ($b_{bp}$)

This appendix, which constitutes a supplementary chapter of this thesis, appears in its entirety in the following:

Watkins RH, Sayers MJ, Shuchman RA and Bosse KR (2023b) Validation of icesat-2 derived data products on freshwater lakes: Bathymetry, diffuse attenuation coefficient for downwelling irradiance, and particulate backscatter coefficient. *IEEE Geoscience and Remote Sensing Letters*, 1–1 (doi: 10.1109/lgrs.2023.3261551)

ICESat-2 was launched by NASA in 2018 with the primary goals of measuring changes in polar ice sheets, measuring the free-board amount of sea ice, and measuring the amount of vegetation canopy across Earth (Martino and others, 2019). This is done with the onboard ATLAS LiDAR, which uses green (532 nm) light to map photon returns across six beams, resulting in 70 cm along profile resolution (Neuenschwander and Pitts, 2019). Since its launch in 2018, secondary uses of ICESat-2 capabilities have been assessed and implemented. To start, the bathymetry of both shallow coastal seaways (Hsu and others, 2021) and water greater than 25 m has been recorded (Ma and others, 2020), with results typically validated by and com-

bined with optical imagery and in situ values to produce high resolution gridded bathymetry (Li and others, 2019).

Along with bathymetry, by building upon work done with previous spaceborne LiDAR based systems (Behrenfeld and others, 2016; Lu and others, 2014b), recent studies have shown optical properties can be derived from ICESat-2 photon return. Both the diffuse attenuation coefficient for downwelling irradiance ($K_d$) and the particulate backscattering coefficient ($b_{bp}$) can be obtained from from the distribution of photons in the water column (Lu and others, 2020). $b_{bp}$ is a central inherent optical property that gives important insight into ecological processes that happen in large bodies of water. On the global oceans, $b_{bp}$ has been used to quantify global carbon stocks (Martinez-Vicente and others, 2013), track the vertical migrations of ocean animals (Behrenfeld and others, 2019), and quantify primary production (Schulien and others, 2017). Likewise, $K_d$ is critical for understanding how much light is penetrating a given water column (i.e. photic zone depth), which has been shown to control biochemical and physical processes such as primary production that dictate the abundance of life within a water column (Lee and others, 2005).

Most studies calculating ICESat-2 bathymetry and all studies calculating ICESat-2 optical properties have been done on the global oceans. However, ICESat-2 still makes passes over some of the worlds largest lakes, including Lake Michigan. Nearshore bathymetry is important in the scope of the Laurentian Great Lakes as changes due to lake warming can effect the spawning environments of fish and can also change local boating patterns (Zhong and others, 2018). Likewise, decreases in $K_d$ and $b_{bp}$ over a 14 year period on Lake Michigan and Lake Huron have been tied to the effect of dreissenid mussels, phosphorus abatement, and climate change on the lakes (Yousef and others, 2017).

Here, we perform two experiments with respect to ICESat-2. To start, we evaluate for the first time measurements of bathymetry, $K_d$, and $b_{bp}$ calculated from ICESat-2 to in situ values sampled at the same time and location as the satellite flyover. This is done in two separate locations: a large freshwater lake (Lake Michgian) and a small freshwater lake (Big Glen Lake) in the area surrounding Glen Arbor, Michigan, USA. This test serves to validate the reliability of ICESat-2 derived products to ground truth measurements and can be taken as an expansion of past studies in other locations. Second, we appraise the value of spaceborne LiDAR remote sensing as a tool to monitor large, freshwater lakes. We close by commenting on the role that spaceborne LiDAR can play in the future of Great Lakes remote sensing.

## Data and Methods

### In Situ Sampling

Our sampling campaign took place on Lake Michigan and Big Glen Lake in the northwest region of Michigan, USA, as indicated by Figure F.1. Sampling was done in two stages: First, bathymetry data was collected on both lakes via a boat survey using a sonar depth sounder. This was done along the projected path of the ICESat-2 flyover. Lake conditions resulted in a slight horizontal offset between the in situ sampling profile and the ICESat-2 profile, especially on Big Glen Lake. Bathymetric data sampling took place the day prior to the flyover on August 13th, 2021. Optical property sampling on Big Glen Lake also took place on August 13th. Optical property data on Lake Michigan was sampled at approximately the same time as the August 14th, 2021 ICESat-2 flyover, which occurred at $\approx 3:30$ pm EST.

$K_d$ was measured using a Seabird Hyperpro II profiling radiometer following previously reported methods(Sayers and others, 2019). Briefly, the profiler was cast in a free-fall to a geometric depth corresponding to two optical depths at 490 nm, approx-

imately 20 m in Lake Michigan and 13 m in Big Glen Lake. Ten casts were made at each site to reduce the effects of wave focusing in the upper water column. Spectral downwelling plane irradiance ($E_d$) profiles (10) were binned (mean) at 0.5 m depth intervals. Spectral $K_d$ of the first optical depth (depth at which 10 percent of the light just below the surface remains (Gordon and McCluney, 1975)) was computed from the binned profiles by calculating a linear fit of the log transformed $E_d$ profile (from 0 m to 1 optical depth) where the slope of the fit is taken as $K_d$ (m$^-$1).

$b_{bp}$ was computed for nine spectral bands (410, 440, 490, 510, 532, 667, 705, 715) using a Seabird ECO BB-9 scattering meter attached to a profiling frame that also included a Seabird AC-S and CTD. Vertical profiles were made through the photic zone at each site, as estimated from the profiling radiometer. Profiles of $b_{bp}$ were averaged into 0.5 m bins. A Secchi disk was also deployed at each sampling location, as a crude estimation of optical depth is needed for $K_d$ and $b_{bp}$ calculations from ICESat-2.

**ICESat-2 Bathymetry, $K_d$ and $b_{bp}$**

ATLAS/ICESat-2 L2A Global Geolocated Photon Data was used to derive all products. This data set contains the coordinates and elevations of all photons that are returned to ICESat-2 (Neumann and others, 2021). Specifically, we use data from the middle, strong beam of a flyover on Lake Michigan and Big Glen Lake from August 14th, 2021, shown in Figure F.1. Bathymetry was calculated from the photon returns following the procedure in (Ranndal and others, 2021). Here, an empirical calculation is used to group bottom returns from satellite in high, medium, and low confidence readings of the bathymetry. These readings are then corrected for refraction that occurs as the photons move through the water (Parrish and others, 2019). In this study, we only evaluate the high confidence bathymetry returns.

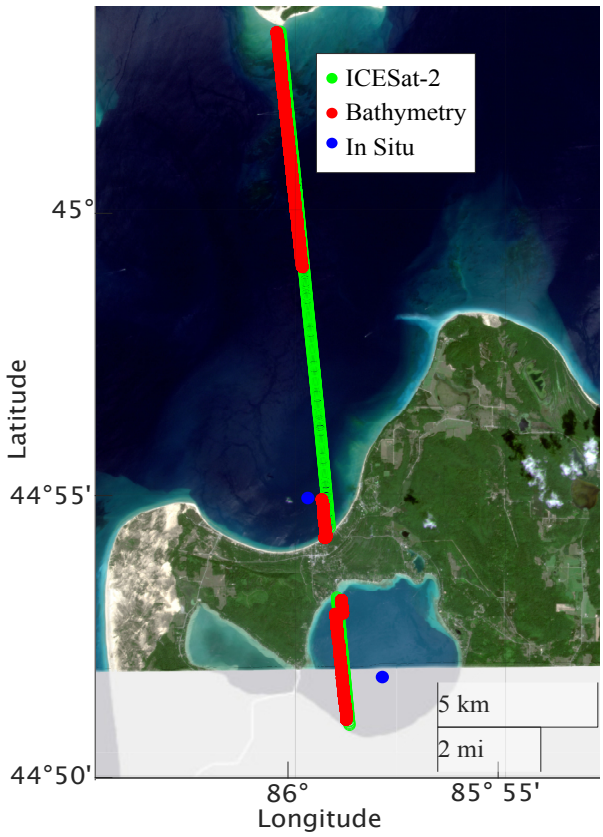


Figure E.1: Sampling location on Lake Michigan and Big Glen Lake. The red line indicates the location of the in situ bathymetric sampling. The blue dots show the location of the optical property in situ sampling. Finally, the green line shows the location of the ICESat-2 flyover. Overlain is the PlanetScope Ortho image of Glen Arbor, MI, USA taken on August 14th, 2021 showing the conditions on Lake Michigan and Big Glen Lake during the ICESat-2 flyover used in this survey. Note the stark difference in water color between Lake Michigan and Big Glen Lake.

Both $K_d$ and $b_{bp}$ are calculated using the method developed by (Lu and others, 2021a, 2020). For the scope of this study, both $K_d$ and $b_{bp}$ refer to the metrics sampled at a wavelength of 532 nm. Here, the photons along the flight-line of the satellite are grouped into 0.001 degree latitude by 0.1 m bins on each body of water. These bins are then normalized and averaged over the length of the flight track to create a photon distribution at depth for each lake. Deconvolution of the signal is performed to remove effects of potential after pulses that occur as the LiDAR signal passes through the water/surface interface.

$K_d$ is then taken as the slope of the decay of the photon signal through the water column between 3 m and 1.5 optical depths, where the limits represent data limitations due to after pulses and LiDAR penetration depth respectively. The optical depths are estimated from Secchi disk measurements, and are taken as 12 m in Lake Michigan and 4 m in Big Glen Lake. Column integrated $b_{bp}$ and depth dependent $b_{bp}$ are calculated directly from the binned, normalized, photon return using predetermined constants and dynamic variables in the derivation. For the scope of our study, we assumed the backscatter of freshwater ($B_w$) to be 0.005 m$^{-}$1 (Thursby and others, 2015) and the wind speed ($v$) to be 7 m * s$^{-}$1 (measured in situ). All other inputs as well as an in depth analysis of these calculations can be found in Lu and others (2020).

## Results

### Bathymetry Validation

We first examined how ICESat-2 derived bathymetry compared to in situ sampled bathymetry at the same relative time (within 24 hours) and the same location. This was done across Big Glen Lake, shown in Figure F.2(a), and Lake Michigan, shown in Figure F.2(b). To start, we looked at the results from Big Glen lake and found a somewhat substantial horizontal offset between the in situ sampled data and the satellite derived data, resulting in a medium difference of 1.22 m. This offset was caused by differences in the sampling line and the satellite line, with the overall trend in the bathymetry being similar between the two sources of data. On Lake Michigan, Figure F.2(b), the in situ sampling line was much closer to the satellite line, resulting in a medium percent difference of only 0.67 m between the two.

Our results from the bathymetry survey also showed the maximum depth that ICESat-2 could reliable sense on freshwater lakes. On Big Glen Lake, the maximum

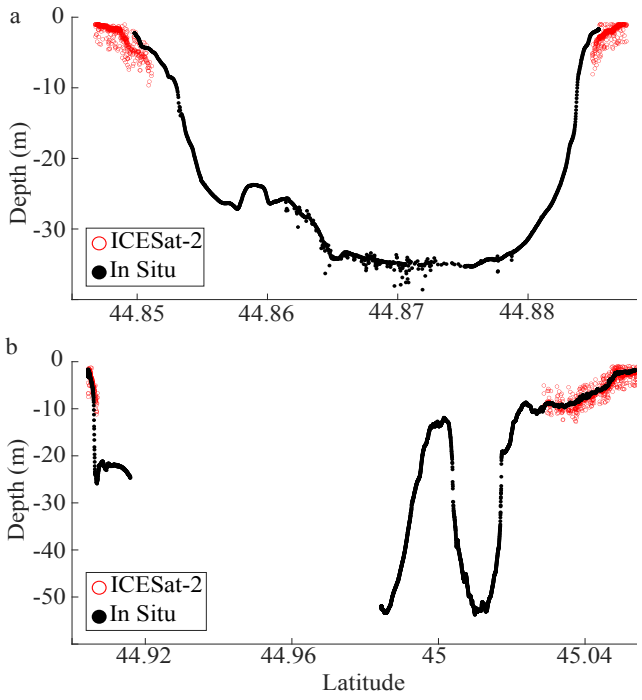


Figure E.2: Comparison between in situ sampled values (black) and ICESat-2 derived values (red). Figure F.2(a) represents Big Glen Lake and Figure F.2(b) represents Lake Michigan. Outliers in in situ sampling values are due to errors in sampling and are not true trends in the data.

sensed depth from ICESat-2 was $\sim$ 8 m while on Lake Michigan, the satellite sensed depth was $\sim$ 12 m. In each location, a Secchi disk was deployed, with results yielding 3.2 m on Big Glen Lake and 12 m on Lake Michigan. Therefore, the maximum depth is largely dependent on the clarity of the water, with increasing clarity (Secchi disk depth) related to larger maximum depth, a occurrence previously noted in other water environments (Parrish and others, 2019).

#### $K_d$ and $b_{bp}$ Validation

We next examined how in situ sampled $K_d$ and $b_{bp}$ values compared to values derived from ICESat-2. To start, we look at our results on Big Glen Lake and find that for $K_d$, the in situ value (0.156 $m^-1$) agreed very well with the satellite derived value (0.158 $m^-1$), with a percent difference of only 1.27 % between them. $K_d$ is

derived from the slope of the blue line shown in Figure F.3(a). On Lake Michigan, shown in Figure F.3(b), we also found that the in situ sampled $K_d$ (0.0996 $m^-1$) agreed very well with the ICESat-2 $K_d$ (0.0921 $m^-1$), with a percent difference of only 7.82 %. Our results for $K_d$ are also consistent with our maximum depth results from our bathymetry survey, with the clearer lake (Lake Michigan) having a lower $K_d$ value than Big Glen Lake. Likewise, our $K_d$ results agree with Secchi disk measurements, where the Secchi depth was much smaller for Big Glen Lake than Lake Michigan.

We also compared satellite derived $b_{bp}$ to in situ sampled $b_{bp}$ on Lake Michigan, shown by Figure F.3(b). This was done by looking at the photon distribution at depth, and then column integrating the result. The photons used to calculate $b_{bp}$ are taken from around 3 m below the surface, down to 1.5 optical depths below the surface (18 m), as indicated by the red points in Figure F.3(b). Our results once again show great coherence between the in situ values (0.0046 $m^-1$) and the satellite values (0.00463 $m^-1$), with a percent difference of only 0.65 %. Unfortunately, we were unable to sample $b_{bp}$ on Big Glen Lake due to limitations of deploying our device on the day of the Big Glen Lake data collect. However, we were still able to derive $b_{bp}$ on Big Glen Lake, which is shown by Figure F.3(a). Here, the value of column integrated $b_{bp}$ was 0.0110 $m^-1$. Though there is no direct compassion to an in situ value, this $b_{bp}$ is consistent with studies that indicate that increasing $K_d$ should yield increasing $b_{bp}$ (Tiwari and Shanmugam, 2013).

#### $b_{bp}$ at depth

Our final analysis compared $b_{bp}$ sampled at depth between in situ value and ICESat-2 derived values on Lake Michigan, which is indicated by Figure F.4(a). Here, $b_{bp}$ is compared at 1 m intervals ranging from 3 m to 1.5 optical depths, which

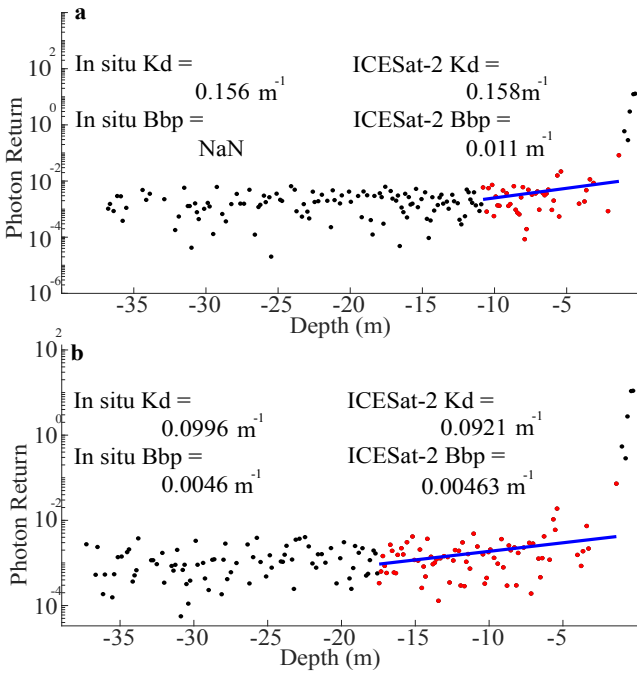


Figure E.3: $K_d$ and $b_{bp}$ comparison between in situ sampled values and ICESat-2 derived values on a) Big Glen Lake and b) Lake Michigan. The black dots in each of figure represent the binned photons while the reds represent the binned photons used in the calculations. The blue line represents the fitted slope in calculating $K_d$

is taken to be 18 m on Lake Michigan. We found a satellite derived $b_{bp}$ at depth that is much more variable than in situ values. The standard deviation at depth for ICESat-2 $b_{bp}$ is 0.0023 m$^{-}$1 while the standard deviation for in situ values is 0.0002 m$^{-}$1, an order of magnitude less. Likewise, the in situ $b_{bp}$ is mostly constant at depth while the ICESat-2 $b_{bp}$ is elevated close to the surface of the water, decays to a minimum of 0.0012 m$^{-}$1 at around 10 m of depth, and then spikes to a maximum value at the bottom of the profile greater than 0.015 m$^{-}$1. Also shown in Figure F.4(b) is the total Chlorophyll a concentration in sampled at depth and the water temperature, both sampled at the same time and location as the in situ values in Figure F.4(a). Note that the water temperature is mostly constant below 5 m, indicating that all data shown was collected above the thermocline.

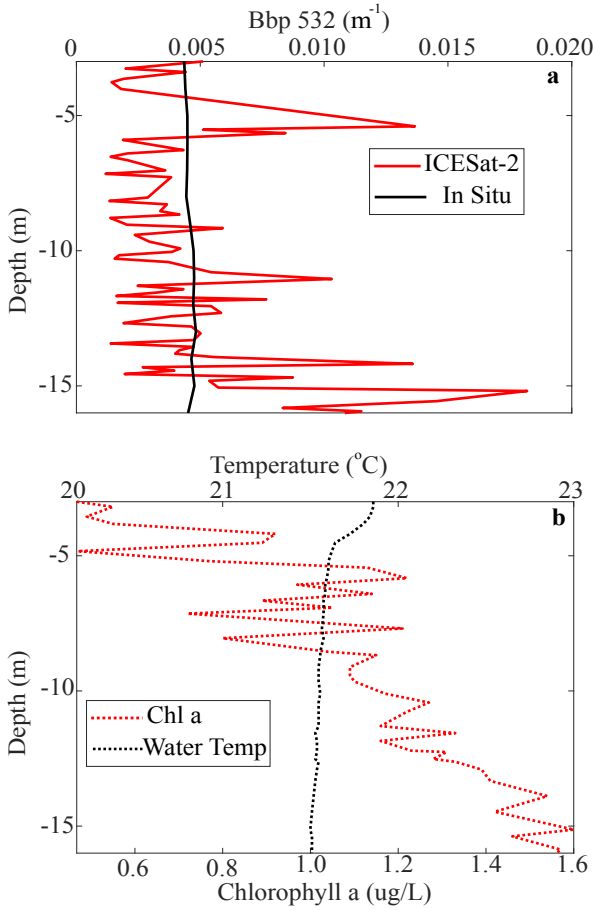


Figure E.4: a)$b_{bp}$ sampled at depth for ICESat-2 (red) and in situ values (black).b) Chlorophyll a (red dotted) and water temperature (black dotted) in situ sampled values at the same location/time as those in Figure F.4(a)

## Discussion

Here, for the first time, we compare a variety of ICESat-2 derived metrics regrading the subsurface properties of freshwater to the same metrics sampled in situ within the same day of each other. To start, we looked at the bathymetry on two separate lakes with different levels of water clarity and found that ICESat-2 was an effective tool for measuring mid-depth bathymetry. Specifically, ICESat-2 was able to measure the bathymetry effectively down to approximately one optical depth, which is variable between lakes based upon the water clarity at the given location. The depth

limit likely partially stems from only taking the high confidence bathymetry photons. If medium and low confidence signals are considered, this would likely increase the range of depths that are able to be observed by ICESat-2, but would also likely increase errors.

In the study, we also examined the effectiveness of monitoring $K_d$ on large, freshwater lakes using ICESat-2. We found that in two different lakes with differing optical properties, ICESat-2 derived $K_d$ values agreed almost perfectly with in situ sampled values. This was also verified empirically by comparing Secci disc depths between the two locations. Likewise, in looking at the contrast in water color in the optical satellite imagery, we can also draw an empirical conclusion that both bodies of water should have substantially different values of $K_d$ (Figure F.1). While $K_d$ was only sampled at one location for ICESat-2, by taking an average value over a segment of the flyover $K_d$ can also be derived at every point along every satellite flyover on Lake Michigan. This could effectively map and monitor how $K_d$ changes in different locations on the lake. Likewise, there are approximately six separate flyovers (depending on the quality of the data return) in varying locations on Lake Michigan every month, which would allow for monitoring of $K_d$ on the lake on a monthly basis.

The final subsurface metric that was monitored using ICESat-2 on the freshwater lakes in our survey was $b_{bp}$. This was done as a column integrated value of Lake Michigan and Big Glen Lake, and also calculated as a function of depth on Lake Michigan. On Lake Michigan, where in situ $b_{bp}$ was also sampled, the column integrated $b_{bp}$ from ICESat-2 was again nearly identical to the in situ sampled value. For the $b_{bp}$ at depth, ICESat-2 was able to effectively sample $b_{bp}$ between 3 m and 18 m (1.5 optical depths). Compared the in situ values at the depth, the ICESat-2

results were much more variable. This is likely related to taking an average across a 10 km long satellite track as oppose to sampling at one particular location. However, trends in the ICESat-2 derived $b_{bp}$ (Figure F.4(a)) seem to correlate with trends in Chlorophyll a concentration where both metrics increase as a function of depth. That said, further sampling and analysis is needed to validate any connections between the two. Finally, as with $K_d$, $b_{bp}$ could also be sampled across all of Lake Michigan on a monthly basis, which is likely where the applicability of these results lie. Here, the structure of the water column (in regards to $b_{bp}$) between 3 m and 18 m could also be mapped, which would be novel for a large, freshwater lake.

**Conclusions**

In closing, we report that ICESat-2 will be a valuable tool in the future of monitoring and remote sensing of not only Lake Michigan, but other large, freshwater, bodies of water. A comparison between in situ values and satellite derived values of bathymetry, $K_d$, and $b_{bp}$ all show good coherence. We note that more sampling campaigns are likely needed for a more through evaluation of the metrics, especially for nighttime flyovers of ICESat-2, which were not evaluated in this study. However, the preliminary results from this survey certainly point towards the incorporation of ICESat-2 into the remote sensing toolbox on the Great Lakes and beyond.

# Bibliography

Adusumilli S, Fricker HA, Medley B, Padman L and Siegfried MR (2020) Interannual variations in meltwater input to the southern ocean from antarctic ice shelves. *Nature Geoscience*, **13**(9), 616–620 (doi: 10.1038/s41561-020-0616-z)

Allen C, Leuschen C, Gogineni P, Rodriguez-Morales F and Paden J (2010) Icebridge mcords l2 ice thickness, version 1 (doi: 10.5067/GDQ0CUCVTE2Q)

Alley KE, Scambos TA, Siegfried MR and Fricker HA (2016) Impacts of warm water on antarctic ice shelf stability through basal channel formation. *Nature Geoscience*, **9**(4), 290–293 (doi: 10.1038/ngeo2675)

Alley KE, SCAMBOS TA, ANDERSON RS, RAJARAM H, POPE A and HARAN TM (2018) Continent-wide estimates of antarctic strain rates from landsat 8-derived velocity grids. *Journal of Glaciology*, **64**(244), 321–332 (doi: 10.1017/jog.2018.23)

Alley KE, Scambos TA, Alley RB and Holschuh N (2019) Troughs developed in ice-stream shear margins precondition ice shelves for ocean-driven breakup. *Science Advances*, **5**(10) (doi: 10.1126/sciadv.aax2215)

Alley KE, Wild CT, Luckman A, Scambos TA, Truffer M, Pettit EC, Muto A, Wallin B, Klinger M, Sutterley T, Child SF, Hulen C, Lenaerts JTM, Maclennan M, Keenan E and Dunmire D (2021) Two decades of dynamic change and progressive

destabilization on the thwaites eastern ice shelf. *The Cryosphere*, **15**(11), 5187–5203 (doi: 10.5194/tc-15-5187-2021)

Alley KE, Scambos TA and Alley RB (2023) The role of channelized basal melt in ice-shelf stability: recent progress and future priorities. *Annals of Glaciology*, 1–5 (doi: 10.1017/aog.2023.5)

Arndt JE, Larter RD, Friedl P, Gohl K and and KH (2018) Bathymetric controls on calving processes at pine island glacier. *The Cryosphere*, **12**(6), 2039–2050 (doi: 10.5194/tc-12-2039-2018)

Banwell AF, MacAyeal DR and Sergienko OV (2013) Breakup of the larsen b ice shelf triggered by chain reaction drainage of supraglacial lakes. *Geophysical Research Letters*, **40**(22), 5872–5876 (doi: 10.1002/2013gl057694)

Bassis J and Ma Y (2015a) Evolution of basal crevasses links ice shelf stability to ocean forcing. *Earth and Planetary Science Letters*, **409**, 203–211 (doi: 10.1016/j.epsl.2014.11.003)

Bassis J and Ma Y (2015b) Evolution of basal crevasses links ice shelf stability to ocean forcing. *Earth and Planetary Science Letters*, **409**, 203–211 (doi: 10.1016/j.epsl.2014.11.003)

Bassis JN and Jacobs S (2013) Diverse calving patterns linked to glacier geometry. *Nature Geoscience*, **6**(10), 833–836 (doi: 10.1038/ngeo1887)

Bassis JN and Walker CC (2011) Upper and lower limits on the stability of calving glaciers from the yield strength envelope of ice. *Proceedings of the Royal Society A: Mathematical, Physical and Engineering Sciences*, **468**(2140), 913–931 (doi: 10.1098/rspa.2011.0422)

Bassis JN, Berg B, Crawford AJ and Benn DI (2021a) Transition to marine ice cliff instability controlled by ice thickness gradients and velocity. *Science*, **372**(6548), 1342–1344 (doi: 10.1126/science.abf6271)

Bassis JN, Berg B, Crawford AJ and Benn DI (2021b) Transition to marine ice cliff instability controlled by ice thickness gradients and velocity. *Science*, **372**(6548), 1342–1344 (doi: 10.1126/science.abf6271)

Behrenfeld MJ, Boss E, Siegel DA and Shea DM (2005) Carbon-based ocean productivity and phytoplankton physiology from space. *Global Biogeochemical Cycles*, **19**(1) (doi: 10.1029/2004gb002299)

Behrenfeld MJ, Hu Y, Hostetler CA, Dall'Olmo G, Rodier SD, Hair JW and Trepte CR (2013) Space-based lidar measurements of global ocean carbon stocks. *Geophysical Research Letters*, **40**(16), 4355–4360 (doi: 10.1002/grl.50816)

Behrenfeld MJ, Hu Y, O'Malley RT, Boss ES, Hostetler CA, Siegel DA, Sarmiento JL, Schulien J, Hair JW, Lu X, Rodier S and Scarino AJ (2016) Annual boom–bust cycles of polar phytoplankton biomass revealed by space-based lidar. *Nature Geoscience*, **10**(2), 118–122 (doi: 10.1038/ngeo2861)

Behrenfeld MJ, Gaube P, Penna AD, O'Malley RT, Burt WJ, Hu Y, Bontempi PS, Steinberg DK, Boss ES, Siegel DA, Hostetler CA, Tortell PD and Doney SC (2019) Global satellite-observed daily vertical migrations of ocean animals. *Nature*, **576**(7786), 257–261 (doi: 10.1038/s41586-019-1796-9)

Bernales J, Rogozhina I and Thomas M (2017) Melting and freezing under antarctic ice shelves from a combination of ice-sheet modelling and observations. *Journal of Glaciology*, **63**(240), 731–744 (doi: 10.1017/jog.2017.42)

Bindschadler R, Vaughan DG and Vornberger P (2011) Variability of basal melt beneath the pine island glacier ice shelf, west antarctica. *Journal of Glaciology*, **57**(204), 581–595 (doi: 10.3189/002214311797409802)

Bishop MP, Björnsson H, Haeberli W, Oerlemans J, Shroder JF and Tranter M (2011) *Encyclopedia of snow, ice and glaciers*. Springer Science & Business Media

Bisson KM, Boss E, Werdell PJ, Ibrahim A and Behrenfeld MJ (2021) Particulate backscattering in the global ocean: A comparison of independent assessments. *Geophysical Research Letters*, **48**(2) (doi: 10.1029/2020gl090909)

Bittig H, Wong A and Plant J (2021) *BGC-Argo synthetic profile file processing and format on Coriolis GDAC*. Ifremer (doi: 10.13155/55637)

Blondeau-Patissier D, Gower JF, Dekker AG, Phinn SR and Brando VE (2014) A review of ocean color remote sensing methods and statistical techniques for the detection, mapping and analysis of phytoplankton blooms in coastal and open oceans. *Progress in Oceanography*, **123**, 123–144 (doi: 10.1016/j.pocean.2013.12.008)

Boss E and Pegau WS (2001) Relationship of light scattering at an angle in the backward direction to the backscattering coefficient. *Applied Optics*, **40**(30), 5503–5507

Burt WJ and Tortell PD (2018) Observations of zooplankton diel vertical migration from high-resolution surface ocean optical measurements. *Geophysical Research Letters*, **45**(24) (doi: 10.1029/2018gl079992)

Cetinić I, Perry MJ, Briggs NT, Kallin E, D'Asaro EA and Lee CM (2012) Particulate organic carbon and inherent optical properties during 2008 north atlantic bloom

experiment. *Journal of Geophysical Research: Oceans*, **117**(C6) (doi: https://doi.org/10.1029/2011JC007771)

Churnside J, Marchbanks R, Lembke C and Beckler J (2017) Optical backscattering measured by airborne lidar and underwater glider. *Remote Sensing*, **9**(4), 379 (doi: 10.3390/rs9040379)

Churnside JH and Marchbanks RD (2019) Calibration of an airborne oceanographic lidar using ocean backscattering measurements from space. *Optics Express*, **27**(8), A536 (doi: 10.1364/oe.27.00a536)

Clauset A, Shalizi CR and Newman MEJ (2009) Power-law distributions in empirical data. *SIAM Review*, **51**(4), 661–703 (doi: 10.1137/070710111)

Cochran JR, Tinto KJ and Bell RE (2020) Detailed bathymetry of the continental shelf beneath the getz ice shelf, west antarctica. *Journal of Geophysical Research: Earth Surface*, **125**(10) (doi: 10.1029/2019jf005493)

Concannon BM and Prentice JE (2008) Loco with a shipboard lidar. Technical report, NAVAL AIR SYSTEMS COMMAND PATUXENT RIVER MD

Cornford SL, Martin DF, Payne AJ, Ng EG, Le Brocq AM, Gladstone RM, Edwards TL, Shannon SR, Agosta C, van den Broeke MR, Hellmer HH, Krinner G, Ligtenberg SRM, Timmermann R and Vaughan DG (2015) Century-scale simulations of the response of the west antarctic ice sheet to a warming climate. *The Cryosphere*, **9**(4), 1579–1600 (doi: 10.5194/tc-9-1579-2015)

Cox C and Munk W (1954) Measurement of the roughness of the sea surface from photographs of the sun's glitter. *Journal of the Optical Society of America*, **44**(11), 838 (doi: 10.1364/josa.44.000838)

Crawford AJ, Benn DI, Todd J, Åström JA, Bassis JN and Zwinger T (2021) Marine ice-cliff instability modeling shows mixed-mode ice-cliff failure and yields calving rate parameterization. *Nature Communications*, **12**(1) (doi: 10.1038/s41467-021-23070-7)

Cuffey KM (2010) *The Physics of Glaciers*. Academic Press, ISBN 0123694612

Dallaston MC, Hewitt IJ and Wells AJ (2015) Channelization of plumes beneath ice shelves. *Journal of Fluid Mechanics*, **785**, 109–134 (doi: 10.1017/jfm.2015.609)

Das I, Padman L, Bell RE, Fricker HA, Tinto KJ, Hulbe CL, Siddoway CS, Dhakal T, Frearson NP, Mosbeux C, Cordero SI and Siegfried MR (2020) Multidecadal basal melt rates and structure of the ross ice shelf, antarctica, using airborne ice penetrating radar. *Journal of Geophysical Research: Earth Surface*, **125**(3) (doi: 10.1029/2019jf005241)

DeConto RM and Pollard D (2016) Contribution of antarctica to past and future sea-level rise. *Nature*, **531**(7596), 591–597 (doi: 10.1038/nature17145)

Dickey TD, Kattawar GW and Voss KJ (2011) Shedding new light on light in the ocean. *Physics Today*, **64**(4), 44–49 (doi: 10.1063/1.3580492)

Dionisi D, Brando VE, Volpe G, Colella S and Santoleri R (2020) Seasonal distributions of ocean particulate optical properties from spaceborne lidar measurements in mediterranean and black sea. *Remote Sensing of Environment*, **247**, 111889 (doi: 10.1016/j.rse.2020.111889)

Dixon D (2007) Antarctic mean annual temperature map (doi: 10.7265/N51C1TTV)

Doake CSM, Corr HFJ, Rott H, Skvarca P and Young NW (1998) Breakup and con-

ditions for stability of the northern larsen ice shelf, antarctica. *Nature*, **391**(6669), 778–780 (doi: 10.1038/35832)

Dow CF, Lee WS, Greenbaum JS, Greene CA, Blankenship DD, Poinar K, Forrest AL, Young DA and Zappa CJ (2018) Basal channels drive active surface hydrology and transverse ice shelf fracture. *Science Advances*, **4**(6) (doi: 10.1126/sciadv.aao7212)

Drews R (2015) Evolution of ice-shelf channels in antarctic ice shelves. *The Cryosphere*, **9**(3), 1169–1181 (doi: 10.5194/tc-9-1169-2015)

Dupont TK and Alley RB (2005) Assessment of the importance of ice-shelf buttressing to ice-sheet flow. *Geophysical Research Letters*, **32**(4), n/a–n/a (doi: 10.1029/2004gl022024)

Dutrieux P, Vaughan DG, Corr HFJ, Jenkins A, Holland PR, Joughin I and Fleming AH (2013) Pine island glacier ice shelf melt distributed at kilometre scales. *The Cryosphere*, **7**(5), 1543–1555 (doi: 10.5194/tc-7-1543-2013)

Dutrieux P, Stewart C, Jenkins A, Nicholls KW, Corr HFJ, Rignot E and Steffen K (2014) Basal terraces on melting ice shelves. *Geophysical Research Letters*, **41**(15), 5506–5513 (doi: 10.1002/2014gl060618)

Earth Resources Observation and Science (EROS) Center (2018) Landsat image mosaic of antarctica (LIMA)

Elser JJ and Hassett RP (1994) A stoichiometric analysis of the zooplankton–phytoplankton interaction in marine and freshwater ecosystems. *Nature*, **370**(6486), 211–213 (doi: 10.1038/370211a0)

Favier L, Durand G, Cornford SL, Gudmundsson GH, Gagliardini O, Gillet-Chaulet F, Zwinger T, Payne AJ and Brocq AML (2014) Retreat of pine island glacier controlled by marine ice-sheet instability. *Nature Climate Change*, **4**(2), 117–121 (doi: 10.1038/nclimate2094)

Favier L, Pattyn F, Berger S and Drews R (2016) Dynamic influence of pinning points on marine ice-sheet stability: a numerical study in dronning maud land, east antarctica. *The Cryosphere*, **10**(6), 2623–2635 (doi: 10.5194/tc-10-2623-2016)

Francis D, Fonseca R, Mattingly KS, Marsh OJ, Lhermitte S and Cherif C (2022) Atmospheric triggers of the brunt ice shelf calving in february 2021. *Journal of Geophysical Research: Atmospheres*, **127**(11) (doi: 10.1029/2021jd036424)

Fretwell P, Pritchard HD, Vaughan DG, Bamber JL, Barrand NE, Bell R, Bianchi C, Bingham RG, Blankenship DD, Casassa G, Catania G, Callens D, Conway H, Cook AJ, Corr HFJ, Damaske D, Damm V, Ferraccioli F, Forsberg R, Fujita S, Gim Y, Gogineni P, Griggs JA, Hindmarsh RCA, Holmlund P, Holt JW, Jacobel RW, Jenkins A, Jokat W, Jordan T, King EC, Kohler J, Krabill W, Riger-Kusk M, Langley KA, Leitchenkov G, Leuschen C, Luyendyk BP, Matsuoka K, Mouginot J, Nitsche FO, Nogi Y, Nost OA, Popov SV, Rignot E, Rippin DM, Rivera A, Roberts J, Ross N, Siegert MJ, Smith AM, Steinhage D, Studinger M, Sun B, Tinto BK, Welch BC, Wilson D, Young DA, Xiangbin C and Zirizzotti A (2013) Bedmap2: improved ice bed, surface and thickness datasets for antarctica. *The Cryosphere*, **7**(1), 375–393 (doi: 10.5194/tc-7-375-2013)

Fricker HA (2005) Multi-year monitoring of rift propagation on the amery ice shelf, east antarctica. *Geophysical Research Letters*, **32**(2) (doi: 10.1029/2004gl021036)

Gilman C and Garrett C (1994) Heat flux parameterizations for the mediterranean

sea: The role of atmospheric aerosols and constraints from the water budget. *Journal of Geophysical Research*, **99**(C3), 5119 (doi: 10.1029/93jc03069)

Gladish CV, Holland DM, Holland PR and Price SF (2012) Ice-shelf basal channels in a coupled ice/ocean model. *Journal of Glaciology*, **58**(212), 1227–1244 (doi: 10.3189/2012jog12j003)

Glen JW (1953) Rate of flow of polycrystalline ice. *Nature*, **172**(4381), 721–722 (doi: 10.1038/172721a0)

Gons HJ, Auer MT and Effler SW (2008) MERIS satellite chlorophyll mapping of oligotrophic and eutrophic waters in the laurentian great lakes. *Remote Sensing of Environment*, **112**(11), 4098–4106 (doi: 10.1016/j.rse.2007.06.029)

Gordon HR and McCluney WR (1975) Estimation of the depth of sunlight penetration in the sea for remote sensing. *Applied Optics*, **14**(2), 413 (doi: 10.1364/ao.14.000413)

Gourmelen N, Goldberg DN, Snow K, Henley SF, Bingham RG, Kimura S, Hogg AE, Shepherd A, Mouginot J, Lenaerts JTM, Ligtenberg SRM and Berg WJ (2017) Channelized melting drives thinning under a rapidly melting antarctic ice shelf. *Geophysical Research Letters*, **44**(19), 9796–9804 (doi: 10.1002/2017gl074929)

Greene CA, Gardner AS, Schlegel NJ and Fraser AD (2022) Antarctic calving loss rivals ice-shelf thinning. *Nature* (doi: 10.1038/s41586-022-05037-w)

Gudmundsson GH (2013) Ice-shelf buttressing and the stability of marine ice sheets. *The Cryosphere*, **7**(2), 647–655 (doi: 10.5194/tc-7-647-2013)

Hair J, Hostetler C, Hu Y, Behrenfeld M, Butler C, Harper D, Hare R, Berkoff T, Cook A, Collins J, Stockley N, Twardowski M, Cetinić I, Ferrare R and Mack

T (2016) Combined atmospheric and ocean profiling from an airborne high spectral resolution lidar. *EPJ Web of Conferences*, **119**, 22001 (doi: 10.1051/epjconf/201611922001)

Hesari MZ, Nunziata F, Aulicino G, Buono A and Migliaccio M (2022) Analysis of fine-scale dynamics of the drygalski ice tongue in antarctica using satellite SAR data. *International Journal of Remote Sensing*, **43**(7), 2581–2598 (doi: 10.1080/01431161.2022.2064199)

Hogg AE and Gudmundsson GH (2017) Impacts of the larsen-c ice shelf calving event. *Nature Climate Change*, **7**(8), 540–542 (doi: 10.1038/nclimate3359)

Holland PR, Corr HFJ, Vaughan DG, Jenkins A and Skvarca P (2009) Marine ice in larsen ice shelf. *Geophysical Research Letters*, **36**(11) (doi: 10.1029/2009gl038162)

Horton R (2022) Offline: Resuscitating the white giants. *The Lancet*, **399**(10332), 1289 (doi: 10.1016/s0140-6736(22)00612-2)

Hostetler CA, Behrenfeld MJ, Hu Y, Hair JW and Schulien JA (2018) Spaceborne lidar in the study of marine systems. *Annual Review of Marine Science*, **10**(1), 121–147 (doi: 10.1146/annurev-marine-121916-063335)

Howat I, Porter C, Noh MJ, Husby E, Khuvis S, Danish E, Tomko K, Gardiner J, Negrete A, Yadav B, Klassen J, Kelleher C, Cloutier M, Bakker J, Enos J, Arnold G, Bauer G and Morin P (2022) The reference elevation model of antarctica - mosaics, version 2 (doi: 10.7910/DVN/EBW8UC)

Hsu HJ, Huang CY, Jasinski M, Li Y, Gao H, Yamanokuchi T, Wang CG, Chang TM, Ren H, Kuo CY and Tseng KH (2021) A semi-empirical scheme for bathymetric

mapping in shallow water by ICESat-2 and sentinel-2: A case study in the south china sea. *ISPRS J. Photogramm. Remote Sens.*, **178**, 1–19

Hu Y and Zhai P (2016) Development and validation of the CALIPSO ocean subsurface data. In *2016 IEEE International Geoscience and Remote Sensing Symposium (IGARSS)*, IEEE (doi: 10.1109/igarss.2016.7729981)

Hu Y, Stamnes K, Vaughan M, Pelon J, Weimer C, Wu D, Cisewski M, Sun W, Yang P, Lin B, Omar A, Flittner D, Hostetler C, Trepte C, Winker D, Gibson G and Santa-Maria M (2008) Sea surface wind speed estimation from space-based lidar measurements. *Atmospheric Chemistry and Physics*, **8**(13), 3593–3601 (doi: 10.5194/acp-8-3593-2008)

Humbert A, Christmann J, Corr HFJ, Helm V, Höyns LS, Hofstede C, Müller R, Neckel N, Nicholls KW, Schultz T, Steinhage D, Wolovick M and Zeising O (2022) On the evolution of an ice shelf melt channel at the base of filchner ice shelf, from observations and viscoelastic modeling. *The Cryosphere*, **16**(10), 4107–4139 (doi: 10.5194/tc-16-4107-2022)

Indrigo C, Dow CF, Greenbaum JS and Morlighem M (2020) Drygalski ice tongue stability influenced by rift formation and ice morphology. *Journal of Glaciology*, **67**(262), 243–252 (doi: 10.1017/jog.2020.99)

Ishalina OT, Bliakharskii DP and Florinsky IV (2021) Recognition of crevasses with high-resolution digital elevation models: Application of geomorphometric modeling and texture analysis. *Transactions in GIS*, **25**(5), 2529–2552 (doi: 10.1111/tgis.12790)

Jamet C, Ibrahim A, Ahmad Z, Angelini F, Babin M, Behrenfeld MJ, Boss E, Cairns B, Churnside J, Chowdhary J, Davis AB, Dionisi D, Duforêt-Gaurier L, Franz B,

Frouin R, Gao M, Gray D, Hasekamp O, He X, Hostetler C, Kalashnikova OV, Knobelspiesse K, Lacour L, Loisel H, Martins V, Rehm E, Remer L, Sanhaj I, Stamnes K, Stamnes S, Victori S, Werdell J and Zhai PW (2019) Going beyond standard ocean color observations: Lidar and polarimetry. *Frontiers in Marine Science*, **6** (doi: 10.3389/fmars.2019.00251)

Jenkins A, Nicholls KW and Corr HFJ (2010) Observation and parameterization of ablation at the base of ronne ice shelf, antarctica. *Journal of Physical Oceanography*, **40**(10), 2298–2312 (doi: 10.1175/2010jpo4317.1)

Jenkins A, Shoosmith D, Dutrieux P, Jacobs S, Kim TW, Lee SH, Ha HK and Stammerjohn S (2018) West antarctic ice sheet retreat in the amundsen sea driven by decadal oceanic variability. *Nature Geoscience*, **11**(10), 733–738 (doi: 10.1038/s41561-018-0207-4)

Jeofry H, Ross N, Brocq AL, Graham AG, Li J, Gogineni P, Morlighem M, Jordan T and Siegert MJ (2018) Hard rock landforms generate 130 km ice shelf channels through water focusing in basal corrugations. *Nature Communications*, **9**(1) (doi: 10.1038/s41467-018-06679-z)

Jeong S, Howat IM and Bassis JN (2016a) Accelerated ice shelf rifting and retreat at pine island glacier, west antarctica. *Geophysical Research Letters*, **43**(22), 11,720–11,725 (doi: 10.1002/2016gl071360)

Jeong S, Howat IM and Bassis JN (2016b) Accelerated ice shelf rifting and retreat at pine island glacier, west antarctica. *Geophysical Research Letters*, **43**(22) (doi: 10.1002/2016gl071360)

Joe J, Scaraggi M and Barber J (2017) Effect of fine-scale roughness on the tractions

between contacting bodies. *Tribology International*, **111**, 52–56 (doi: 10.1016/j.triboint.2017.03.001)

Jordan JR, Holland PR, Jenkins A, Piggott MD and Kimura S (2014) Modeling ice-ocean interaction in ice-shelf crevasses. *Journal of Geophysical Research: Oceans*, **119**(2), 995–1008 (doi: 10.1002/2013jc009208)

Joughin I (2005) Calving of large tabular icebergs from ice shelf rift systems. *Geophysical Research Letters*, **32**(2) (doi: 10.1029/2004gl020978)

Joughin I, Smith BE and Medley B (2014) Marine ice sheet collapse potentially under way for the thwaites glacier basin, west antarctica. *Science*, **344**(6185), 735–738 (doi: 10.1126/science.1249055)

Joughin I, Shapero D, Smith B, Dutrieux P and Barham M (2021) Ice-shelf retreat drives recent pine island glacier speedup. *Science Advances*, **7**(24), eabg3080 (doi: 10.1126/sciadv.abg3080)

Ju J and Roy DP (2008) The availability of cloud-free landsat data over the conterminous united states and globally. *Remote Sensing of Environment*, **112**(3), 1196–1211 (doi: 10.1016/j.rse.2007.08.011)

Khazendar A, Rignot E, Schroeder DM, Seroussi H, Schodlok MP, Scheuchl B, Mouginot J, Sutterley TC and Velicogna I (2016) Rapid submarine ice melting in the grounding zones of ice shelves in west antarctica. *Nature Communications*, **7**(1) (doi: 10.1038/ncomms13243)

Kheireddine M and Antoine D (2014) Diel variability of the beam attenuation and backscattering coefficients in the northwestern mediterranean sea (BOUSSOLE

site). *Journal of Geophysical Research: Oceans*, **119**(8), 5465–5482 (doi: 10.1002/2014jc010007)

Kokhanovsky AA (2003) Parameterization of the mueller matrix of oceanic waters. *Journal of Geophysical Research*, **108**(C6) (doi: 10.1029/2001jc001222)

Konrad H, Shepherd A, Gilbert L, Hogg AE, McMillan M, Muir A and Slater T (2018) Net retreat of antarctic glacier grounding lines. *Nature Geoscience*, **11**(4), 258–262 (doi: 10.1038/s41561-018-0082-z)

Kulessa B, Jansen D, Luckman AJ, King EC and Sammonds PR (2014) Marine ice regulates the future stability of a large antarctic ice shelf. *Nature Communications*, **5**(1) (doi: 10.1038/ncomms4707)

Laird NF, Kristovich DAR, Liang XZ, Arritt RW and Labas K (2001) Lake michigan lake breezes: Climatology, local forcing, and synoptic environment. *Journal of Applied Meteorology*, **40**(3), 409–424 (doi: 10.1175/1520-0450(2001)040<0409:lmlbcl>2.0.co;2)

Larour E, Rignot E, Poinelli M and Scheuchl B (2021) Physical processes controlling the rifting of larsen c ice shelf, antarctica, prior to the calving of iceberg a68. *Proceedings of the National Academy of Sciences*, **118**(40) (doi: 10.1073/pnas.2105080118)

Larter RD (2022) Basal melting, roughness and structural integrity of ice shelves. *Geophysical Research Letters*, **49**(4) (doi: 10.1029/2021gl097421)

Lee ZP, Darecki M, Carder KL, Davis CO, Stramski D and Rhea WJ (2005) Diffuse attenuation coefficient of downwelling irradiance: An evaluation of remote sensing methods. *Journal of Geophysical Research: Oceans*, **110**(C2)

Lhermitte S, Sun S, Shuman C, Wouters B, Pattyn F, Wuite J, Berthier E and Nagler T (2020) Damage accelerates ice shelf instability and mass loss in amundsen sea embayment. *Proceedings of the National Academy of Sciences*, **117**(40), 24735–24741 (doi: 10.1073/pnas.1912890117)

Li X, Sun B, Siegert MJ, Bingham RG, Tang X, Zhang D, Cui X and Zhang X (2010a) Characterization of subglacial landscapes by a two-parameter roughness index. *Journal of Glaciology*, **56**(199), 831–836 (doi: 10.3189/002214310794457326)

Li X, Zhong S, Bian X and Heilman WE (2010b) Climate and climate variability of the wind power resources in the great lakes region of the united states. *Journal of Geophysical Research*, **115**(D18) (doi: 10.1029/2009jd013415)

Li X, Rignot E, Morlighem M, Mouginot J and Scheuchl B (2015) Grounding line retreat of totten glacier, east antarctica, 1996 to 2013. *Geophysical Research Letters*, **42**(19), 8049–8056 (doi: 10.1002/2015gl065701)

Li Y, Gao H, Jasinski MF, Zhang S and Stoll JD (2019) Deriving high-resolution reservoir bathymetry from ICESat-2 prototype photon-counting lidar and landsat imagery. *IEEE Transactions on Geoscience and Remote Sensing*, **57**(10), 7883–7893 (doi: 10.1109/tgrs.2019.2917012)

Lilly J and Olhede S (2009) Higher-order properties of analytic wavelets. *IEEE Transactions on Signal Processing*, **57**(1), 146–160 (doi: 10.1109/tsp.2008.2007607)

Lilly JM (2017) Element analysis: a wavelet-based method for analysing time-localized events in noisy time series. *Proceedings of the Royal Society A: Mathematical, Physical and Engineering Science*, **473**(2200), 20160776 (doi: 10.1098/rspa.2016.0776)

Lilly JM and Olhede SC (2012) Generalized morse wavelets as a superfamily of analytic wavelets. *IEEE Transactions on Signal Processing*, **60**(11), 6036–6041 (doi: 10.1109/tsp.2012.2210890)

Liu Y, Moore JC, Cheng X, Gladstone RM, Bassis JN, Liu H, Wen J and Hui F (2015) Ocean-driven thinning enhances iceberg calving and retreat of antarctic ice shelves. *Proceedings of the National Academy of Sciences*, **112**(11), 3263–3268 (doi: 10.1073/pnas.1415137112)

Lohrenz SE, Fahnenstiel GL, Millie DF, Schofield OME, Johengen T and Bergmann T (2004) Spring phytoplankton photosynthesis, growth, and primary production and relationships to a recurrent coastal sediment plume and river inputs in southeastern lake michigan. *Journal of Geophysical Research*, **109**(C10) (doi: 10.1029/2004jc002383)

Loisel H, Bosc E, Stramski D, Oubelkheir K and Deschamps PY (2001) Seasonal variability of the backscattering coefficient in the mediterranean sea based on satellite SeaWiFS imagery. *Geophysical Research Letters*, **28**(22), 4203–4206 (doi: 10.1029/2001gl013863)

Lovejoy S (1982) Area-perimeter relation for rain and cloud areas. *Science*, **216**(4542), 185–187 (doi: 10.1126/science.216.4542.185)

Lu X, Hu Y, Liu Z, Zeng S and Trepte C (2013) CALIOP receiver transient response study. In JA Shaw and DA LeMaster (eds.), *SPIE Proceedings*, SPIE (doi: 10.1117/12.2033589)

Lu X, Hu Y, Trepte C, Zeng S and Churnside JH (2014a) Ocean subsurface studies with the CALIPSO spaceborne lidar. *Journal of Geophysical Research: Oceans*, **119**(7), 4305–4317 (doi: 10.1002/2014jc009970)

Lu X, Hu Y, Trepte C, Zeng S and Churnside JH (2014b) Ocean subsurface studies with the CALIPSO spaceborne lidar. *Journal of Geophysical Research: Oceans*, **119**(7), 4305–4317 (doi: 10.1002/2014jc009970)

Lu X, Hu Y, Pelon J, Trepte C, Liu K, Rodier S, Zeng S, Lucker P, Verhappen R, Wilson J, Audouy C, Ferrier C, Haouchine S, Hunt B and Getzewich B (2016) Retrieval of ocean subsurface particulate backscattering coefficient from spaceborne CALIOP lidar measurements. *Optics Express*, **24**(25), 29001 (doi: 10.1364/oe.24.029001)

Lu X, Hu Y, Yang Y, Vaughan M, Liu Z, Rodier S, Hunt W, Powell K, Lucker P and Trepte C (2018) Laser pulse bidirectional reflectance from CALIPSO mission. *Atmospheric Measurement Techniques*, **11**(6), 3281–3296 (doi: 10.5194/amt-11-3281-2018)

Lu X, Hu Y, Yang Y, Bontempi P, Omar A and Baize R (2020) Antarctic spring ice-edge blooms observed from space by ICESat-2. *Remote Sensing of Environment*, **245**, 111827 (doi: 10.1016/j.rse.2020.111827)

Lu X, Hu Y, Omar A, Baize R, Vaughan M, Rodier S, Kar J, Getzewich B, Lucker P, Trepte C, Hostetler C and Winker D (2021a) Global ocean studies from CALIOP/CALIPSO by removing polarization crosstalk effects. *Remote Sensing*, **13**(14), 2769 (doi: 10.3390/rs13142769)

Lu X, Hu Y, Yang Y, Neumann T, Omar A, Baize R, Vaughan M, Rodier S, Getzewich B, Lucker P, Trepte C, Hostetler C and Winker D (2021b) New ocean subsurface optical properties from space lidars: CALIOP/CALIPSO and ATLAS/ICESat-2. *Earth and Space Science*, **8**(10) (doi: 10.1029/2021ea001839)

Lu X, Hu Y, Yang Y, Vaughan M, Palm S, Trepte C, Omar A, Lucker P and Baize R (2021c) Enabling value added scientific applications of ICESat-2 data with effective removal of afterpulses. *Earth and Space Science*, **8**(6) (doi: 10.1029/2021ea001729)

Luckman A, Jansen D, Kulessa B, King EC, Sammonds P and Benn DI (2012) Basal crevasses in larsen c ice shelf and implications for their global abundance. *The Cryosphere*, **6**(1), 113–123 (doi: 10.5194/tc-6-113-2012)

Luckman A, Benn DI, Cottier F, Bevan S, Nilsen F and Inall M (2015) Calving rates at tidewater glaciers vary strongly with ocean temperature. *Nature Communications*, **6**(1) (doi: 10.1038/ncomms9566)

Ma Y, Xu N, Liu Z, Yang B, Yang F, Wang XH and Li S (2020) Satellite-derived bathymetry using the ICESat-2 lidar and sentinel-2 imagery datasets. *Remote Sensing of Environment*, **250**, 112047 (doi: 10.1016/j.rse.2020.112047)

Mandelbrot BB and Wheeler JA (1983) The fractal geometry of nature. *American Journal of Physics*, **51**(3), 286–287 (doi: 10.1119/1.13295)

Marsh OJ, Fricker HA, Siegfried MR, Christianson K, Nicholls KW, Corr HFJ and Catania G (2016) High basal melting forming a channel at the grounding line of ross ice shelf, antarctica. *Geophysical Research Letters*, **43**(1), 250–255 (doi: 10.1002/2015gl066612)

Martin DF, Cornford SL and Payne AJ (2019) Millennial-scale vulnerability of the antarctic ice sheet to regional ice shelf collapse. *Geophysical Research Letters*, **46**(3), 1467–1475 (doi: 10.1029/2018gl081229)

Martinez-Vicente V, Dall'Olmo G, Tarran G, Boss E and Sathyendranath S (2013)

Optical backscattering is correlated with phytoplankton carbon across the atlantic ocean. *Geophysical Research Letters*, **40**(6), 1154–1158 (doi: 10.1002/grl.50252)

Martino AJ, Neumann TA, Kurtz NT and McLennan D (2019) ICESat-2 mission overview and early performance. In SP Neeck, T Kimura and P Martimort (eds.), *Sensors, Systems, and Next-Generation Satellites XXIII*, SPIE (doi: 10.1117/12.2534938)

McCormack FS, Roberts JL, Gwyther DE, Morlighem M, Pelle T and Galton-Fenzi BK (2021) The impact of variable ocean temperatures on totten glacier stability and discharge. *Geophysical Research Letters*, **48**(10) (doi: 10.1029/2020gl091790)

McGrath D, Steffen K, Scambos T, Rajaram H, Casassa G and Lagos JLR (2012) Basal crevasses and associated surface crevassing on the larsen c ice shelf, antarctica, and their role in ice-shelf instability. *Annals of Glaciology*, **53**(60), 10–18 (doi: 10.3189/2012aog60a005)

Mélin F (2011) Comparison of SeaWiFS and MODIS time series of inherent optical properties for the adriatic sea. *Ocean Science*, **7**(3), 351–361 (doi: 10.5194/os-7-351-2011)

Miles BWJ, Stokes CR, Jenkins A, Jordan JR, Jamieson SSR and Gudmundsson GH (2020) Intermittent structural weakening and acceleration of the thwaites glacier tongue between 2000 and 2018. *Journal of Glaciology*, **66**(257), 485–495 (doi: 10.1017/jog.2020.20)

Milillo P, Rignot E, Rizzoli P, Scheuchl B, Mouginot J, Bueso-Bello J and Prats-Iraola P (2019) Heterogeneous retreat and ice melt of thwaites glacier, west antarctica. *Science Advances*, **5**(1), eaau3433 (doi: 10.1126/sciadv.aau3433)

Morel A and Prieur L (1977) Analysis of variations in ocean color1. *Limnology and Oceanography*, **22**(4), 709–722 (doi: 10.4319/lo.1977.22.4.0709)

Morel A and others (1974) Optical properties of pure water and pure sea water.

Morlighem M (2019) Measures bedmachine antarctica, version 1 (doi: 10.5067/C2GFER6PTOS4)

Morlighem M, Rignot E, Binder T, Blankenship D, Drews R, Eagles G, Eisen O, Ferraccioli F, Forsberg R, Fretwell P, Goel V, Greenbaum JS, Gudmundsson H, Guo J, Helm V, Hofstede C, Howat I, Humbert A, Jokat W, Karlsson NB, Lee WS, Matsuoka K, Millan R, Mouginot J, Paden J, Pattyn F, Roberts J, Rosier S, Ruppel A, Seroussi H, Smith EC, Steinhage D, Sun B, van den Broeke MR, van Ommen TD, van Wessem M and Young DA (2019) Deep glacial troughs and stabilizing ridges unveiled beneath the margins of the antarctic ice sheet. *Nature Geoscience*, **13**(2), 132–137 (doi: 10.1038/s41561-019-0510-8)

Mouw CB, Greb S, Aurin D, DiGiacomo PM, Lee Z, Twardowski M, Binding C, Hu C, Ma R, Moore T, Moses W and Craig SE (2015) Aquatic color radiometry remote sensing of coastal and inland waters: Challenges and recommendations for future satellite missions. *Remote Sensing of Environment*, **160**, 15–30 (doi: 10.1016/j.rse.2015.02.001)

Nakayama Y, Manucharyan G, Zhang H, Dutrieux P, Torres HS, Klein P, Seroussi H, Schodlok M, Rignot E and Menemenlis D (2019) Pathways of ocean heat towards pine island and thwaites grounding lines. *Scientific Reports*, **9**(1) (doi: 10.1038/s41598-019-53190-6)

Neuenschwander A and Pitts K (2019) The ATL08 land and vegetation product

for the ICESat-2 mission. *Remote Sensing of Environment*, **221**, 247–259 (doi: 10.1016/j.rse.2018.11.005)

Neumann TA, A Brenner, D Hancock, J Robbins, J Saba, K Harbeck, A Gibbons, J Lee, S B Luthcke and T Rebold (2021) Atlas/icesat-2 l2a global geolocated photon data, version 5 (doi: 10.5067/ATLAS/ATL03.005)

NOAA (2022) Noaa great lakes coastal forecasting system (glcfs), [lake michigan wind speed; 2006-2019]

Obase T, Abe-Ouchi A, Kusahara K, Hasumi H and Ohgaito R (2017) Responses of basal melting of antarctic ice shelves to the climatic forcing of the last glacial maximum and CO2 doubling. *Journal of Climate*, **30**(10), 3473–3497 (doi: 10.1175/jcli-d-15-0908.1)

Paden J, Li J, Leuschen C, Rodriguez-Morales F and Hale R (2010) Icebridge mcords l2 ice thickness, version 1 (doi: 10.5067/gdq0cucvte2q)

Palmer SC, Kutser T and Hunter PD (2015) Remote sensing of inland waters: Challenges, progress and future directions. *Remote Sensing of Environment*, **157**, 1–8 (doi: 10.1016/j.rse.2014.09.021)

Parrish CE, Magruder LA, Neuenschwander AL, Forfinski-Sarkozi N, Alonzo M and Jasinski M (2019) Validation of ICESat-2 ATLAS bathymetry and analysis of ATLAS's bathymetric mapping performance. *Remote Sensing*, **11**(14), 1634 (doi: 10.3390/rs11141634)

Pritchard HD and Vaughan DG (2007) Widespread acceleration of tidewater glaciers on the antarctic peninsula. *Journal of Geophysical Research*, **112**(F3) (doi: 10.1029/2006jf000597)

Pritchard HD, Ligtenberg SRM, Fricker HA, Vaughan DG, van den Broeke MR and Padman L (2012) Antarctic ice-sheet loss driven by basal melting of ice shelves. *Nature*, **484**(7395), 502–505 (doi: 10.1038/nature10968)

Pörtner HO, Roberts D, Masson-Delmotte V, Zhai P, Tignor M, Poloczanska E, Mintenbeck K, M Nicolai AO, Petzold J and B Rama NWe (2019) *IPCC, 2019: Summary for Policymakers*. U.S. Dept. of the Interior, U.S. Geological Survey

Ranndal H, Christiansen PS, Kliving P, Andersen OB and Nielsen K (2021) Evaluation of a statistical approach for extracting shallow water bathymetry signals from ICESat-2 ATL03 photon data. *Remote Sensing*, **13**(17), 3548 (doi: 10.3390/rs13173548)

Rignot E (2004) Accelerated ice discharge from the antarctic peninsula following the collapse of larsen b ice shelf. *Geophysical Research Letters*, **31**(18) (doi: 10.1029/2004gl020697)

Rignot E and Steffen K (2008) Channelized bottom melting and stability of floating ice shelves. *Geophysical Research Letters*, **35**(2) (doi: 10.1029/2007gl031765)

Rignot E, Jacobs S, Mouginot J and Scheuchl B (2013) Ice-shelf melting around antarctica. *Science*, **341**(6143), 266–270 (doi: 10.1126/science.1235798)

Rignot E, Mouginot J, Morlighem M, Seroussi H and Scheuchl B (2014) Widespread, rapid grounding line retreat of pine island, thwaites, smith, and kohler glaciers, west antarctica, from 1992 to 2011. *Geophysical Research Letters*, **41**(10), 3502–3509 (doi: 10.1002/2014gl060140)

Rignot E, Mouginot J, Scheuchl B, van den Broeke M, van Wessem MJ and Morlighem M (2019a) Four decades of antarctic ice sheet mass balance from

1979–2017. *Proceedings of the National Academy of Sciences*, **116**(4), 1095–1103 (doi: 10.1073/pnas.1812883116)

Rignot E, Mouginot J, Scheuchl B, van den Broeke M, van Wessem MJ and Morlighem M (2019b) Four decades of antarctic ice sheet mass balance from 1979–2017. *Proceedings of the National Academy of Sciences*, **116**(4), 1095–1103 (doi: 10.1073/pnas.1812883116)

Rignot E, Mouginot J, Scheuchl B and Jeong S (2022) Changes in antarctic ice sheet motion derived from satellite radar interferometry between 1995 and 2022. *Geophysical Research Letters*, **49**(23) (doi: 10.1029/2022gl100141)

Rippin D, Bingham R, Jordan T, Wright A, Ross N, Corr H, Ferraccioli F, Brocq AL, Rose K and Siegert M (2014) Basal roughness of the institute and möller ice streams, west antarctica: Process determination and landscape interpretation. *Geomorphology*, **214**, 139–147 (doi: 10.1016/j.geomorph.2014.01.021)

Robel AA and Banwell AF (2019) A speed limit on ice shelf collapse through hydrofracture. *Geophysical Research Letters*, **46**(21), 12092–12100 (doi: 10.1029/2019gl084397)

Roth B, Mandrak N, Hrabik T, Sass G and Peters J (2012) *Fishes and decapod crustaceans of the Great Lakes basin*, 105–135

Rott H, Skvarca P and Nagler T (1996) Rapid collapse of northern larsen ice shelf, antarctica. *Science*, **271**(5250), 788–792 (doi: 10.1126/science.271.5250.788)

Rydt JD, Gudmundsson GH, Nagler T and Wuite J (2019) Calving cycle of the brunt ice shelf, antarctica, driven by changes in ice shelf geometry. *The Cryosphere*, **13**(10), 2771–2787 (doi: 10.5194/tc-13-2771-2019)

Sayers MJ, Bosse KR, Shuchman RA, Ruberg SA, Fahnenstiel GL, Leshkevich GA, Stuart DG, Johengen TH, Burtner AM and Palladino D (2019) Spatial and temporal variability of inherent and apparent optical properties in western lake erie: Implications for water quality remote sensing. *Journal of Great Lakes Research*, **45**(3), 490–507 (doi: 10.1016/j.jglr.2019.03.011)

Scambos T, Hulbe C and Fahnestock M (2003) Climate-induced ice shelf disintegration in the antarctic peninsula. In *Antarctic Peninsula Climate Variability: Historical and Paleoenvironmental Perspectives*, 79–92, American Geophysical Union (doi: 10.1029/ar079p0079)

Scambos T, Fricker HA, Liu CC, Bohlander J, Fastook J, Sargent A, Massom R and Wu AM (2009) Ice shelf disintegration by plate bending and hydro-fracture: Satellite observations and model results of the 2008 wilkins ice shelf break-ups. *Earth and Planetary Science Letters*, **280**(1-4), 51–60 (doi: 10.1016/j.epsl.2008.12.027)

Scambos TA (2004) Glacier acceleration and thinning after ice shelf collapse in the larsen b embayment, antarctica. *Geophysical Research Letters*, **31**(18) (doi: 10.1029/2004gl020670)

Scambos TA, Haran TM, Fahnestock MA, Painter TH and Bohlander J (2007) MODIS-based mosaic of antarctica (MOA) data sets: Continent-wide surface morphology and snow grain size. *Remote Sens. Environ.*, **111**(2-3), 242–257

Schmidt BE, Washam P, Davis PED, Nicholls KW, Holland DM, Lawrence JD, Riverman KL, Smith JA, Spears A, Dichek DJG, Mullen AD, Clyne E, Yeager B, Anker P, Meister MR, Hurwitz BC, Quartini ES, Bryson FE, Basinski-Ferris A, Thomas C, Wake J, Vaughan DG, Anandakrishnan S, Rignot E, Paden J and

Makinson K (2023) Heterogeneous melting near the thwaites glacier grounding line. *Nature*, **614**(7948), 471–478 (doi: 10.1038/s41586-022-05691-0)

Schoof C (2007) Ice sheet grounding line dynamics: Steady states, stability, and hysteresis. *Journal of Geophysical Research*, **112**(F3) (doi: 10.1029/2006jf000664)

Schulien JA, Behrenfeld MJ, Hair JW, Hostetler CA and Twardowski MS (2017) Vertically- resolved phytoplankton carbon and net primary production from a high spectral resolution lidar. *Optics Express*, **25**(12), 13577 (doi: 10.1364/oe.25.013577)

Scofield AE, Watkins JM, Osantowski E and Rudstam LG (2020) Deep chlorophyll maxima across a trophic state gradient: A case study in the laurentian great lakes. *Limnology and Oceanography*, **65**(10), 2460–2484 (doi: 10.1002/lno.11464)

Scott JB, Smith AM, Bingham RG and Vaughan DG (2010) Crevasses triggered on pine island glacier, west antarctica, by drilling through an exceptional melt layer. *Annals of Glaciology*, **51**(55), 65–70 (doi: 10.3189/172756410791392763)

Selley HL, Hogg AE, Cornford S, Dutrieux P, Shepherd A, Wuite J, Floricioiu D, Kusk A, Nagler T, Gilbert L, Slater T and Kim TW (2021) Widespread increase in dynamic imbalance in the getz region of antarctica from 1994 to 2018. *Nature Communications*, **12**(1) (doi: 10.1038/s41467-021-21321-1)

Sergienko OV (2013) Basal channels on ice shelves. *Journal of Geophysical Research: Earth Surface*, **118**(3), 1342–1355 (doi: 10.1002/jgrf.20105)

Seroussi H, Nakayama Y, Larour E, Menemenlis D, Morlighem M, Rignot E and Khazendar A (2017) Continued retreat of thwaites glacier, west antarctica, con-

trolled by bed topography and ocean circulation. *Geophysical Research Letters*, **44**(12), 6191–6199 (doi: 10.1002/2017gl072910)

Shean DE, Joughin IR, Dutrieux P, Smith BE and Berthier E (2019) Ice shelf basal melt rates from a high-resolution digital elevation model (DEM) record for pine island glacier, antarctica. *The Cryosphere*, **13**(10), 2633–2656 (doi: 10.5194/tc-13-2633-2019)

Shepherd A, Wingham D and Rignot E (2004) Warm ocean is eroding west antarctic ice sheet. *Geophysical Research Letters*, **31**(23) (doi: 10.1029/2004gl021106)

Shepherd A, Fricker HA and Farrell SL (2018) Trends and connections across the antarctic cryosphere. *Nature*, **558**(7709), 223–232 (doi: 10.1038/s41586-018-0171-6)

Shuchman RA, Leshkevich G, Sayers MJ, Johengen TH, Brooks CN and Pozdnyakov D (2013) An algorithm to retrieve chlorophyll, dissolved organic carbon, and suspended minerals from great lakes satellite data. *Journal of Great Lakes Research*, **39**, 14–33 (doi: 10.1016/j.jglr.2013.06.017)

Sifuzzaman M (2009) Application of wavelet transform and its advantages compared to fourier transform. In *Application of Wavelet Transform and its Advantages Compared to Fourier Transform*

Smith B, Dickinson S, Jelley BJ, Neumann TA, Hancock D and Harbeck K (2022) Atlas/icesat-2 l3b slope-corrected land ice height time series, version 5 (doi: 10.5067/ATLAS/ATL11.005)

Stanton TP, Shaw WJ, Truffer M, Corr HFJ, Peters LE, Riverman KL, Bindschadler R, Holland DM and Anandakrishnan S (2013) Channelized ice melting in the ocean

boundary layer beneath pine island glacier, antarctica. *Science*, **341**(6151), 1236–1239 (doi: 10.1126/science.1239373)

Still H, Campbell A and Hulbe C (2018) Mechanical analysis of pinning points in the ross ice shelf, antarctica. *Annals of Glaciology*, **60**(78), 32–41 (doi: 10.1017/aog.2018.31)

Stoica P and Moses RL (2005) *Spectral Analysis of Signals*. Pearson, Upper Saddle River, NJ

Stokes CR, Abram NJ, Bentley MJ, Edwards TL, England MH, Foppert A, Jamieson SSR, Jones RS, King MA, Lenaerts JTM, Medley B, Miles BWJ, Paxman GJG, Ritz C, van de Flierdt T and Whitehouse PL (2022) Response of the east antarctic ice sheet to past and future climate change. *Nature*, **608**(7922), 275–286 (doi: 10.1038/s41586-022-04946-0)

Stramski D, Reynolds RA, Babin M, Kaczmarek S, Lewis MR, Röttgers R, Sciandra A, Stramska M, Twardowski MS, Franz BA and Claustre H (2008) Relationships between the surface concentration of particulate organic carbon and optical properties in the eastern south pacific and eastern atlantic oceans. *Biogeosciences*, **5**(1), 171–201 (doi: 10.5194/bg-5-171-2008)

Sullivan JM, Twardowski MS, Ronald J, Zaneveld V and Moore CC (2013) Measuring optical backscattering in water. In *Light scattering reviews 7*, 189–224, Springer

Taylor J, Siegert MJ, Payne AJ and Hubbard B (2004) Regional-scale bed roughness beneath ice masses: measurement and analysis. *Computers & Geosciences*, **30**(8), 899–908 (doi: 10.1016/j.cageo.2004.06.007)

Thursby G, Rego S and Keith D (2015) Data report for calibration of a bio-optical model for narragansett bay

Tiwari SP and Shanmugam P (2013) An optical model for deriving the spectral particulate backscattering coefficients in oceanic waters. *Ocean Science*, **9**(6), 987–1001 (doi: 10.5194/os-9-987-2013)

Trusel LD, Frey KE, Das SB, Munneke PK and van den Broeke MR (2013) Satellite-based estimates of antarctic surface meltwater fluxes. *Geophysical Research Letters*, **40**(23), 6148–6153 (doi: 10.1002/2013gl058138)

Vanderploeg HA, Johengen TH, Lavrentyev PJ, Chen C, Lang GA, Agy MA, Bundy MH, Cavaletto JF, Eadie BJ, Liebig JR, Miller GS, Ruberg SA and McCormick MJ (2007) Anatomy of the recurrent coastal sediment plume in lake michigan and its impacts on light climate, nutrients, and plankton. *Journal of Geophysical Research*, **112**(C3) (doi: 10.1029/2004jc002379)

Vaughan DG (1993) Relating the occurrence of crevasses to surface strain rates. *Journal of Glaciology*, **39**(132), 255–266 (doi: 10.3189/s0022143000015926)

Vaughan DG, Corr HFJ, Bindschadler RA, Dutrieux P, Gudmundsson GH, Jenkins A, Newman T, Vornberger P and Wingham DJ (2012) Subglacial melt channels and fracture in the floating part of pine island glacier, antarctica. *Journal of Geophysical Research: Earth Surface*, **117**(F3), n/a–n/a (doi: 10.1029/2012jf002360)

Voss KJ and Fry ES (1984) Measurement of the mueller matrix for ocean water. *Applied Optics*, **23**(23), 4427 (doi: 10.1364/ao.23.004427)

Wåhlin AK, Graham AGC, Hogan KA, Queste BY, Boehme L, Larter RD, Pettit EC, Wellner J and Heywood KJ (2021) Pathways and modification of warm water

flowing beneath thwaites ice shelf, west antarctica. *Science Advances*, **7**(15) (doi: 10.1126/sciadv.abd7254)

Walker CC, Becker MK and Fricker HA (2021) A high resolution, three-dimensional view of the d-28 calving event from amery ice shelf with ICESat-2 and satellite imagery. *Geophysical Research Letters*, **48**(3) (doi: 10.1029/2020gl091200)

Watkins RH, Bassis JN and Thouless MD (2021) Roughness of ice shelves is correlated with basal melt rates. *Geophysical Research Letters*, **48**(21) (doi: 10.1029/2021gl094743)

Watkins RH, Sayers MJ, Shuchman RA and Bosse KR (2023a) Assessment of using spaceborne LiDAR to monitor the particulate backscatter coefficient on large, freshwater lakes: A test using CALIPSO on lake michigan. *Frontiers in Remote Sensing*, **4** (doi: 10.3389/frsen.2023.1104681)

Watkins RH, Sayers MJ, Shuchman RA and Bosse KR (2023b) Validation of icesat-2 derived data products on freshwater lakes: Bathymetry, diffuse attenuation coefficient for downwelling irradiance, and particulate backscatter coefficient. *IEEE Geoscience and Remote Sensing Letters*, 1–1 (doi: 10.1109/lgrs.2023.3261551)

Wearing MG, Hindmarsh RC and Worster MG (2015) Assessment of ice flow dynamics in the zone close to the calving front of antarctic ice shelves. *Journal of Glaciology*, **61**(230), 1194–1206 (doi: 10.3189/2015jog15j116)

Webber BGM, Heywood KJ, Stevens DP, Dutrieux P, Abrahamsen EP, Jenkins A, Jacobs SS, Ha HK, Lee SH and Kim TW (2017) Mechanisms driving variability in the ocean forcing of pine island glacier. *Nature Communications*, **8**(1) (doi: 10.1038/ncomms14507)

Werner M, Jouzel J, Masson-Delmotte V and Lohmann G (2018) Reconciling glacial antarctic water stable isotopes with ice sheet topography and the isotopic paleothermometer. *Nature Communications*, **9**(1) (doi: 10.1038/s41467-018-05430-y)

Westberry T, Behrenfeld MJ, Siegel DA and Boss E (2008) Carbon-based primary productivity modeling with vertically resolved photoacclimation. *Global Biogeochemical Cycles*, **22**(2), n/a–n/a (doi: 10.1029/2007gb003078)

Whitehouse DJ (2004) *Surfaces and their measurement*. Kogan Page Science

Wild CT, Alley KE, Muto A, Truffer M, Scambos TA and Pettit EC (2022) Weakening of the pinning point buttressing thwaites glacier, west antarctica. *The Cryosphere*, **16**(2), 397–417 (doi: 10.5194/tc-16-397-2022)

Wille JD, Favier V, Jourdain NC, Kittel C, Turton JV, Agosta C, Gorodetskaya IV, Picard G, Codron F, Santos CLD, Amory C, Fettweis X, Blanchet J, Jomelli V and Berchet A (2022) Intense atmospheric rivers can weaken ice shelf stability at the antarctic peninsula. *Communications Earth and amp Environment*, **3**(1) (doi: 10.1038/s43247-022-00422-9)

Winker DM, Vaughan MA, Omar A, Hu Y, Powell KA, Liu Z, Hunt WH and Young SA (2009) Overview of the CALIPSO mission and CALIOP data processing algorithms. *Journal of Atmospheric and Oceanic Technology*, **26**(11), 2310–2323 (doi: 10.1175/2009jtecha1281.1)

Winker DM, Pelon J, Coakley JA, Ackerman SA, Charlson RJ, Colarco PR, Flamant P, Fu Q, Hoff RM, Kittaka C, Kubar TL, Treut HL, Mccormick MP, Mégie G, Poole L, Powell K, Trepte C, Vaughan MA and Wielicki BA (2010) The CALIPSO mission. *Bulletin of the American Meteorological Society*, **91**(9), 1211–1230 (doi: 10.1175/2010bams3009.1)

Wuite J, Jezek KC, Wu X, Farness K and Carande R (2009) The velocity field and flow regime of david glacier and drygalski ice tongue, antarctica. *Polar Geography*, **32**(3-4), 111–127 (doi: 10.1080/10889370902815499)

Yousef F, Shuchman R, Sayers M, Fahnenstiel G and Henareh A (2017) Water clarity of the upper great lakes: Tracking changes between 1998–2012. *Journal of Great Lakes Research*, **43**, 239–247 (doi: 10.1016/j.jglr.2016.12.002)

Zaneveld JRV, Pegau S and Mueller JL (2003) Volume scattering function and backscattering coefficients: instruments, characterization, field measurements, and data analysis protocols. *Ocean optics protocols for satellite ocean color sensor validation, revision*, **4**, 65–76

Zhong Y, Notaro M and Vavrus SJ (2018) Spatially variable warming of the laurentian great lakes: an interaction of bathymetry and climate. *Climate Dynamics*, **52**(9-10), 5833–5848 (doi: 10.1007/s00382-018-4481-z)

Zwally HJ and Schutz B (2014) Glas/icesat l1b global elevation data (hdf5) (doi: 10.5067/ICESAT/GLAS/DATA109)